

The Paton Welding Journal

01
2022

International Scientific-Technical and Production Journal
Founded in January 2000 (12 Issues Per Year)

EDITORIAL BOARD

Editor-in-Chief

I.V. Krivtsun E.O. Paton Electric Welding Institute, Kyiv, Ukraine

Deputy Editor-in-Chief

S.V. Akhonin E.O. Paton Electric Welding Institute, Kyiv, Ukraine

Deputy Editor-in-Chief

L.M. Lobanov E.O. Paton Electric Welding Institute, Kyiv, Ukraine

Editorial Board Members

O.M. Berdnikova E.O. Paton Electric Welding Institute, Kyiv, Ukraine

Chang Yunlong School of Materials Science and Engineering,
Shenyang University of Technology, Shenyang, China

V.V. Dmitrik NTUU «Kharkiv Polytechnic Institute», Kharkiv, Ukraine

Dong Chunlin China-Ukraine Institute of Welding of Guangdong Academy of Sciences, Guangzhou, China

A. Gumenyuk Bundesanstalt für Materialforschung und –prüfung (BAM), Berlin, Germany

V.V. Knysh E.O. Paton Electric Welding Institute, Kyiv, Ukraine

V.M. Korzhyk E.O. Paton Electric Welding Institute, Kyiv, Ukraine

V.V. Kvasnytskyi NTUU «Igor Sikorsky Kyiv Polytechnic Institute», Kyiv, Ukraine

Yu.M. Lankin E.O. Paton Electric Welding Institute, Kyiv, Ukraine

S.Yu. Maksymov E.O. Paton Electric Welding Institute, Kyiv, Ukraine

Yupiter HP Manurung Smart Manufacturing Research Institute, Universiti Teknologi MARA, Shah Alam, Malaysia

M.O. Pashchin E.O. Paton Electric Welding Institute, Kyiv, Ukraine

Ya. Pilarczyk Welding Institute, Gliwice, Poland

V.D. Poznyakov E.O. Paton Electric Welding Institute, Kyiv, Ukraine

U. Reisgen Welding and Joining Institute, Aachen, Germany

I.O. Ryabtsev E.O. Paton Electric Welding Institute, Kyiv, Ukraine

V.M. Uchanin Karpenko Physico-Mechanical Institute, Lviv, Ukraine

Yang Yongqiang South China University of Technology, Guangzhou, China

Managing Editor

O.T. Zelnichenko International Association «Welding», Kyiv, Ukraine

Address of Editorial Board

E.O. Paton Electric Welding Institute, 11 Kazymyr Malevych Str. (former Bozhenko), 03150, Kyiv, Ukraine

Tel./Fax: (38044) 200 82 77, E-mail: journal@paton.kiev.ua

<https://patonpublishinghouse.com/eng/journals/tpwj>

State Registration Certificate 24933-14873 ПП from 13.08.2021

ISSN 0957-798X, DOI: <http://dx.doi.org/10.37434/tpwj>

Subscriptions, 12 issues per year:

\$384 — annual subscription for the printed (hard copy) version, air postage and packaging included;

\$312 — annual subscription for the electronic version

(sending issues in pdf format or providing access to IP addresses).

The content of the journal includes articles received from authors from around the world in the field of welding, metallurgy, material science and selectively includes translations into English of articles from the following journals, published by PWI in Ukrainian:

- Automatic Welding (<https://patonpublishinghouse.com/eng/journals/as>);
- Technical Diagnostics & Nondestructive Testing (<https://patonpublishinghouse.com/eng/journals/tdnk>);
- Electrometallurgy Today (<https://patonpublishinghouse.com/eng/journals/sem>).

CONTENTS

ORIGINAL ARTICLES

L.J. Feinberg, V.V. Shchegol, L.V. Honcharenko TWO-WIRE SUBMERGED-ARC WELDING WITH COLD WIRE APPLICATION*	3
S. Gook, B. El-Sari, M. Biegler, M. Rethmeier, F. Lichtenthäler, M. Stark MULTIPLE-WIRE SUBMERGED ARC WELDING OF HIGH-STRENGTH FINE-GRAINED STEELS*	9
M. Polieschuk, I. Matveiev, V. Bovkun, J. Selech, A. Tunik, O. Cherkashin, L. Kisterska, K. Siekierski MAGNETIC-PULSE WELDING OF COPPER RINGS WITH STEEL PARTS USING SINGLE-TURN INDUCTOR*	14
A. StraÙe, A. Gumenyuk, M. Rethmeier IMPROVEMENT OF THE MECHANICAL PROPERTIES AND CORROSION RESISTANCE OF LASER WELDS ON THICK DUPLEX PLATES BY LASER CLADDED BUTTERING*	18
V.V. Skryabinskyi, V.M. Nesterenkov, A.V. Mykytchyk ELECTRON BEAM WELDING OF ALUMINIUM 1570 ALLOY AND MECHANICAL PROPERTIES OF ITS JOINTS AT CRYOGENIC TEMPERATURES*	22
N.V. Piskun, E.L. Vrzhyzhevskiy, V.A. Kostin, T.G. Taranova, I.L. Bogaichuk, I.I. Statkevych INFLUENCE OF TIME OF EXISTENCE OF MOLTEN POOL IN ELECTRON BEAM PROCESSES ON THE LEVEL OF EVAPORATION OF ELEMENTS WITH A HIGH VAPOR TENSION*	26
A.A. Makarenko, O.V. Makhnenko MATHEMATICAL MODELING OF RESIDUAL STRESSES IN COMPOSITE WELDED JOINTS OF WVER-1000 REACTOR VESSEL COVER WITH CSS NOZZLES*	33
N.O. Lysenko, O.O. Pedash, V.V. Klochykhin, P.O. Kasai INFLUENCE OF LONG-TERM SOAKING ON THE STRUCTURE AND PROPERTIES OF IN625 ALLOY SAMPLES MADE BY SELECTIVE LASER MELTING**	41
I.M. Javorskyi, R.M. Yuzefovych, O.V. Lychak, P.O. Semenov METHODS AND MEANS OF EARLY VIBRATION DIAGNOSTICS OF ROTATING COMPONENTS OF MECHANISMS OF QUAY CONTAINER HANDLERS***	48

INFORMATION

«The Paton Welding Journal» — Short History	59
---	----

*Translated Article(s) from «Automatic Welding», No. 1, 2022.

**Translated Article(s) from «Electrometallurgy Today», No. 4, 2021.

***Translated Article(s) from «Technical Diagnostics & Nondestructive Testing», No. 4, 2021.

<https://doi.org/10.37434/tpwj2022.01.01>

TWO-WIRE SUBMERGED-ARC WELDING WITH COLD WIRE APPLICATION

L.J. Feinberg, V.V. Shchegol, L.V. Honcharenko

E.O. Paton Electric Welding Institute of the NASU
11 Kazymyr Malevych Str., 03150, Kyiv, Ukraine

ABSTRACT

The possibility for improvement of welded joint properties by feeding cold wire into the weld pool to increase its cooling rate was considered. The technique of the process was investigated in the case of two-wire submerged-arc welding of low-alloyed 10G2FB steel at application of cold wire. Impact toughness of the metal of the weld and HAZ was determined on IX type specimens with a sharp notch to GOST 6996, depending on welding process parameters, and welded joint structures were studied.

KEY WORDS: low-alloyed steel, thermal cycle, impact toughness, cold wire, submerged-arc welding

INTRODUCTION

The problem of ensuring the reliability of the main gas pipelines by improving the properties of the welded joints remains to be urgent. One of the possible directions of its solution is a method proposed by ESAB Company, Sweden, for submerged-arc processes [1–3] with feeding cold wire (CW) into the weld pool. The idea of the method consists in increasing the welded joint cooling rate with the respective improvement of its structure and mechanical properties.

The objective of the research was evaluation of the effectiveness of the above-mentioned process in the case of two-wire submerged-arc welding in the modes characteristic for pipes of medium thickness (12–25 mm). In addition to mechanical properties of welded joints this process was to provide the specified penetration and sound formation of welds of 22–25 mm width with 0.5–3.0 mm reinforcement height and its smooth transition to base metal (BM).

When choosing the experimental parameters, the reference point was work [1], where the external weld of a two-sided butt joint 13 mm thick from X70 steel was welded by two arcs in the presence or absence of CW. Welding wire of 4 mm diameter of BA S2 Mo grade and BF 6.4 flux with 1.7 basicity were used.

BM chemical composition (wt.%) is given: 0.046 C; 1.76 Mn; 0.24 Si; 0.21 (V, Mo, Nb, Ti); 0.54 (Cu, Ni, Cr), as well as the composition of cold and electrode wires (wt.%): 0.10 C; 1.04 Mn; 0.1 Si; 0.56 Mo; 0.02 Ni; 0.03 Cr; 0.03 Cu.

The relatively high carbon content in the welding wire was supposed to lower austenite transformation temperature, so as to increase the acicular ferrite fraction and improve the weld structure, respectively.

Welding process parameters according to [1] were as follows:

- arc 1 — 1040/30, reverse polarity direct current;
- arc 2 — 830/34, square wave alternating current;
- welding speed — 160 cm/min (96 m/h);
- CW feed rate — 25.4 cm/min (15.2 m/h).

By our data, for such a mode welding wire feed rate in arcs 1 and 2 is equal to 135–140 m/h, so that CW fraction relative to each of these wires should be equal to ~0.11. In our experiments this fraction was increased as far as it was allowed by weld formation quality to achieve maximum effectiveness of the process.

CW is placed ahead of the first arc, between the arcs or behind the last arc [2]. In work [1] CW was placed behind the last arc that seems to be optimal, as in this case the penetration depth is not decreased, and weld pool is cooled to the maximum.

In the above-mentioned work HAZ was tested for impact bending, using specimens of 5×10×55 mm size with a sharp notch, one half of which passed through the zone of coarse grain, and the second one - through the zone of fine grain. At temperatures of 20 °C and –30 °C CW application increased the impact energy of HAZ metal by 10 J, and at –45 °C — by 20 J. More essential results as to HAZ properties were obtained at testing by SENT procedure.

Owing to reduction of heat input by 9 % and increase of the cooling rate by 10 % the HAZ structure was improved by a number of characteristics:

- reduction of primary austenite grain sizes from 68 to 55 μm, as a result of shortening of the time of staying in the austenite temperature range of 1400–1100 °C;
- reduction of the fraction of coarse MAK-phase particles of more than 2 μm size from 3.2±0.2 to 1.0±0.1 %;
- reduction of the sizes of ferrite-bainite grain in the HAZ from 17.6±5.0 to 15.3±4.5 μm (for X70 steel the mentioned grain size was 4.1±0.5 μm);
- increase of the angles of grain disorientation.

Table 1. Process parameters and weld dimensions

Weld number	Arc number	V_{CWf} mm/10 s	I_w/U_a A/V	V_{elf} mm/10 s	ψ	L_{cr} mm	Weld dimensions, mm		
							h	b	a
600	1	105	1100/36	485	0.21	185	14.6–14.8	22.7–23.1	3.0–3.5
	2		1010/38	498					
601	1	70	1100/36	485	0.14	195	~15.0	23.9–24.9	2.6–2.8
	2		980/38	498					
602	1	0	1100/36	485	0	230	~15.0	24.0–25.0	2.4–2.6
	2		960/38	498					

Note. Welding speed of 65 m/h (I_w — welding current; U_a — arc voltage; V_{CWf} — cold wire feed rate; V_{elf} — electrode wire feed rate; I_w ; U_a ; V_{CWf} ; V_{elf} ; ψ — ratio of cold and electrode (on arc 2) wires; L_{cr} — crater length; h , b — penetration and weld width; a — its reinforcement height).

MATERIALS AND PROCEDURES

In our laboratory tests, plates of low-alloyed cold-resistant steel 10G2FB of 19 mm thickness were used as BM. Electrode and cold wire of Sv-08G1NMA grade of 4.0 mm diameter, as well as OP 132 flux, made in France, were applied. Power to the first and second electrodes was supplied from VSZh-1600 rectifier and laboratory transformer with a square waveform of current, respectively. The inclination of the first and second electrodes to the vertical was equal to -7° and 20° , and the distance between them was 20 mm. Welding was performed on V-shaped grooves of $5 \text{ mm} \times 90^\circ$ size.

During work performance the influence of CW feed rate and its position on arcing stability and weld formation quality was determined with correction of the process parameters.

To evaluate the effectiveness of the new process in improvement of welded joint properties, comparative testing was performed with and without CW application. With this purpose, the specimens of weld and HAZ metal of IX type to GOST 6996 of $10 \times 10 \times 75$ mm size were tested for impact bending at temperatures of -20 and -40 °C, and metallographic analysis of the joint structure was also performed.

In keeping with the international standard for manufacturing pipes for underwater gas pipelines [4] the mentioned specimens were selected from the weld upper part at 2 mm distance from BM surface.

In the HAZ test specimens the notch was made normal to BM surface through the middle of the fusion line (FL) so that one of its halves passed through the weld, and the other one — through the HAZ. With such a procedure a considerable part of the notch is in the coarse grain zone that impairs the impact toughness properties.

In the case of weld asymmetry, the notch was made from the side of a more round FL, avoiding artificial overestimation of the test results.

Analysis of welded joint microstructure was performed with application of optical microscope on microsections etched in 4 % solution of HNO_3 .

RESULTS

TEST SERIES 1

CW was placed behind the last arc with backward inclination at 37° angle to the vertical so that in the state of shorting on BM the tips of CW and the last electrode contacted each other.

Two CW feed rates were tested, which were equal to 0.14 and 0.21 relative to the feed rate of second arc electrode wire (ψ coefficient) (Table 1). At increase of ψ coefficient to 0.21 weld formation became worse — its width was reduced from 24–25 to 23–22.7 mm, and reinforcement height increased from 2.4–2.8 to 3.0–3.5 mm (Figure 1).

CW closeness to arc 2 generated the self-regulation effect with increase of its current by approximate-

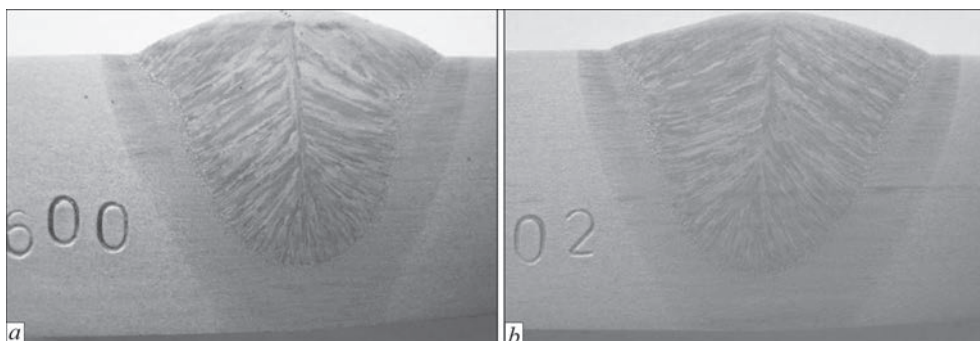


Figure 1. Macrosections of welds with CW application (No.600) and without it (No.602), $\times 2.7$

Table 2. Process parameters and weld dimensions

Weld number	Arc number	$V_{CW P}$ mm/10 s	I_w/U_a A/V	V_w m/h	$V_{el P}$ mm/10 s	ψ	Weld dimensions, mm		
							h	b	a
603	1	205	1100/36	65	485	0.46	14.6–14.8	21.7–21.9	3.2–3.5
	2		980/38–39		443				
605	1	160	1100/36	62	497	0.34	13.5–13.7	23.0–24.4	2.9–3.2
	2		900/42–43		467				
606	1	202	1100/36	62	497	0.43	14.3–14.5	23.1–24.1	2.7–3.1
	2		900/42–43		467				

Table 3. Influence of CW and its location on weld dimensions

Weld number	Arc number	ψ	$V_{CW P}$ mm/10 s	$I_w A/U_a, V$	$V_{el P}$ mm/10 s	Weld dimensions, mm		
						h	b	a
Reference weld without CW application								
702	1	0	0	1050/36	470	13.5	23.7–23.9	1.8–2.8
	2			900/42	445			
Reference welds with CW feeding behind the last arc								
700	1	0.37	165	1050/36	470	ND	23.5–24.6	3.2–4.1
	2			900/42	445			
701	1	0.48	215	1050/36	470	13.6	23.3–23.9	3.3–4.0
	2			900/42	445			
Reference weld with CW feeding between the arcs								
703	1	0.44	215	1050/36	470	13.0	24.8–25.7	3.6–4.1
	2			950/42	485			

ly 50 A. Increase of CW feed rate led to shortening of the crater length.

TEST SERIES 2 (MODE CORRECTION)

To improve weld formation the electrode feed rate in arc 2 was lowered, and the possibility of increasing CW feed rate was also tested at coefficient $\psi = 0.46$ to achieve greater cooling of the weld pool (weld No.603, Table 2). Alongside weld narrowing and anticipated increase of reinforcement height, the mentioned increase of wire feed rate also led to waviness of reinforcement edges.

Improvement of weld formation by mode No.603 was achieved by increasing the electrode spacing from 20 to 25 mm, reducing the welding speed from 65 to 62 m/h and increasing the second arc voltage (welds Nos 605, 606).

TEST SERIES 3 (INCREASE OF THE DISTANCE BETWEEN CW AND THE SECOND ELECTRODE)

Increase of the distance between CW and the second electrode was tested to stabilize the burning mode of the second arc and more effective cooling of the weld pool (Figure 2). Here, it should be limited, depending both on the welding mode and CW feed rate, to avoid lack-of-melting (“freezing”) of CW in the weld pool with emergency stopping of the process. A preliminary indication of emergence of such a situation is appearance of a slag crust on the surface of longitudinal protrusions and depressions, left by CW

when it sweeps up the half-molten slag crust and flux to the second arc with deterioration of its burning stability (Figure 3). In this case, the emergency situation appeared at the mentioned distance of more than 12 mm. Therefore, with the view to process stability it was reduced to 8 mm for further experiments (welds Nos 700, 701).

Experiments showed that CW “freezing” to the pool does not take place at increase of its feed rate at least to 215 mm/10 s (weld No.701), but it is accompanied by unacceptable increase of weld reinforcement

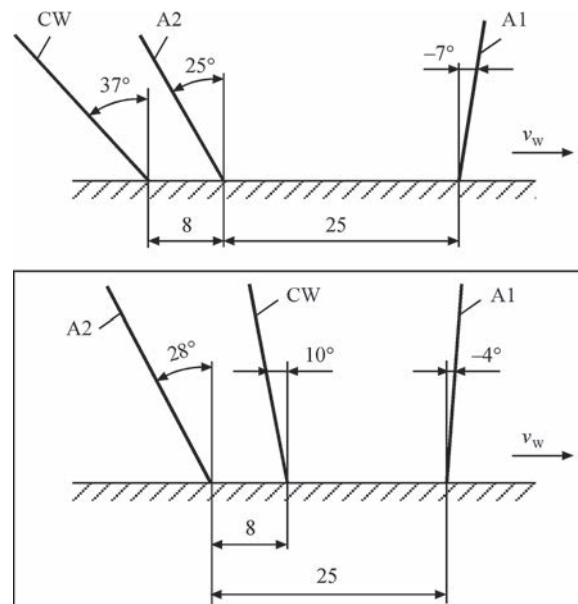


Figure 2. Variants of CW positioning



Figure 3. Unevenness of slag crust surface arising at excessive distance from CW to the last electrode

ment height (Table 3) that will require correction of the groove area.

TEST SERIES 4 (PLACING CW BETWEEN THE ELECTRODES)

Testing the variant with CW feeding between the arcs, in connection with the special features of machine design, required certain changes in the electrode setting parameters (Figure 2). Here, the quality of formation of the weld (No.703) improved as a result of positive forming effect from the action of the second arc

on excess metal from CW melting (see Table 3). It is known that such CW positioning is used to increase the process productivity [5].

Chemical composition of the metal of welds on 10G2FB steel was typical for gas pipes (Table 4), ensuring their high impact toughness (Table 5). Additional alloying by Ti–B can be used to further increase the weld metal impact toughness.

Impact toughness testing of weld metal did not reveal any advantages of the process with CW application (Table 5). As to HAZ metal, similar testing showed very high spreading of the results, which did not allow an objective evaluation of the possible advantages of CW application by this characteristic.

Analysis of the microstructure of welded joints Nos 701, 703, welded with CW application, was performed in comparison with a joint made in the same mode, but without CW application (specimen No.702). Photographs of the structures of coarse-grain zone are given in Figures 4, 5.

Structure of specimen No.702 is typical for joints from steel X70. In the coarse-grain zone it is of bainitic type with different form of the second phase precipitates (Figure 4). These are ferrite grains mostly

Table 4. Chemical composition of the metal of weld, wt.% and BM

Analysis point	C	Si	Mn	S	P	Ni	Mo	V	Al	Nb	Ti
Weld	0.086	0.33	1.60	0.009	0.018	0.19	0.19	0.058	0.025	0.02	0.010
BM	0.103	0.245	1.57	0.005	0.013	0.02	<0.01	0.081	0.030	0.03	0.013

Table 5. CW influence on welded joint impact toughness

Weld number	ψ , %	KCV, J/cm ²			
		Weld		HAZ	
		–20 °C	–40 °C	–20 °C	–40 °C
Series 1					
602	0.00	<u>166.2-185.2</u> 173.6	<u>87.5-145.6</u> 122.9	<u>83.1-144.3</u> 110.1	<u>55.8-94.7</u> 84.7
600	0.21	<u>159.7-172.5</u> 166.2	<u>97.6-144.4</u> 123.4	<u>62.1-245.9</u> 126.7	<u>38.5-90.5</u> 60.5
Series 2					
603	0.46	<u>169.6-256.1</u> 199.6	<u>106.0-157.9</u> 129.0	<u>63.1-219.0</u> 133.0	<u>42.8-142.2</u> 78.4
605	0.34	N/D	N/D	<u>158.2-220.7</u> 190.1	<u>75.3-202.2</u> 135.6
606	0.43	N/D	N/D	<u>68.3-245.6</u> 158.1	<u>107.6-153.4</u> 127.5
Series 3, 4					
701	0.48	<u>151.4-215.8</u> 197.9	<u>80.9-184.6</u> 143.3	<u>62.9-173.1</u> 107.9	<u>43.4-117.1</u> 70.1
703	0.44	<u>167.5-197.1</u> 182.3	<u>99.4-179.4</u> 129.1	<u>100.7-218.1</u> 157.2	<u>58.6-190.0</u> 106.1
702	0.00	<u>174.4-226.3</u> 193.8	<u>87.7-166.7</u> 122.9	<u>67.4-226.4</u> 120.7	<u>37.5-186.1</u> 92.3

Note. Number of specimens tested for each variant is 5 pcs.

with dense distribution of the ordered and unordered phases. Individual coarse ferrite grains are observed near FL, some of which have an elongated shape and are located in parallel to the above-mentioned line with sparse distribution of platelike forms of the second phase. In the zone adjacent to FL, the coarse grain corresponds to number 3–4 acc. to GOST 5639.

There can be three rows of such coarse grains near the FL. The longest extent of the coarse-grain zone is approximately 0.5 mm. A grid of continuous polygonal hypoeutectoid ferrite is present on the boundaries of primary austenite grains.

The type of microstructure in the coarse-grain zone of a welded joint of specimen No. 701, where CW was fed behind the last arc, is similar to specimen No.702. However, a greater number of grains with the prevailing fraction of the structure with an ordered form of the second phase, represented by parallel platelike packets located across the entire grain, is observed in it, while in the zone adjacent to FL, a tendency to formation of mostly grains of No.4 size, and individual grains of No.3 size is observed. The polygonal ferrite grid on the boundaries of primary austenite grains is not continuous. The extent of the coarse-grain zone does not exceed 0.42 mm.

On specimen No.703 CW application led to some more pronounced positive changes in the coarse-grain zone (Figure 5). They concern the extent (width) of the coarse-grain zone, its maximum size and structure type. So, the coarse-grain zone is reduced from 0.5 to 0.4 mm, while the maximum grain size decreases from Nos 3–4 to Nos 4–5 acc. to GOST 5639. CW also promotes improvement of the coarse grain structure, namely reduction of the volume of rack bainite in the form of extended packets, spreading through the entire grain, and increase of the volume of bainite with disoriented and globular carbide formations. Here, the greater part of the coarse grains near the FL consists of individual disoriented blocks. Reduction of the volume of hypoeutectoid ferrite fringe on the boundaries of the coarse grains in the HAZ is also observed.

MAK-phase chains were present in the overheated zone on grain boundaries in all the studied specimens.

Thus, CW application promoted a certain improvement of welded joint structure, which was manifested to the greatest extent in individual regions of the HAZ of weld No.703.

DISCUSSION OF THE RESULTS

Comparison of the modes of making welds Nos 600 and 602 (see Table 1) allowed evaluation of the energy consumed in CW melting, and determination of

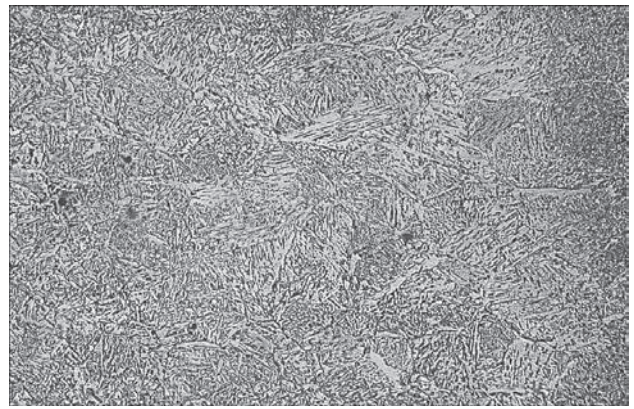


Figure 4. Microstructure ($\times 100$) of coarse-grain zone of a welded joint (No.702), made without CW application

$t_{8/5}$ parameter. If in the initial variant No.602 the rate of wire feed on arc 2 is increased by the value of CW feed rate in variant No.600, then, proceeding from the assumption of a proportional increase of welding current, it would rise by approximately 200 A. Thus, the energy required for CW melting at coefficient $\psi = 0.21$ is approximately equal to $U \cdot I \approx 36.200 \text{ V} \cdot \text{A}$. If self-regulation of arc 2 in process No.600 is eliminated by moving CW farther away from it, then this energy will be taken by the weld pool with its appropriate cooling and without the mentioned increase of its current. Under such conditions, reduction of heat input in the initial process No.602 at CW application, will be equal to approximately 10 %.

Parameter $t_{8/5}$ of the time of weld cooling in the temperature range of 800–500 °C is proportional to the process heat input [6]. Thus, CW application at $\psi = 0.21$ will reduce $t_{8/5}$ parameter also by 10 %, which is in agreement with the data of [1].

Acceleration of weld pool cooling rate using CW turned out to be insufficient for any significant improvement of the structure and noticeable increase of weld metal impact toughness. So, welds Nos 701, 703 welded using CW with rather high coefficient $\psi = 0.44\text{--}0.48$ in one series with weld No.702, where

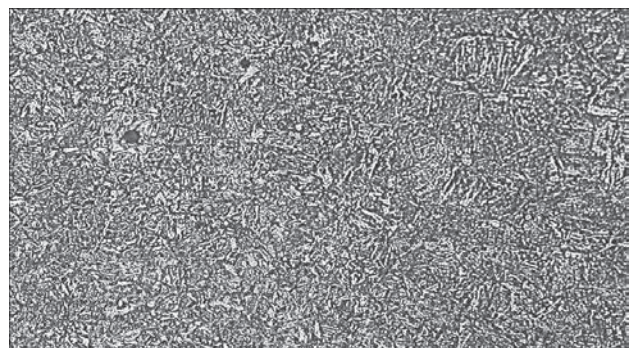


Figure 5. Microstructure ($\times 100$) of coarse-grain zone of a welded joint (No.703), made with CW application ($\psi = 0.44 \%$)

CW was not used, demonstrated approximately the same impact toughness (see Table 5).

As regards the HAZ metal, a great spreading of impact toughness values is observed. It is largely determined by the procedure of making the notch by the standard for underwater gas pipelines [5], in keeping with which a considerable part of it runs through the coarse-grain zone.

This zone is known to be characterized by great inhomogeneity of the structure and lowering of the metal ductile properties. Here, the smallest change of FL steepness influences the portion of the notch, running through the mentioned unfavourable zone, increasing the spreading of impact toughness values.

It should be also noted that at CW positioning behind the last arc an increase of FL steepness is observed, with probable lowering of the HAZ impact toughness values.

The new process showed a certain tendency to improvement of the HAZ metal structure.

CONCLUSIONS

The possibility of implementing the process with CW application is shown under the conditions of two-wire submerged-arc welding. CW feeding is performed behind the last arc or between the arcs. The ratio of CW mass to that of the second arc electrode wire (ψ coefficient) should not exceed 0.14–0.20. Increase of this ratio will require correction of the process initial parameters.

This process does not provide any essential improvement of mechanical characteristics of the joints, but somewhat improves the HAZ metal structure and can significantly increase the deposition rate.

REFERENCES

1. Mohammadijoo, M., Collins, L., Lazor, R. et al. (2018) Influence of cold-wire submerged arc welding on the toughness of microalloyed steel. *Welding J.*, 97(12), 338 s–352 s.
2. Raudsepp et al. (2018) *Method and system for submerged arc welding*. Pat. 10137521, USA, Publ. 27.11.2018.
3. Andersson, M., Johansson, T., Jungkvist, R., Raudsepp, H. (2015) *Method and system for submerged arc welding*. Pat. 020150202709A1, USA, Publ. 23.07.2015.
4. *DNV offshore standard for submarine pipeline systems, DNV-OS-F101*.
5. Raudsepp, H. (2021) *Tandem arc welding head and a welding arrangement for overlapping arcs to a cold wire electrode*. Pat. 10.994.362, USA, Publ. 04.05.2021.
6. Uver, D., u. Degenkolbe, J. (1977) Kennzeichnung von Schweißtemperaturzyklen hinsichtlich ihrer Auswirkung die mechanischen Eigenschaften von Schweißverbindungen. *Stahl u. Eisen.*, 97(24), 1201–1208.

ORCID

L.J. Feinberg: orcid.org/0000-0003-2029-7983

CONFLICT OF INTEREST

The Authors declare no conflict of interest

CORRESPONDING AUTHOR

L.J. Feinberg

E.O. Paton Electric Welding Institute of the NASU
11 Kazymyr Malevych Str., 03150, Kyiv, Ukraine
E-mail: leonid.fainberg@gmail.com

SUGGESTED CITATION

L.J. Feinberg, V.V. Shchegol, L.V. Honcharenko (2022) Two-wire submerged-arc welding with cold wire application. *The Paton Welding J.*, 1, 3–8.

JOURNAL HOME PAGE

<https://pwj.com.ua/en>

Received: 29.10.2021

Accepted: 07.02.2022

<https://doi.org/10.37434/tpwj2022.01.02>

MULTIPLE-WIRE SUBMERGED ARC WELDING OF HIGH-STRENGTH FINE-GRAINED STEELS

S. Gook¹, B. El-Sari¹, M. Biegler¹, M. Rethmeier¹, F. Lichtenthäler², M. Stark²

¹Fraunhofer Institute for Production Systems and Design Technology
Pascalstrasse 8–9, 10587, Berlin, Germany. E-mail: sergej.gook@ipk.fraunhofer.de

²SMS group GmbH, Hirtenwiese 4, 57578, Elkenroth, Germany

ABSTRACT

Ensuring the required mechanical-technological properties of welds is a critical issue in the application of multi-wire submerged arc welding processes for welding high-strength fine-grained steels. Excessive heat input is one of the main causes for microstructural zones with deteriorated mechanical properties of the welded joint, such as a reduced notched impact strength and a lower structural robustness. A process variant is proposed which reduces the weld volume as well as the heat input by adjusting the welding wire configuration as well as the energetic parameters of the arcs, while retaining the advantages of multi-wire submerged arc welding such as high process stability and production speed.

KEY WORDS: submerged arc welding, high-strength fine-grained steels, mechanical properties of the joints, energy parameters of the arc

INTRODUCTION

Submerged arc welding (SAW) with wire electrodes has a wide range of application in the manufacturing of numerous assemblies and components of various branches, such as large-diameter pipe manufacturing, the oil and gas industry, shipbuilding, the petrochemical industry, hydropower plants and offshore wind energy. Due to the high deposition rate of the process, a continuous production with a high cost-effectiveness can be achieved. For components with a thickness up to 10 mm, the single-wire SAW is sufficient. Parts with a larger thickness, require an increased deposition rate, which can be achieved through the application of multiple wire electrodes [1]. Especially, multi-wire SAW processes with up to five wire electrodes have proven successful [2].

However, the application of such highly efficient SAW process variants on modern high-strength steels (yield strength above 355 MPa) is challenging, because of the excessive heat input due to the large volume of the liquid weld pool [3] and the resulting softening in certain areas of the heat-affected zone (HAZ) [4]. These areas suffer from a decreased toughness as well as decreased strength properties of the welded joint [5, 6]. In particular, this problem concerns high-strength thermo-mechanically treated fine-grained steels, whose high mechanical-technological properties are achieved through the specifically adjusted thermo-mechanical rolling process. The fine-grained microstructure of these steels can be irreversibly destroyed in the HAZ, so that the width of the softening zone is essentially dependent on the welding process used and on the line energy [7, 8]. For comparison, a

single-wire SAW process has a typical deposition rate of about 8 kg/h, while a five-wire SAW process can achieve a deposition rate of 90 kg/h [2, 9]. The line energies for both process variants are about 2.5 kJ/mm and 10 kJ/mm, respectively. In DIN EN 10225:2009 [10] a nominal energy per unit length of 3.5 ± 0.2 kJ/mm for SAW of fine-grained structural steels for fixed offshore structures is recommended. However, the maximum allowable line energy may be 5 ± 0.2 kJ/mm if the material requirements are not met at 3.5 ± 0.2 kJ/mm. In the manufacturing of large-diameter pipes for the oil and gas industry, an increase in pipe wall thickness above 21 mm leads to an increase in heat input above 5 kJ/mm during welding, resulting in severe overheating and slow cooling of the metal in the HAZ. The specified heat input for a five-wire SAW process is thus far above the recommended values.

The presented welding process parameters as well as the requirements of the standard indicate a contradiction to the application of the multi-wire SAW process. This contradiction is due to the fact that, on the one hand, multi-wire submerged arc welding is highly interesting for the metalworking industry because of its cost-effectiveness. On the other hand, due to its process-specific properties, the use of this process leads to the fact that the mechanical-technological values of the welded joints are negatively influenced.

The objective of this work is to investigate process limits of a five-wire submerged arc welding process with respect to maximum welding speed, penetration depth and heat input by means of welding tests on thick-walled pipes. Furthermore, the possibilities to reduce the heat input by adjusting the process configuration should be shown.



Figure 1. Five-wire SAW test stand for welding sheets and tubes at Fraunhofer IPK in Berlin

WELDING EQUIPMENT AND MATERIALS

The welding experiments were conducted on a full-scale industrial welding system (SMS group GmbH) for longitudinal five-wire SAW on large-diameter pipes. The arcs are supplied with current by five electronically controlled current sources of type PERFECTarc® 1500 AC/DC (SMS group GmbH) with a total current of up to 7500 A. The resulting advantages are not limited to high deposition rates and welding speeds. With a programmable waveform for current and voltage, the welding result can be modeled with respect to various factors (e.g. weld geometry) [11]. Both, flat specimens with a length of two meters and large pipes with a length of up to six meters can be welded on the system. The transport carriage with the component to be welded can be moved at a speed of up to 6 m/min. The five-wire SAW system with two different geometries of specimens is shown in Figure 1.

In the conducted welding tests, pipe sections made of pipeline steel grade X70 according to API 5L or L485MB according to DIN EN 10208-2 (material No.1.8977) were used. The used welding consumables were solid wires BA S2Mo according to EN ISO 14171-A (EN 756) and an agglomerated welding powder of the aluminate-based type BF 5.1.

EXPERIMENTAL PROCEDURE AND RESULTS

Welding tests were performed on six meter long pipe sections with an outside diameter of 914.4 mm (36") and a wall thickness of 39 mm using the five-wire submerged arc welding method. The pipes used were the longitudinally welded pipe sections, which were provided with a tack weld as well as an inner layer. The welds investigated were therefore made as external welds in a 15 mm deep V-joint with an opening angle of 70°. A welding speed of ≥ 1 m/min, which was demanding for the given edge preparation, was set as a target. A calculation of the weld volume to be filled showed that a deposition rate of the process of at least 72 kg/hour should be achieved to ensure a closed profile of the weld. In addition, a weld penetration depth of at least 22 mm was targeted in order to melt the existing GMA tack weld and guarantee a secure bond between the outer layer and the previously applied inner layer.

A series of welds was performed with a wire configuration conventional for industrial practice, with the first two torches fitted with the 4.8 mm wires and the third, fourth and fifth wires having a diameter of 4 mm. In the second experiment, a 3.2 mm wire electrode was used on the first torch. The subsequent four wires had a diameter of 4 mm. The weld outer appearance, the metallographic



Figure 2. Outer appearance and cross-section of a SAW-weld. Outer layer welded with the following wire configuration: $d_{1,2} = 4.8$ mm and $d_{3,4,5} = 4$ mm; parameters: $V = 1.1$ m/min, $I_1 = 1480$ A, $U_1 = 34$ V; $I_2 = 1200$ A, $U_2 = 38$ V; $I_3 = 760$ A, $U_3 = 38$ V; $I_4 = 650$ A, $U_4 = 38$ V; $I_5 = 650$ A, $U_5 = 38$ V

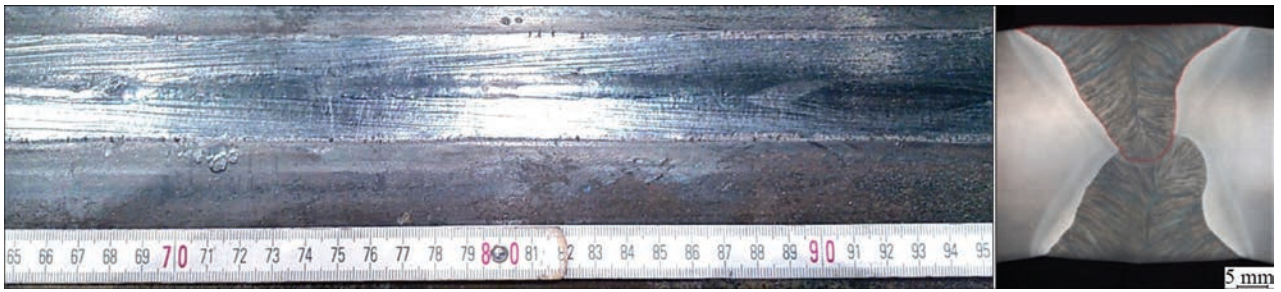


Figure 3. Outer appearance and cross-section of a SAW weld. Outer layer welded with the following wire configuration: $d_1 = 3.2$ mm and $d_{2,3,4,5} = 4$ mm; parameters: $V = 1.2$ m/min, $I_1 = 1200$ A, $U_1 = 32$ V; $I_2 = 1150$ A, $U_2 = 36$ V; $I_3 = 780$ A, $U_3 = 42$ V; $I_4 = 760$ A, $U_4 = 44$ V; $I_5 = 760$ A, $U_5 = 44$ V

cross sections and the welding parameters for both process variants are shown in Figures 2 and 3.

The control system of the welding current sources made it possible to record all relevant process data such as welding current, voltage and the welding and wire feed speed during welding at a sampling rate of 50 Hz and to use them for further analysis of the welding process. The recorded data of the welding process are shown as an example in Figure 4.

The smooth progressions of the welding current and voltage signals for all five wires indicate that the welding process is stable. The actual deposition rate of the welding processes could be determined from the recorded wire feed rates.

The evaluation of the results showed that the welding process in the configuration presented in Figure 2 could be run at a welding speed of 1.1 m/min. A line energy of 9.5 kJ/mm had to be brought out to achieve a deposition rate of 83 kg/hour. The V-joint was thus completely filled. The seams showed a slight concavity of the top bead of 0.7 mm. With a welding depth of 20.5 mm, a through-welded seam could be produced, so that the seam cross-section was completely closed. However, the welding depth achieved must be considered as borderline, as the inner layer could only just

be reached. The process variant with a 3.2 mm leader wire demonstrates a different result (see Figure 3). Here, a greater weld penetration depth of 24.5 mm was achieved than that for the process configuration with the 4.8 mm leading wire. Due to a larger weld penetration depth, the weld exhibited a slimmer profile, resulting in a reduction of the weld cross-section from 425.8 to 379.8 mm² (by 10.8 %). The welding speed could be increased up to 1.2 m/min, which produced a flat weld with no concavity. The line energy went down to 9.1 kJ/mm (by 4.2 %).

The temperature cycles during welding were measured with type K thermocouples. Since the weld width was about 40 mm, the thermocouples were placed at a distance of about 20 mm from the center of the V-joint. Hence, it was possible to record the $t_{8/5}$ time in the HAZ, in close proximity to the fusion line. The results of the temperature measurement for the two process variants can be seen in Figure 5. The line energy of the welding process of 9.5 kJ/mm resulted in a $t_{8/5}$ time of 92 seconds. For the process variant with a line energy of 9.1 kJ/mm, the $t_{8/5}$ time went down to 83 seconds. The corresponding cooling rates are 3.2 and 3.6 °C/s. However, if we consider the recommendations on the cooling rate for longitudinal submerged arc welding of

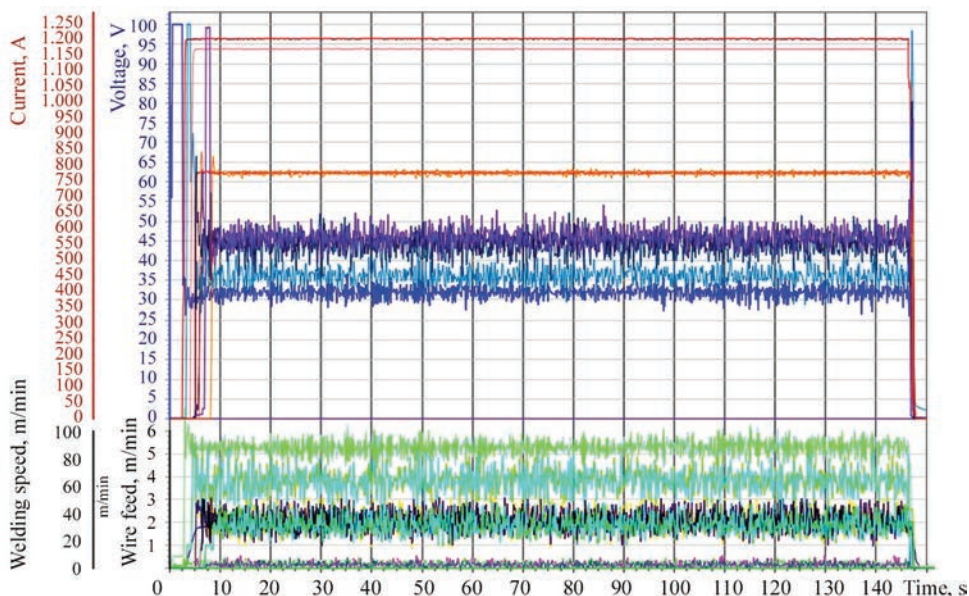


Figure 4. Recorded process data during five-wire SAW welding of a thick-walled pipe

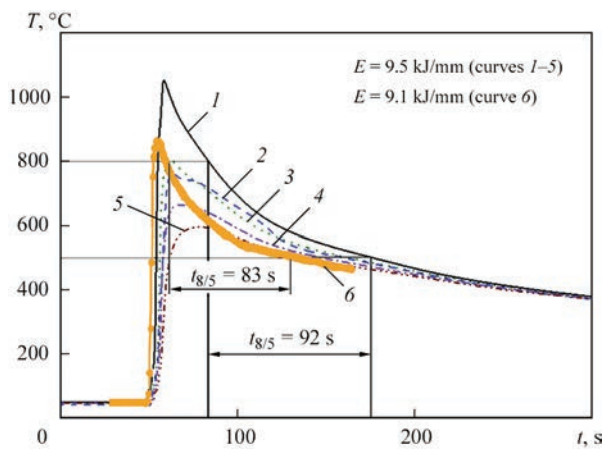


Figure 5. Welding temperature cycles for five-wire SAW welding for $E = 9.5$ kJ/mm und $E = 9.1$ kJ/mm, outer seam, tube wall thickness 39 mm

large-diameter pipes, we find that it should be in the range of 10 to 60 °C/s [12–15]. The values considered here are far from the recommended cooling rates. The negative effect of too high line energies on the ductile-plastic properties of HAZ was demonstrated by the hardness tests. Using the $HV1$ hardness test, it was found (Figure 6) that welds produced at 9.5 kJ/mm had a relatively high drop in HAZ hardness (0.79 of the base metal hardness). When welded with 9.1 kJ/mm of line energy, the welds have a lower hardness drop in HAZ (0.91 of the base metal hardness), but this can mean a strength loss of about 10 %.

For both process variants considered, it can be seen that the energy per unit length for five-wire SAW is too high and must be reduced further to avoid the formation of unfavorable microstructures and a reduction in the ductile-plastic properties in the HAZ.

DISCUSSION

In multi-wire SAW, it is common for the first wire to be supplied with DC positive to achieve the maximum weld penetration depth. The subsequent wires are supplied with AC current with a phase shift of 90° in order to minimize mutual magnetic blowout effects.

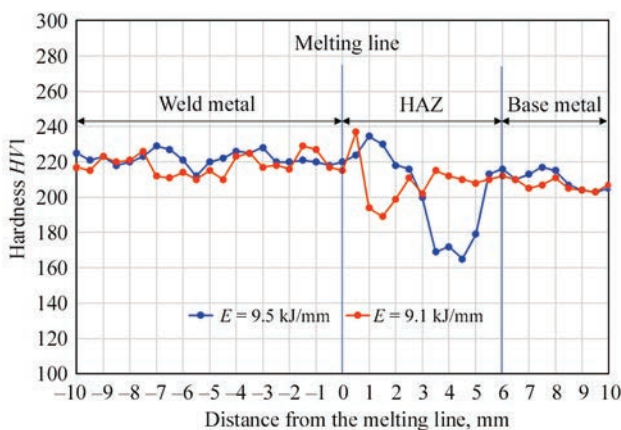


Figure 6. Hardness profile $HV1$ in the weld seam during five-wire SAW welding for $E = 9.5$ kJ/mm und $E = 9.1$ kJ/mm, outer seam, tube wall thickness 39 mm

In the process variants considered here, the current of the first 4.8 mm wire was 1480 A and was at the upper power limit of the current source. The current density at the tip of the wire reached 98 A/mm², which is a typical value for SAW with a solid wire electrode. In the second process variant, a 3.2 mm wire electrode was used on the first torch. With a significantly higher current density at the tip of the 3.2 mm wire of 125 A/mm², it was possible to achieve a weld penetration depth approx. 20 % greater than that for the process configuration with the 4.8 mm wire in front.

Based on this effect, a technological recommendation can be proposed for multi-wire SAW on heat-sensitive fine-grained steels. Basically, to achieve a lower heat input, the edge preparation must be modified accordingly. This means that the opening angle of the joint must be reduced so that the joint is reliably filled at the set welding parameters. The amount of filler metal required to fill the V-joint is thereby reduced and the heat input in multi-wire submerged-arc welding can be lowered. Hence, the line energy does not exceed the specified limit. By reducing the heat input in this way during SAW of thick-walled pipes, cooling rates of up to 10 °C/s and higher can be achieved [15]. For welding an outer layer on a pipe with a wall thickness of 39 mm, this means that the opening angle of the V-joint must be reduced from 70 to 60° and the depth of the V-groove must be reduced by one millimeter from 15 mm to 14 mm. The required deposition rate at a welding speed of 1.2 m/min would be about 67 kJ/h and the line energy 6.5 kJ/mm.

The comparison of the inner seam shape shows that the weld with the thicker leading wire has a semi-circular fusion line, a more favorable shape, than the seam with thinner 3.2 mm wire in front (see Figures 2 and 3). The seam width relates to the seam depth as 1:1 for the seam with 4.8 mm wire in front. For the thinner leading wire, this ratio is at an unfavorable value ≤ 1 because the seam is too deep. Here, however, it must be noted from macrographs provided that the weld with 3.2 mm wire in front does not have parallel flanks or melt lines, which would indicate unfavorable crystallization front. The weld is rather triangular or fillet-shaped in shape. It can be seen that crystallization occurs perpendicular to the fusion line and crystallines are oriented towards the top region of the weld, i.e. the region of the weld where the lowest mechanical stresses due to heat shrinkage occur. From this point of view, the “width to depth ratio” criterion must be considered critically, especially for the welds where no classical semicircular or almost straight fusion lines can be observed.

Another advantage of the process variant with the thinner leading wire, which should not be underestimated, is that the melted cross-sectional area of the weld seam is approx. 10 % smaller than in the variant with the 4.8 mm wire. This advantage is reflected

in the fact that with a smaller weld cross-section, the mixing of the filler metal with the base metal is also lower. It is known from practice that a high degree of mixing is unfavorable for higher-strength grades and must therefore be kept as low as possible.

CONCLUSIONS

Current multi-wire SAW techniques, when welding thick-walled pipes made of high-strength fine-grain steels, are characterized by high energy of the process up to 9.5 kJ/mm and thus do not provide a cooling rate in HAZ within the recommended range of 10–60 °C/s. This limits the applicability of multi-wire submerged arc welding in pipe production, especially when processing higher strength grades X70 and higher according to API 5L.

Based on the welding tests with a five-wire SAW process on a pipe with a wall thickness of 39 mm, it was shown that with decreasing diameter of the leading (DC) welding wire, the penetration depth of the arc and thus also the weld penetration depth increases by approx. 20 % compared to a conventional welding wire configuration. The weld becomes slimmer and has a fillet-shaped weld penetration profile.

Based on this effect, a process recommendation is proposed for minimizing the energy of the line and increasing the cooling rate in the area of the HAZ. Reducing the opening angle of the V-joint in combination with lowering of V-groove depth will result in a reduction of the weld cross-section. The required amount of filler material is reduced and line energy of the process decreases. With this process configuration, it is also possible to switch to a four-wire UP welding process because the use of the fifth wire is no longer necessary due to the reduced deposition rate.

REFERENCES

1. Brensing, K.H., Sommer, B. *Herstellverfahren für Stahlrohre*. Salzgitter Großrohre GmbH. www.wv-stahlrohre.de/fileadmin/pdf/Stahlrohre_Herstellverfahren.pdf
2. DVS Merkblatt 0915 (02/2000) Unterpulver-Mehrdrahtschweißen 3. Moeinifar, S., Kokabi, A.H., Hosseini, H.M. (2011) Role of tandem submerged arc welding thermal cycles on properties of the heat affected zone in X80 microalloyed pipe line steel. *J. Materials Proc. Technology*, 211(3), 368–375.
3. Hochhauser, D.I.F., Rauch, M.R. (2012) Influence of the soft zone on the strength of welded modern HSLA steels. *Welding in the World*, 56(5–6), 77–85.
4. Maurer, W., Ernst, W., Rauch, R. et al. (2013) Einfluss der Weichen Zone auf die mechanischen Eigenschaften hochfester Schweißverbindungen. *Schweiss- & Prüftechnik*, 10–15.
5. Bang, K.S., Kim, W.Y. (2002) Estimation and prediction of HAZ softening in thermomechanically controlled-rolled and accelerated-cooled steel. *Welding J. New York*, 81(8), 174–S.
6. Sirin, K., Sirin, S.Y., Kaluc, E. (2016) Influence of the inter-pass temperature on $t_{8/5}$ and the mechanical properties of sub-

- merged arc welded pipe. *J. of Materials Proc. Technology*, 238, 152–159.
7. Viano, D.M., Ahmed, N.U., Schumann, G.O. (2000) Influence of heat input and travel speed on microstructure and mechanical properties of double tandem submerged arc high strength low alloy steel weldments. *Sci. and Technol. of Welding and Joining*, 5(1), 26–34.
8. Aichele, G. (1994) *Leistungskennwerte für Schweißen und Schneiden*. Fachbuchreihe Schweißtechnik. DVS-Verlag GmbH Düsseldorf.
9. Norm DIN EN 10225:2009-10. *Schweißgeeignete Baustähle für feststehende Offshore-Konstruktionen – Technische Lieferbedingungen*. Deutsche Fassung EN 10225:2009
10. Wietrzniok, H., Lichtenthäler, F. (2014) Moderne Großrohrfertigung – Neue Hochleistungs-Schweißstromquelle für alle Lichtbogenschweißverfahren. *DVS Berichte*, 306, 19–25, DVS-Verlag, Düsseldorf 2014.
11. Hulka, K. (2005) The role of niobium in low carbon Bainitic HSLA Steel. In: *Proc. of 1st Intern. Conf. on Super-High Strength Steels (Rome, Italy, November 2005)*.
12. Knoop, F.M., Bremer S., Flaxa V. et al. (2011) The processing of helical-welded large diameter pipes of grade X80 with 23.7 mm wall thickness and their properties. In: *Proc. of Intern. Seminar on Welding of High Strength Pipeline Steels (Araxa, Brazil, November)*, 209–229.
13. Frantov, I., Permyakov, I., Bortsov, A. (2011) Improved weldability and criterion for reliability of high strength pipes steels. In: *Proc. of Intern. Seminar on Welding of High Strength Pipeline Steels (Araxa, Brazil, November)*, 247–260.
14. Chengia, Shang, Xiaoxiang, Wang, Quingyou, Liu, Jianyan, Fu. (2011) Weldability of higher niobium X80 pipeline steel. In: *Proc. of Intern. Seminar on Welding of High Strength Pipeline Steels (Araxa, Brazil, November)*, 435–453.
15. Khudyakov, A.O., Korobov Yu.S., Danilkin P.A., Kvashnin V.D. (2019) Finite element analysis of heat distribution for multiple-electrode submerged arc welding of high-strength pipe steels. In: *Proc. of 13th Intern. Conf. on Mechanical Behaviour of Materials (ICM-13) (Melbourne, Australia)*, 190–197.

ORCID

S. Gook: orcid.org/0000-0003-2029-7983

CONFLICT OF INTEREST

The Authors declare no conflict of interest

CORRESPONDING AUTHOR

S. Gook

Fraunhofer Institute for Production Systems and Design Technology, Pascalstrasse 8–9, 10587, Berlin, Germany.

E-mail: sergej.gook@ipk.fraunhofer.de

SUGGESTED CITATION

S. Gook, B. El-Sari, M. Biegler, M. Rethmeier, F. Lichtenthäler, M. Stark (2022) Multiple-wire submerged arc welding of high-strength fine-grained steels. *The Paton Welding J.*, 1, 9–13.

JOURNAL HOME PAGE

<https://pwj.com.ua/en>

Received: 23.12.2021

Accepted: 07.02.2022

<https://doi.org/10.37434/tpwj2022.01.03>

MAGNETIC-PULSE WELDING OF COPPER RINGS WITH STEEL PARTS USING SINGLE-TURN INDUCTOR

M. Polieschuk¹, I. Matveiev¹, V. Bovkun¹, J. Selech², A. Tunik¹, O. Cherkashin¹, L. Kisterska³, K. Siekierski⁴

¹E.O. Paton Electric Welding Institute of the NASU
11 Kazymyr Malevych Str., 03150, Kyiv, Ukraine

²Poznan University of Technology. 60-965, 5 M. Skłodowska-Curie Square, Poznan, Poland

³Ukrainian-American JV «Marketing of Superhard Materials»
2 Avtozavodska Str., 04074, Kyiv, Ukraine

⁴NxTechnologies. 60-125, ul. Bosa, 4/6-24, Poznań, Poland

ABSTRACT

Magnetic-pulse welding is an innovative joining method that allows combining dissimilar metals. The article discusses weldability of copper rings with steel rods in order to study the possibility of using single-turn inductor. All specimens were welded with a discharge energy of 18 kJ. Significant deformations of copper rings were observed. Metallographic examination of welds revealed no defects. High-quality joining of metals in the welding zone with a characteristic wavy boundary interface was noted. However, to obtain more information on the exact mechanisms of weld formation, it is recommended to carry out numerical modeling of the process.

KEY WORDS: magnetic-pulse welding, cold welding, solid state welding, copper, steel, rings, microstructure, microhardness

INTRODUCTION

Magnetic-pulse technologies are increasingly used in modern industry and, in particular, in welding. They are characterized by a more dynamic growth of scientific and technical publications as compared to many conventional methods of welding [1, 2].

Magnetic-pulse welding (MPW) is the solid phase welding, which is performed as a result of the collision of joined surfaces under the action of the pulsed magnetic field of the inductor and the current induced by this field in metal parts. When the inductor current interacts (Figure 1) with the induced current, in a part repulsive forces arise between the inductor and a part. As a result, a part in the area under the inductor, receiving a high speed of movement, moves to a fixed

part. The formation of a welded joint is provided by plastic deformations due to the collision of surfaces. The collision rate reaches hundreds of m/s, and the pressure in the contact zone reaches thousands of MPa [3, 4]. The general scheme of the MPW process of cylindrical parts is shown in Figure 1.

The following advantages of the technology are distinguished: welding of both similar and dissimilar metals; absence of thermal deformations; high speed of welding (pulse duration ~30 μ s); high quality of welding and repeatability of results; low energy consumption (approximately 10 times lower than in MIG welding); possibility of process automation; possibility to produce rectilinear welded joints up to 3 m length. The MPW process does not require the operation of cleaning parts, consumables (welding wire, gases) and local exhaust ventilation due to the absence of harmful emissions. It should also be noted that conventional methods of welding rings with cylindrical parts do not meet the needs of modern industry in terms of manufacturability, quality, efficiency, price and environmental impact. From this point of view, MPW technology is the technology of choice for many cases. This is especially true when parts operate in a tribological friction pair “copper ring – steel cylinder” and where high requirements are specified to the absence of solid inclusions in the material of rings and the requirements to process efficiency.

All this initiated a number of activities within the framework of UN and the European Union and led to the foundation of a large-scale international project JOIN’EM, which aims to study some aspects of magnetic-pulse welding [5–7].

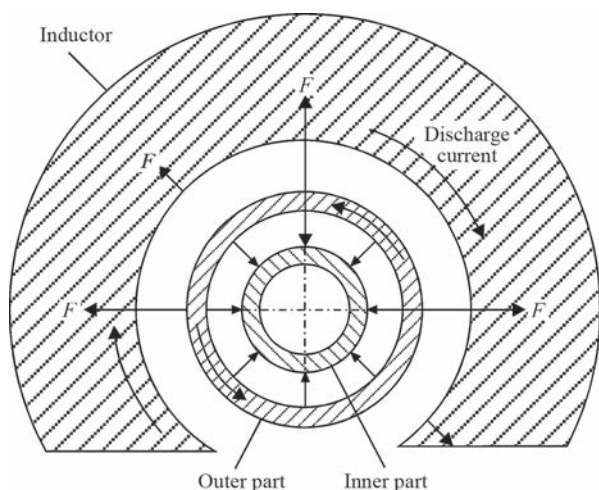


Figure 1. Process diagram for MPW of cylindrical parts

Copyright © The Author(s)

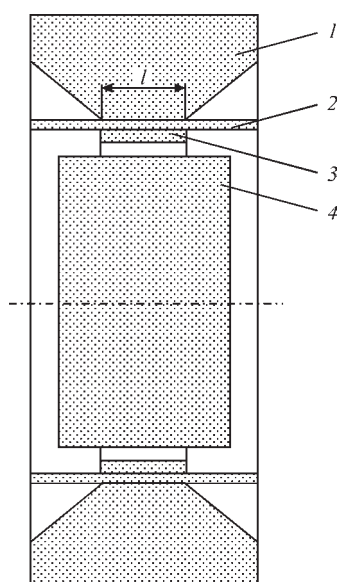


Figure 2. Scheme of single-turn inductor with workpieces before welding: 1 — inductor; 2 — insulator; 3 — copper ring; 4 — steel workpiece — target



Figure 3. Installation H-126A for magnetic-pulse welding

Most scientific and technical publications on this topic are devoted to MPW of cylindrical parts (tube-to-tube, tube-to-rod) [8, 9] using multi-turn inductors and magnetic field concentrators. Taking into account some differences in the processes of deformation of tubes and rings in MPW and increased energy losses when using such inductors with field concentrators, the authors proposed to use single-turn inductors (Figure 2) for welding parts such as “copper ring – steel rod/tube”, which allows producing a quality joint at a discharge energy of less than 35 [9] and 20 kJ [8].

It is also relevant to realize the MPW process on metals and alloys of domestic production, the compo-

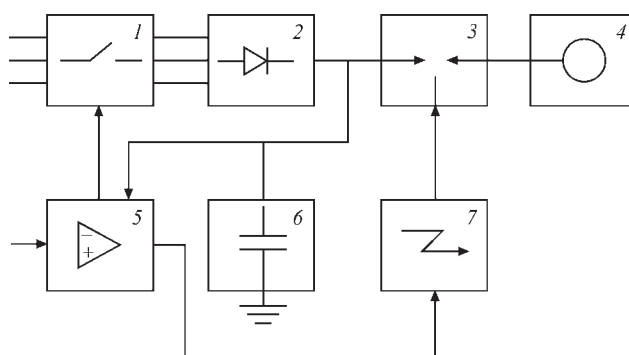


Figure 4. Structural block diagram of design of H126 installation: 1 — controlled network switch; 2 — high-voltage rectifier; 3 — controlled gas-discharge switch (trigatron); 4 — working inductor; 5 — automation unit with manual voltage adjuster; 6 — unit of high-voltage power capacitors; 7 — controlled arc ignition unit (oscillator)



Figure 5. Laboratory inductor

sition and properties of which often differ from those analogues produced abroad.

MATERIALS, EQUIPMENT AND RESEARCH METHODS

The study was performed using a modified installation H-126A (Figure 3). This installation was designed by the E.O. Paton Electric Welding Institute and was the first MPW installation certified at the EU, manufactured by a commercial batch.

When conducting metallographic examinations, a procedure was used that includes metallography — optical microscope Neophot-32, durometric analysis — hardness tester M-400 of LECO Company at a load of 0.098 and 0.249 N.

The structural scheme of the design of H-126A is shown in Figure 4.

Table 1. Chemical composition (wt.%) of the material 3sp steel, DSTU 4484:2005/GOST

C	Si	Mn	Ni	S	P	Cr	N	Cu	As
0.14–0.22	0.15–0.3	0.4–0.65	≤0.3	≤0.05	≤0.04	≤0.3	≤0.008	≤0.3	≤0.08

Table 2. Chemical composition (wt.%) of the material M1 copper. DSTU EN 1057: 2016

Fe	Ni	S	As	Pb	Zn	O	Sb	Bi	Sn	–
≤0.005	≤0.002	≤0.004	≤0.002	≤0.005	≤0.004	≤0.05	≤0.002	≤0.001	≤0.002	Cu+Ag min 99.9



Figure 6. Specimens joined by MPW

The process of measuring current was performed according to a new method proposed at the PWI, which is supposed to be an alternative to the conventional method, using the so-called Rogowski coil. The measurements used a high-speed USB oscilloscope DATAMAN 570 and the corresponding software for processing and post-processing of the obtained data.

For the study of joints of dissimilar metals produced by the MPW method, cylindrical specimens with an outer diameter D_{out} — 26.3 mm of 3sp steel (Table 1) and rings of copper of grade M1 (Table 2) with an outer diameter D_{out} — 30.6 mm, inner diameter D_{in} — 28.6 and width of 7 mm were prepared.

A laboratory single-turn inductor (Figure 5), insulators and specimen aligning fixtures were also manufactured.

RESULTS OF RESEARCH AND DISCUSSION

The process of welding-on rings of M1 copper to steel specimens of 3sp steel (Figure 6) was carried out at a charge voltage on the battery of 18 kV capacitors. The

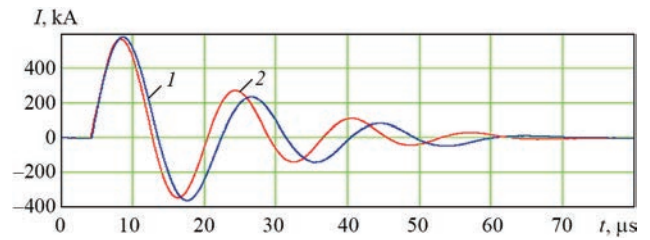


Figure 7. Oscillograms of currents in MPW at a charge energy of the capacitor battery of 18 kJ: 1 — inductor without a workpiece; 2 — inductor with a workpiece

total capacitance of the capacitors was 115 μ F. Current switching was performed using a controlled arc discharger of “trigatron” type. The width of the working turn of the inductor was 6 mm. From the experience of previous experiments it was found that for a given geometric configuration of parts, the optimal gap between them is 1.15 mm. Before the process of welding the specimens, the pulse current was registered on the inductor without a workpiece and with a workpiece (Figure 7).

The appearance of the specimens after welding indicates the presence of significant plastic deformation of copper rings (see Figure 6).

Metallographic examinations showed that when joining copper rings with a wall thickness of 1 mm and a width of 7 mm with cylindrical steel surfaces, the areas of linear joining of 2.3–5.0 mm size with a wavy-tooth line of the zone of this joint are observed. The relief and

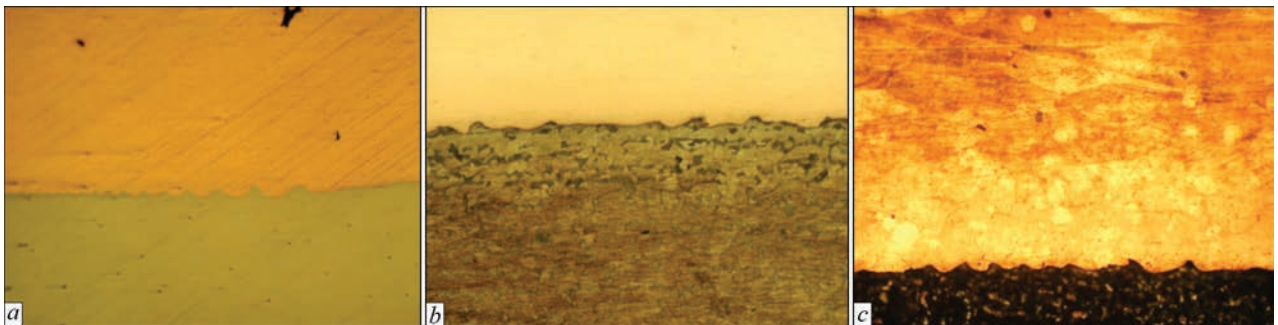


Figure 8. Macro- (a) and microstructure (b, c) of copper-steel joints produced by MPW method

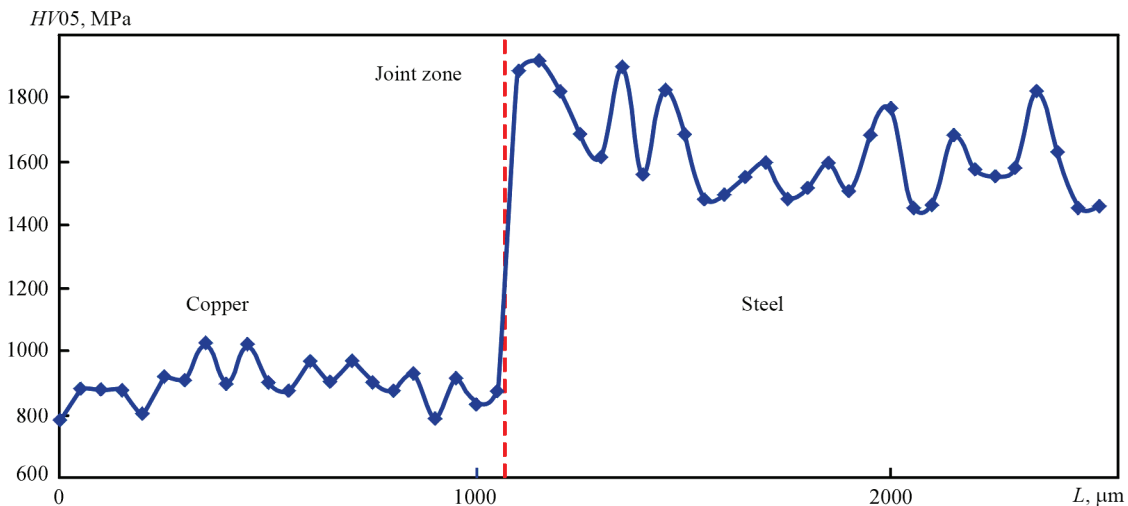


Figure 9. Diagram of change of microhardness of copper-steel specimen after MPW

geometrical characteristics of the joint line area depend on the welding process parameters (discharge energy, gap between parts, etc.) and design of the inductor [10, 11]. The height of teeth in the joint area was 10–30 μm (Figure 8, *a*). The thickness of the welded-on copper layer was 0.96–1.16 mm. This difference in thickness is caused by the influence of the nonuniform magnetic field of the working zone of the inductor. In the joint zone on the side of copper, changes in the metal structure were recorded — rounded grains with a diameter of 20–80 μm at a distance of 270–500 μm from the joint zone are observed. Rounded grains are located near the joint area. Moving further from this area, their number decreases and the structure turns into large deformed copper grains with twins (Figure 8, *c*).

The microhardness of copper in the joint area is 1344 MPa (Figure 9), which almost does not differ from the total hardness of the copper layer — 1361 MPa, the microhardness of rounded grains is 3–5 % higher (~1382 MPa) than that of large deformed grains (~1361 MPa).

In the joint area on the side of steel to a depth of ~ 50 μm , a ferrite band was recorded. Its average microhardness in the joint area is 2058 MPa, which is 16 % higher than the microhardness in the centre of a steel part, being 1777 MPa. Further changes in the banded ferrite-pearlite structure are not observed (Figure 8, *b*).

CONCLUSIONS

The weldability of copper rings to steel rods was investigated in order to study the possibility of using a single-turn inductor. A high-quality joint of copper rings of 1 mm wall thickness with steel cylinders was produced with the use of discharge energy of up to 18 kJ.

Metallographic analysis revealed a high-quality joint of copper rings with steel parts with a two-zone shape of joining, as well as structural changes in the weld zone, while the microhardness of steel within this zone increases in average by 16 %.

In the future, investigations will be conducted to study the effect of different process parameters (gap between parts, energy and discharge frequency) on the strength and metallographic characteristics of Cu–Fe welds.

To gain a better understanding of exact mechanisms of welding, effect of ring wall thickness on weld formation, and deformation of components, numerical simulation should also be performed.

REFERENCES

1. Polieschuk, M.A., Matveev, I.V., Bovkun, V.A. (2012) Fields of application of magnetic-pulse welding (Review). *The Paton Welding J.*, **4**, 42–46.
2. Polieschuk, M.A., Matveev, I.V., Bovkun, V.O. et al. (2020) Application of magnetic-pulse welding to join plates from similar and dissimilar alloys. *The Paton Welding J.* **8**, 41–45. DOI: <https://doi.org/10.37434/tpwj2020.08.07>
3. Lueg-Althoff, J., Schilling, B., Bellmann J. et al. (2016) Influence of the wall thicknesses on the joint quality during magnetic pulse welding in tube-to-tube configuration. In: *Proc. of 7th Intern. Conf. on High Speed Forming – 2016* <https://core.ac.uk/download/pdf/46917088.pdf>
4. Miranda, R.M., Tomás, B., Santos, T.G., Fernandes, N. (2014) Magnetic pulse welding on the cutting edge of industrial applications. *Soldag. Insp. São Paulo*, **19**(1), 69–81, Jan/Mar, <http://www.scielo.br/pdf/si/v19n1/a09v19n1.pdf>
5. (2017) Process analysis for magnetic pulse welding of copper tubes to stainless steel rods. *I²FG Workshop on Impulse Metalworking 2017, (November 29th, 2017, Berlin, Germany)*. http://www.join-em.eu/documents/I2FG%202017%20Join_EM.pdf
6. https://ec.europa.eu/clima/policies/strategies/2020_en#tab-0-1 (30.01.2018)
7. *United Nations* (Editor), Transforming our world: The 2030 agenda for sustainable development, *A/RES/70/1*, <https://sdgs.un.org/2030agenda>
8. Simoen, B., Faes, K., De, Waele, W. (2017) Investigation of the weldability of copper to steel tubes using the electromagnetic welding process. October 2017. *Intern. J. Sustainable Construction & Design* **8**(1):7, DOI: <https://doi.org/10.21825/scad.v8i1.6811> <https://ojs.ugent.be/SCAD/article/view/6811>
9. Satendra, Kumar, Kulkarni, M.R., Saroj, P.C., Mittal, K.C. (2013) Metallurgical and mechanical testing of electromagnetically welded copper and iron sample. *NDT.net Issue: 2014-02*. In: *Proc. of Asia Pacific Conf. on Non-Destructive Testing (14th APCNDT), (Mumbai, India, November 18–22, 2013)*. Session: NDE for Quality Control & Quality Assurance, <https://www.ndt.net/article/apcndt2013/papers/099.pdf>
10. Kore, S.D., Date, P.P., Kulkarni, S.V. Effect of process parameters on electromagnetic impact welding of aluminum sheets. *Intern. J. of Impact Engineering*, **34**, 1327–1341.
11. Khandaei, M., Vahidshad, Y., Ayaz, M. (2020) Improvement of weld quality in electromagnetic welding of aluminum-stainless steel sheets. *Materialwiss. Werkstofftech*, **51**(10), 1372–1388. DOI: <https://doi.org/10.1002/mawe.201900205>

ORCID

M.A. Polieschuk: orcid.org/0000-0002-5992-4641,
 I.V. Matveiev: orcid.org/0000-0003-0683-0761,
 V.O. Bovkun: orcid.org/0000-0001-7019-8671,
 A.Yu. Tunik: orcid.org/0000-0001-6801-6461,
 O.V. Cherkashin: orcid.org/0000-0001-9978-6848

CONFLICT OF INTEREST

The Authors declare no conflict of interest

CORRESPONDING AUTHOR

M.A. Polieschuk
 E.O. Paton Electric Welding Institute of the NASU
 11 Kazymyr Malevych Str., 03150, Kyiv, Ukraine
 E-mail: dep_6@paton.kiev.ua

SUGGESTED CITATION

M. Polieschuk, I. Matveiev, V. Bovkun, J. Selech, A. Tunik, O. Cherkashin, L. Kisterska, K. Siekierski (2022) Magnetic-pulse welding of copper rings with steel parts with the use of single-turn inductor. *The Paton Welding J.*, **1**, 14–17.

JOURNAL HOME PAGE

<https://pwj.com.ua/en>

Received: 29.10.2021
 Accepted: 07.02.2022

<https://doi.org/10.37434/tpwj2022.01.04>

IMPROVEMENT OF THE MECHANICAL PROPERTIES AND CORROSION RESISTANCE OF LASER WELDS ON THICK DUPLEX PLATES BY LASER CLADDED BUTTERING

A. StraÙe, A. Gumenyuk, M. Rethmeier

Bundesanstalt für Materialforschung und -prüfung (BAM)
Unter den Eichen 87, 12205 Berlin, Germany

ABSTRACT

Because of its excellent corrosion resistance, high tensile strength and high ductility, duplex stainless steel 2205 offers many areas of application. Though laser beam welding accompanied by high cooling rates, duplex steels tend to perform higher ferrite contents in weld metal as the base metal, which leads to a reduction of ductility and corrosion resistance of the weld joint. To overcome this problem, a solution, based on buttering the plate edges by laser metal deposition (LMD) with material containing higher Ni concentrations prior to laser welding was suggested. In this context different process parameters for LMD process were investigated. In a second step the possibility of welding those edges defect free while achieving balanced austenite-ferrite ratio was verified with metallographic analysis, Electron Backscatter Diffraction (EBSD) and impact testing according to Charpy. The improved corrosion resistance was observed with ASTM G48 standard test method.

KEY WORDS: laser metal deposition, laser beam welding, duplex stainless steel

INTRODUCTION

Laser beam welding of thick plates has great relevance for applications in the chemical and the offshore industry, where defect free weld seams with a homogenous microstructure are crucial. But often it is necessary to add filler materials to achieve the desired properties. A known problem with laser beam welding of thick plates is the decreasing detectability of the elements of said filler materials in the depth of the welds. Gook et al. [1] proved that up to a depth of 14 mm the elements are traceable, even if they are not transported uniformly through the molten pool, which results in weld seams with different properties between the upper and the lower part. An example for this is the duplex stainless steel 2205. Those steels are characterized by a balanced austenite-ferrite ratio, which is accompanied by the combined properties of both microstructures, an excellent ductility and tensile strength. Welding, especially laser beam welding, of those materials leads to a massive change of the austenite-ferrite ratio to a much higher ferrite content, up to 90 % and with that to changed properties of the weld seam in comparison to the base material, e.g. a reduced ductility as reported by Kotecki [2]. A solution for this problem is the usage of nitrogen for a better formation of the austenite phase. Lai et al., suggested the usage of nitrogen as shielding gas for laser welding processes, as the gas stabilizes the forming of austenite [3]. Another approach to reduce the ferrite content of the welds is the usage of filler

materials in form of electrodes with a higher Ni-content. This leads to a higher austenite ratio in the microstructure. Muthupandi et al. studied the influence of such electrodes for laser beam and electron beam welding processes [4]. Wu et al. used a powder nozzle to distribute nickel powder into the molten pool [5]. As mentioned, the filler material only reaches a depth of maximal 14 mm, this solution is only feasible for thinner plates. For thick plates Westin et al. [6] proposed nickel foils which were placed between both welding partners before the tacking, but the handling of foils is complicated and time consuming. In this paper another approach for the homogenous distribution of the filler material by laser clad buttering is proposed.

In the last years Laser Metal Deposition (LMD) became more important for different types of applications, for repair of components, e.g., of the tip of turbine blades and in the additive manufacturing of whole parts as well. Another common application is cladding of components with corrosion or wear resistant layers. In this study the edges of the welding partners were coated with a duplex steel and nickel powder mixture before the laser welding to ensure a homogenous distribution of the alloying elements in the laser weld seams, which must display a balanced duplex microstructure.

EXPERIMENTAL SETUP

Base plates with the dimensions 300×100×15 mm were of the duplex stainless steel 2205. For the LMD process, duplex powder 2205 with a grain size of

Table 1. Chemical composition (wt.%) of the investigated materials

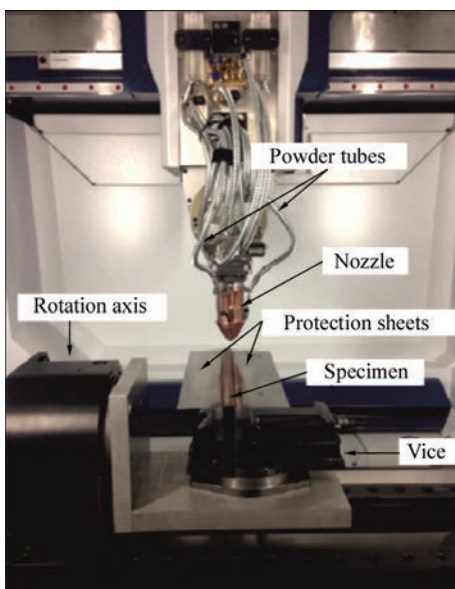
Material	Form	Fe	Cr	Ni	Mo	Nb	Mn	N	C	Si	P
Duplex (1.4462)	Base material	Bal.	22.96	5.18	3.00	–	1.82	0.17	0.02	0.29	0.03
Duplex (1.4462)	Powder	Bal.	22.80	5.57	3.16	–	1.09	0.16	0.02	0.68	0.02
Nickel (24.053)	Powder	–	–	Bal.	–	–	–	–	0.05	–	–

53–250 μm and nickel powder with a grain size of 45–125 μm were used.

Table 1 shows the chemical composition of the base material and the powders. The resulting powder mixture contained a 12 % total amount of nickel. The coatings of the plates' edges were produced in a five-axis laser cell (TruLaser Cell 3000, Trumpf), that is coupled with a 16 kW Yb:YAG-disk laser (TruDisk 16002, Trumpf) with a wavelength of 1030 nm. A three-jet nozzle with a working distance of 16 mm and a powder feeder (Flowmotion Twin, Medicoat) were used.

The cladding was done with a laser spot diameter of 1.6 mm, a constant powder mass flow of 15 $\text{g}\cdot\text{min}^{-1}$, a laser power of 0.8 kW, a velocity of 0.8 $\text{m}\cdot\text{min}^{-1}$ and a stepover of 1.5 mm. For all experiments the carrier gas was helium with a gas flow of 4 $\text{l}\cdot\text{min}^{-1}$ and shielding gas was argon with 10 $\text{l}\cdot\text{min}^{-1}$. The experimental setup is shown in Figure 1 and chemical composition in Table 1.

For a longer coverage of the edges with shielding gas, protection sheets were used on either side of the plate. Those were clamped in the vice about 1–2 mm under the base plate. One layer per edge was cladded using a bidirectional strategy. The stepover was chosen in respect with the intention to produce preferably smooth coatings for the following laser beam welding process. The tacking was done with a cladding track on the upper and the lower side of the weld seam. For


Figure 1. Experimental setup for the coatings

those tack welds the welding parameters were the same as for the clad layers.

The laser beam welding was performed with a 20 kW Yb-fiber laser (YLR-20000, IPG) with a wavelength of 1064 nm, a focus diameter of 0.56 mm and a beam parameter product of 11.2 $\text{mm}\cdot\text{mrad}$.

After the coating of the edges and the tacking, the plates were welded with different welding gases. Shielding gas and the gas in the dragging nozzle was always argon, for the root shielding nozzle the influence of argon was tested as well as nitrogen. The laser power was 14.3 kW by a speed of 1.5 $\text{m}\cdot\text{min}^{-1}$ with a defocusing of -5 mm. The experimental setup is shown in Figure 2.

Different destructive and non-destructive tests were executed on both kinds of weld seams, with and without coating, to ensure the quality of the coatings and the welds. Cross sections as well as electron backscatter diffraction (EBSD), impact testing according to Charpy and corrosion testing according to the ASTM G48-11 Method A were used to characterize their properties.

RESULTS AND DISCUSSION

The buttering of edges with twenty single tracks is shown in Figure 3. The optical analysis of the microstructure showed that the austenite-ferrite ratio of the coatings was balanced due to the higher nickel content of the powder.

The LMD-tracks were set closer than the usual overlap of 30 % to realize an even surface. Other ste-

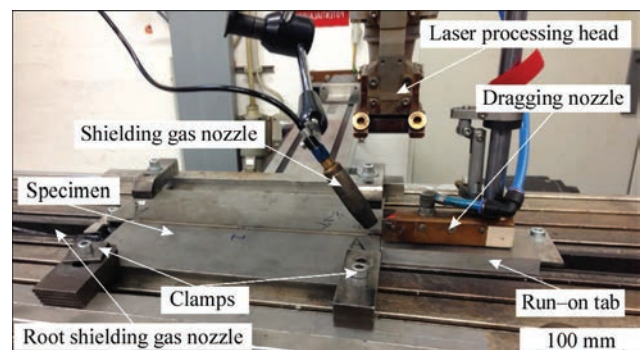

Figure 2. Experimental setup for the laser welds

Figure 3. Cross section of buttering of edges



Figure 4. Microsection of weld seam with LMD-tacking

pothers with a more moderate space between the lines were tested as well, but they resulted in surfaces, that were too uneven for the laser welding process. However, the edges display a certain waviness and a dipping at the corners, which proved to be problematic with the laser beam welding, were a technical zero-gap is preferred. Thus, the weld seams showed irregularities in the upper and the root side. To overcome this problem, LMD-tacking with the same parameter set as the buttering was applied on both sides of the coated plates to fill the gaps instead of the typical tacking with laser beam at the beginning, in the middle and at the end of the plates. The weld seam with this tacking showed a good appearance with only minimal relapse on the root side, shown in Figure 4.

The optical and EBSD-analysis of the weld seams with coated edges displayed a significantly better austenite-ferrite ratio than the ones which were welded without any filler material. For the last ones, the seams showed an austenite content below 10 %, whereas the austenite-ferrite ratio of the welds with the coated edges was balanced, with 40–50 % austenite, depending on the root shielding gas. Figure 5 shows a part of an EBSD-analysis of one of the weld seams. The ferrite phase was colored red, while the austenite is shown in blue. The amount of austenite measured with EBSD for this weld was 41.8 %. Those, that were performed with nitrogen as root shielding gas, displayed a higher austenite content up to 56.8 %, which affirms the discoveries of Lai et al.

Impact testing was executed by means of undersize Charpy-V samples with the dimensions 7.5×10×55 mm. The notch was placed in the middle of the weld seam and the testing performed at a temperature of –20 °C. Specimens welded with and without buttering were compared. The surface of the unbuttered ones implied brittle fractures (Figure 6, a) with an average impact toughness of 29 J·cm⁻², whereas the buttered ones displayed a far more ductile fracture behavior with values of 140 J·cm⁻² (Figure 6, b). The results show, that due to the buttering the weld seams show satisfactory ductility in contrast to that of unbuttered ones.

The corrosion testing was done with the standard testing method according to ASTM G48 for pitting corrosion for stainless steels in chlorite containing

environments. The testing was done at 25 °C for 24 hours in a FeCl₃·6H₂O (6 % FeCl₃ by mass)-testing solution. The specimen size was 55×25×15 mm. No corrosion was observed in the base metal in any of the tests. The ferritic weld seam of the uncoated specimen (Figure 7, a, b) showed corrosion in the weld metal. While the coated test pieces showed no corrosion, neither in the base metal nor in the weld seam (Figure 7, c, d). The proposed two-step process with the LMD-coated edges of the plates with a powder mixture containing 12 % nickel is able to form weld seam that are corrosion resistant.

CONCLUSIONS

Laser beam welding of 15 mm thick duplex plates LMD-coated with a powder mixture containing 12 % nickel was performed. The cross-sections as well as the EBSD-analysis showed a balanced duplex structure throughout the whole weld seam. The austenite content in the welds with nitrogen as shielding gas was higher by 15 %. The impact testing of the specimen confirmed the better ductility of the weld seams with coated edges and the defect free corrosion testing specimen confirmed the superiority of the mechanical properties as well.

ACKNOWLEDGEMENTS

This work was supported by the Federation of Industrial Research Association (AiF, project number 19.228N) and the German Federal Ministry for Economic Affairs and Energy (BMWi-Bundesministerium für Wirtschaft und Energie) based on a resolution of the Deutscher Bundestag. The authors want to thank Butting GmbH and personally Mr. M. Schlundt kindly for providing the base material as well as for performing the corrosion testing.

Additionally, the authors want to thank Mr. R. Saliwan Neumann (Department 5.1 — Materialography, Fractography and Ageing of Engineered Materials, BAM) for the EBSD measurements.

REFERENCES

1. Gook, S., Gumenyuk, A., Rethmeier, M. (2014) Hybrid laser arc welding of X80 and X120 steel grade. *Sci. and Technol. of Welding and Joining*, 19(1), 15–24.
2. Kotecki, D.J. (1986) Ferrite control in duplex stainless steel weld metal. *Welding Research Suppl.*, 65(10), 273–278.
3. Lai, R., Cai, Y., Wu, Y. et al. (2016) Influence of absorbed nitrogen on microstructure and corrosion resistance of 2205

duplex stainless steel joint processed by fiber laser welding. *J. of Materials Proc. Technology*, **231**, 397–405.

4. Muthupandi, V., Bala Srinivasan, P., Shankar, V. et al. (2005) Effect of nickel and nitrogen addition on the microstructure and mechanical properties of power beam processed duplex stainless steel (UNS 31803) weld metals. *Materials Letters*, **59(18)**, 2305–2309.
5. Wu, H.C., Tsay, L.W., Chen, C. (2004) Laser beam welding of 2205 duplex stainless steel with metal powder additions. *ISIJ Intern.*, **44(10)**, 1720–1726.
6. Westin, E.M., Stelling, K., Gumenyuk, A. (2011) Single-pass laser-GMA hybrid welding of 13.5 mm thick duplex stainless steel. *Welding in the World*, **55**, 39–49.

CONFLICT OF INTEREST

The Authors declare no conflict of interest

CORRESPONDING AUTHOR

A. Gumenyuk

Bundesanstalt für Materialforschung und -prüfung (BAM), Unter den Eichen 87, 12205 Berlin, Germany. E-mail: andrey.gumenyuk@bam.de

SUGGESTED CITATION

A. Straße, A. Gumenyuk, M. Rethmeier (2022) Improvement of the mechanical properties and corrosion resistance of laser welds on thick duplex plates by laser clad buttering. *The Paton Welding J.*, **1**, 18–21.

JOURNAL HOME PAGE

<https://pwj.com.ua/en>

Received: 28.10.2021

Accepted: 07.02.2022

<https://doi.org/10.37434/tpwj2022.01.05>

ELECTRON BEAM WELDING OF ALUMINIUM 1570 ALLOY AND MECHANICAL PROPERTIES OF ITS JOINTS AT CRYOGENIC TEMPERATURES

V.V. Skryabinskyi¹, V.M. Nesterenkov¹, A.V. Mykytchyk²

¹E.O. Paton Electric Welding Institute of the NASU
11 Kazymyr Malevych Str., 03150, Kyiv, Ukraine

²SE “International Center for Electron Beam Technologies
of the E.O. Paton Electric Welding Institute of the NAS of Ukraine”
68 Antonovych Str., 03150, Kyiv, Ukraine

ABSTRACT

The features of electron beam welding of the 1570 alloy were studied and mechanical properties of its welded joints in the temperature range of 20–293 K were investigated. It was found that during electron beam welding in the 1570 alloy, the width of the heat-affected-zone does not exceed 4 mm from the fusion line, which is 4 times lower than in the AMg6N alloy. In the weld, fusion zone and HAZ cracks, clusters of eutectic interlayers and other defects were not detected. The ultimate strength of the joints of the 1570 alloy at a decrease in the test temperature from 293 to 20 K increases from 325 to 525 MPa. The yield limit is also increased from 210 to 270 MPa, and the ductility changes slightly. At the same time, the impact toughness decreases from 38 to 9 J/cm². The strength coefficient of welded joints with a decrease in the test temperature from 293 to 20 K increases from 0.85 to 0.95. In general, the 1570 alloy is well welded by electron beam and the method of electron beam welding can be recommended in the manufacture of welded structures of rockets and spacecrafts.

KEY WORDS: electron beam welding, aluminium alloy, mechanical properties, welded joints; cryogenic temperatures

INTRODUCTION

The high-strength 1570 alloy of the Al–Mg system is designed to replace the AMg6 alloy in welded structures of rockets and spacecrafts. The use of the AMg6 alloy is explained by its advantages such as high ductility and corrosion resistance at a satisfactory weldability. The main disadvantage of this alloy is its relatively low strength [1]. The difference between the 1570 and AMg6 alloy is that it is additionally doped with the scandium element in the amount of 0.17–0.27 % and has higher mechanical properties. For alloys of the Al–Mg system, the most effective hardener is scandium [2]. High mechanical properties of the alloy are predetermined by the formation of fine-dispersed reinforcing particles of the Al₃Sc phase, precipitated during heating and deformation from the supersaturated solid solution. In terms of yield strength, semi-finished products from the 1570 alloy are 1.5–2.0 times higher than similar semi-finished products from the AMg6 alloy, depending on the type of semi-finished product. The use of the 1570 alloy instead of the AMg6 alloy gives an advantage in weight by up to 20 % [1].

The addition of scandium to alloys of the Al–Mg system improves their weldability. For example, their resistance to hot crack formation during fusion welding significantly increases [1, 3]. The strength coefficient of welded joints of the 1570 alloy is 0.85–0.95 depending on the type of semi-finished product. It was found that short-term heating of the near-weld zone of the 1570 alloy to 450 °C is not accompanied by a decrease in hardness [4]. Even at long-term heating (2–10 h), recrystallization processes in the 1570 alloy begin at the temperatures above 400–500 °C, depending on the type of semi-finished product [5]. This is explained by a high thermal stability of the nonrecrystallized structure, predetermined by the precipitation of secondary particles of the Al₃Sc phase from the supersaturated solid solution during thermomechanical treatment of the alloy.

One of the main ways to join the structural elements of rocket engineering from aluminium alloys is electron beam welding (EBW). The aim of this work is to study the features of EBW of the 1570 alloy and study the mechanical properties of its welded joints in the temperature range of 20–293 K.

RESEARCH METHODS AND EQUIPMENT

The research was carried out on stamped semi-finished products of the 1570 alloy with a thickness of 30, 40 and 60 mm. Semi-finished products were welded in the electron beam welding machine UL 209M

¹Based on the materials of the report at the X International Conference “Beam Technologies in Welding and Materials Processing”, Odessa, September 6–10, 2021.

with a power source ELA 60/60 with an accelerating voltage of 60 kV. Hardness measurements were used to evaluate changes in the strength of the weld metal and the width of the heat-affected-zone (HAZ). The Rockwell device was used with a load on a steel ball of 600 N on the scale B. The microstructures of welded joints were examined on cross-sections with the use of the Neophot optical microscope.

The mechanical properties of the stamped semi-finished product of the 1570 alloy and its welded joints were determined at temperatures of 20, 77, 196 and 293 K. Standard specimens of GOST 11150–84 type 1 No.2 (for tests at low temperatures) and specimens with a notch of the same diameter of the working part were tested. Impact strength was determined during tests of specimens with Charpy notch.

EXPERIMENTAL STUDIES AND RESULTS

During welding, the beam current and the focusing lens current were selected from the condition of a guaranteed penetration and formation of the back weld bead. EBW modes for semi-finished products of different thicknesses are shown in the Table 1.

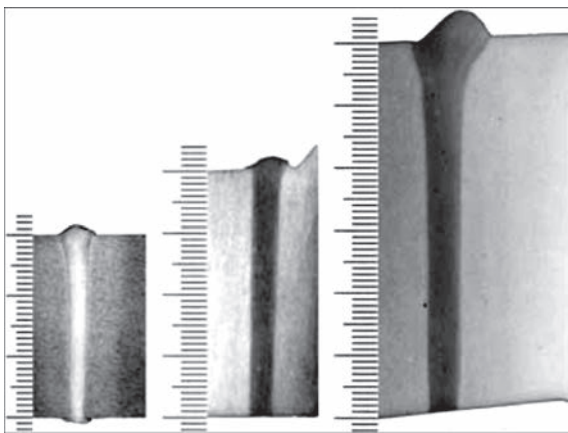


Figure 1. Macrosections of joints of semi-finished products of the 1570 alloy with a thickness of 30, 40 and 60 mm

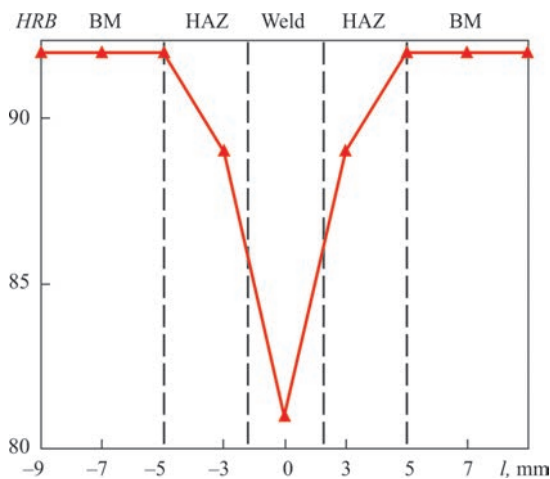


Figure 2. Distribution of hardness in the cross-section of joints of stamped semi-finished products of the 1570 alloy

Table 1. EBW modes for welding of semi-finished products of the 1570 alloy of different thickness, mm

Thickness of semi-finished product, mm	EBW modes for the 1570 alloy			
	U_{acc} , kV	v_w , mm/s	I_{beam} , mA	Beam scan amplitude, mm
30	60	14–17	220–280	1.0–1.5
40		14–17	270–330	1.0–1.5
60		10–12	360–420	1.5–2.0

Welds had a width from 3 to 5 mm with almost parallel boundaries of the penetration zone in the central and lower part (Figure 1). Spraying, splashing and leaking of liquid metal during EBW process were not observed.

During EBW of the 1570 alloy, the width of the HAZ does not exceed 4 mm from the fusion line (Figure 2) regardless of the thickness of the welded semi-finished products (see Table). This is 4 times less than in EBW of the AMg6N alloy [6].

The weld metal has a homogeneous highly-dispersed cellular-dendritic structure (Figure 3). In the weld, fusion zone and HAZ no cracks clusters, of eutectic interlayers and other defects were found.

With a decrease in the test temperature from 293 to 20 K, the ultimate strength of the base metal of the 1570 alloy increases from 385 to 535 MPa (Figure 4). The yield limit also increases from 245 to 310 MPa. The relative elongation decreases from 24 to 15 %

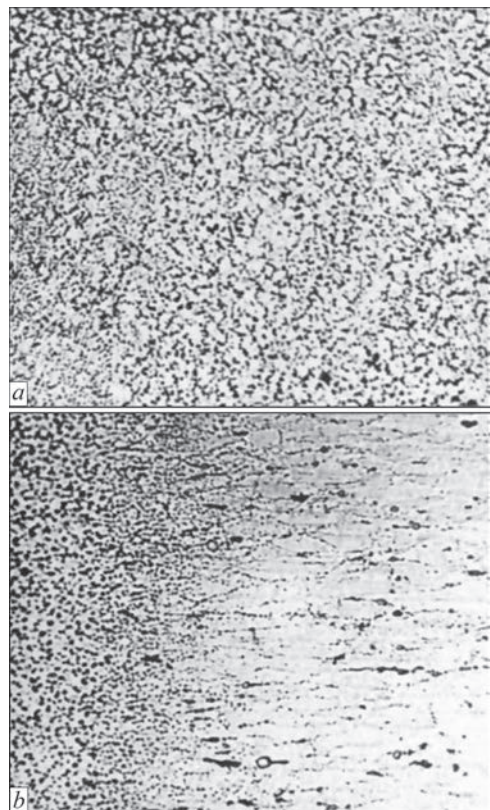


Figure 3. Microstructure ($\times 200$) of weld metal of stamped semi-finished product of the 1570 alloy: *a* — central part of the weld; *b* — fusion line

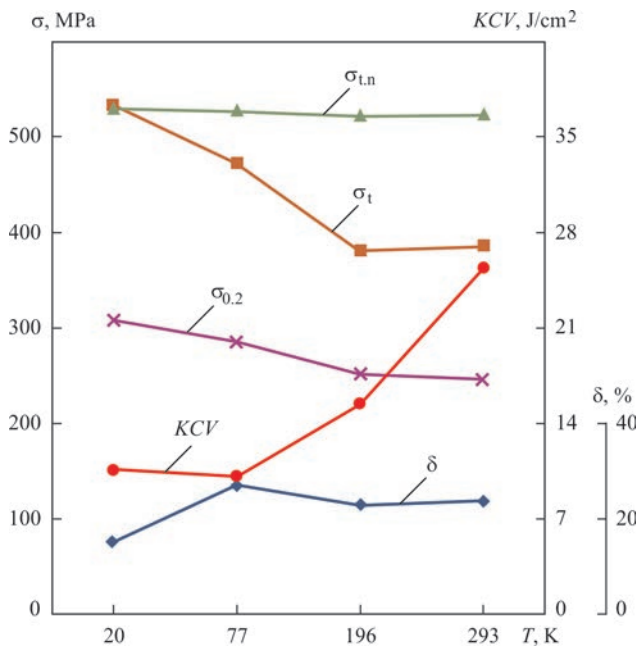


Figure 4. Dependence of mechanical properties of stamped semi-finished product of the 1570 alloy with a thickness of 60 mm on the test temperature

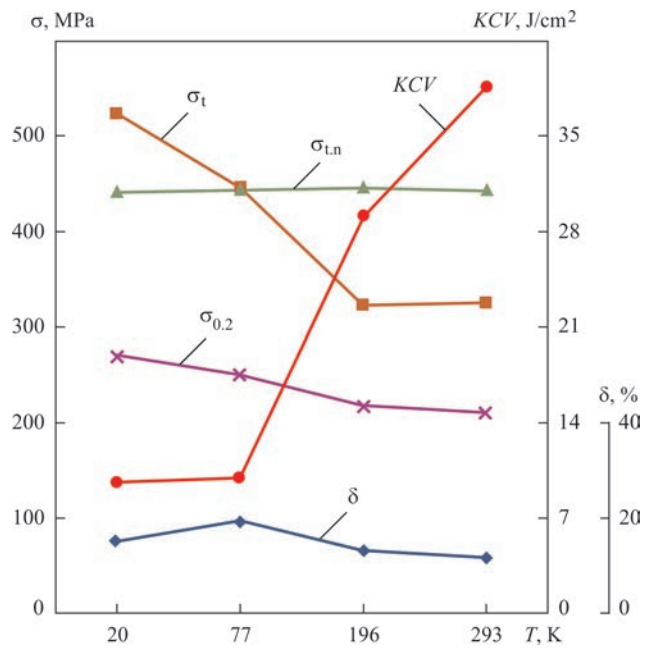


Figure 6. Dependence of mechanical properties of welded joints of the 1570 alloy, made by EBW method, on test temperature

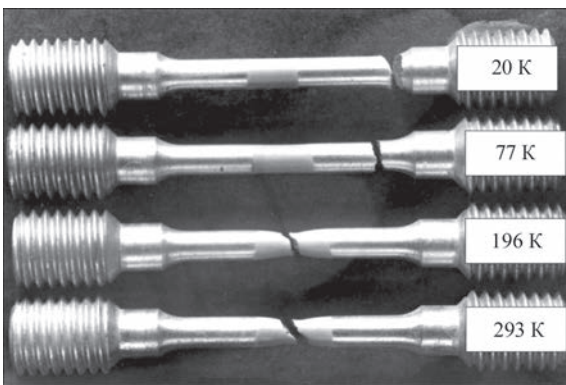


Figure 5. Nature of destruction of specimens cut from welded joints of stamped semi-finished product of the 1570 alloy at different test temperatures

and the impact toughness decreases from 25 to 10 J/cm². The ultimate strength of the notched specimens is about 525 MPa and is almost independent of the test temperature.

The peculiarity of the tests of welded joints of the 1570 alloy is that at the test temperatures of 20 and 77 K, the specimens are destroyed over the base metal outside the HAZ (Figure 5). The ultimate strength of the smooth specimens becomes higher than the ultimate strength of the specimens with a notch and at 20 K it reaches 525 MPa (Figure 6). At the same time, impact toughness of the weld metal decreases from 38 to 9 J/cm². The ultimate strength of the rupture specimens with a notch of the weld metal amounts to about 443 MPa at all test temperatures.

At a decrease in the test temperature from 293 to 20 K, the strength coefficient of welded joints increases from 0.85 to 0.95 (Figure 7). The sensitivity of the

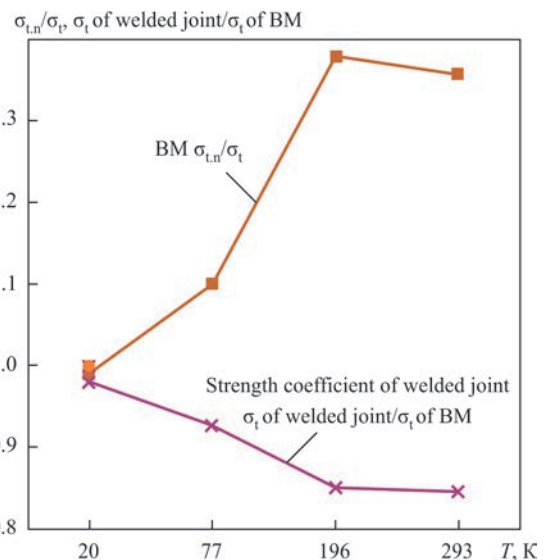


Figure 7. Effect of test temperature on strength coefficient of joints and sensitivity to stress concentrators of stamped semi-finished product of the 1570 alloy

metal to stress raisers is evaluated by the ratio of the ultimate strength of the specimen with a notch to the ultimate strength of the smooth specimen ($\sigma_{t,n}/\sigma_t$). The sensitivity to the notch of the base metal and the weld metal is low. The ratio $\sigma_{t,n}/\sigma_t$ at temperatures of 293 and 196 K is not lower than 1.3. With a decrease in temperature, the sensitivity of the base metal to the notch increases, but even at a temperature of 20 K the ratio $\sigma_{t,n}/\sigma_t$ amounts to about one.

CONCLUSIONS

The investigations of microstructure and mechanical properties of joints of stamped semi-finished products of the 1570 alloy, made by EBW method, were car-

ried out. No defects were found in the welded joints. The width of the HAZ amounts up to 4 mm from the fusion line and almost does not depend on the thickness of the semi-finished product to be welded. At a decrease in the test temperature from 293 to 20 K, the strength coefficient of welded joints increases from 0.85 to 0.95.

Thus, it was found that the 1570 alloy is well welded by electron beam and the EBW method can be recommended in the manufacture of welded structures of rockets and spacecrafts.

REFERENCES

1. Ovchinnikov, V.V. (2017) Prospects of development of high-technological wrought aluminium alloys for welded structures. Pt 3. *Mashinostroenie i Inzhenernoe Obrazovanie*, **4**, 44–60 [in Russian]. https://old.mospolytech.ru/mio/rus_1547816839.pdf
2. Filatov, Yu.A. (2014) Alloys of Al–Mg–Sc system as a special group of wrought aluminium alloys. *Tekhnologiya Lyogkikh Splavov*, **2**, 34–41 [in Russian].
3. Panteleev, M.D., Bakradze, M.M., Skupov, A.A. et al. (2018) Technological peculiarities of fusion welding of aluminium alloy V-1579. *Aviats. Materialy i Tekhnologii*, **3**(52), 11–17 [in Russian]. https://journal.viam.ru/en/system/files/uploads/pdf/2018/2018_3_2_1.pdf
4. Nesterenkov, V.M., Skryabinskyi, V.V., Rusynyk, M.O. (2021) Effect of thermal cycles in electron beam welding of aluminium 1570 alloy on mechanical properties of welded joints. *The Paton Welding J.*, **5**, 35–40. <https://doi.org/10.37434/tpwj2021.05.06>
5. Koryagin, Yu.D., Iliin, S.I. (2017) Peculiarities of recrystallization of wrought aluminium-magnesium alloys with scandium. *Vestnik YuUrGU, Metallurgiya*, **17**(1), 65–72 [in Russian]. <https://cyberleninka.ru/article/n/osobennosti-rekristallizatsii-deformiruemyh-alyuminiy-magnievyyh-splavov-so-skandiem/viewer>
6. Bondarev, A.A., Skryabinsky, V.V. (1985) Influence of technological factors on softening zone of AMg6N alloy in electron beam welding. *Avtomatich. Svarka*, **3**, 40–42 [in Russian].

ORCID

V.V. Skryabinskyi: orcid.org/0000-0003-4470-3421,
V.M. Nesterenkov: orcid.org/0000-0002-7973-1986,
A.V. Mykytchyk: orcid.org/0000-0002-9761-9429

CONFLICT OF INTEREST

The Authors declare no conflict of interest

CORRESPONDING AUTHOR

V.V. Skryabinskyi
E.O. Paton Electric Welding Institute of the NASU
11 Kazymyr Malevych Str., 03150, Kyiv, Ukraine
E-mail: skriabinski.vv.555@gmail.com

SUGGESTED CITATION

V.V. Skryabinskyi, V.M. Nesterenkov, A.V. Mykytchyk (2022) Electron beam welding of aluminium 1570 alloy and mechanical properties of its joints at cryogenic temperatures. *The Paton Welding J.*, **1**, 22–25.

JOURNAL HOME PAGE

<https://pwj.com.ua/en>

Received: 29.10.2021

Accepted: 07.02.2022

<https://doi.org/10.37434/tpwj2022.01.06>

INFLUENCE OF TIME OF EXISTENCE OF MOLTEN POOL IN ELECTRON BEAM PROCESSES ON THE LEVEL OF EVAPORATION OF ELEMENTS WITH A HIGH VAPOR TENSION

N.V. Piskun, E.L. Vrzhyzhevskiy, V.A. Kostin, T.G. Taranova, I.L. Bogaichuk, I.I. Statkevych

E.O. Paton Electric Welding Institute of the NASU
11 Kazymyr Malevych Str., 03150, Kyiv, Ukraine

ABSTRACT

The intermetallic Ti-44Al-5Nb-3Cr-1.5Zr alloy (at.%), developed and melted at the E.O. Paton Electric Welding Institute of the NAS of Ukraine, was studied. The processes of evaporation of elements with a high vapor tension, such as aluminium and chromium for two electron beam processes: melting and welding were studied. It was experimentally proven and confirmed by investigations that the use of directional crystallization by electron beam melting, which takes place in deep vacuum conditions, does not allow providing uniformity of structure along the length of the ingot, which is associated with evaporation of elements with a high vapor tension, such as aluminium and chromium. It was found that during electron beam welding of specimens of intermetallic Ti-44Al-5Nb-3Cr-1.5Zr alloy (at.%), cracks appeared, but, as was proved by X-ray spectral studies, evaporation of elements does not occur. The parameters of these two processes were compared and it was shown that the level of evaporation of elements with a high vapor tension in electron beam processes is influenced by the time of staying the material in a liquid state and the sizes of the molten zone.

KEY WORDS: intermetallic alloy of TiAl system, electron beam melting, electron beam welding, evaporation, elements with a high vapor tension, molten zone, crystallization time

INTRODUCTION

It is known that heat-resistant intermetallic alloys have high strength, heat resistance, creep and corrosion resistance at high temperatures [1]. Thanks to a low density and specific strength, intermetallics based on γ -TiAl are attractive for the use in gas turbine engines [2]. Due to unique properties, they are also promising for using in various other industries. For example, manufacture of low-pressure turbine blades from these alloys allows saving 180 kg for each engine as compared to traditional materials [3]. This, in turn, allows reducing the cost of products of aerospace industry, which is very important.

However, a low ductility at room temperature and a low manufacturability, associated with the latter, complicates and in some cases even excludes the possibility of manufacturing semi-finished products and products from these materials. A widespread use of titanium aluminides in the structures of different purpose depends to a large extent on the creation of effective methods for their manufacturing and subsequent processes of their mechanical and heat-mechanical treatment.

Since the use of TiAl titanium aluminides is promising for its wide application in the structures of aircraft engine turbines, parts of the automotive industry and some other industries [4], then the introduction of intermetallic alloys largely depends on the devel-

opment of technologies of their joining. In parts and assemblies of gas turbine engines, it is possible to use welding in order to simplify their manufacturing. The most suitable method for producing intermetallic joining is electron beam welding [5], which allows welding products of different geometric shapes and producing welds of different extension. In addition, as compared to other types of fusion welding, it has the following advantages: first, since it is carried out in a high vacuum, it fully protects such an active material as titanium; secondly, in electron beam welding, a narrow weld and a very small heat-affected zone are formed, which, in turn, should lead to minimal deformations of welded joint.

Therefore, the development and optimization of welding technology, the creation of new approaches to the welding process in order to produce defectless joints is very relevant.

The main problem with the use of electron beam processes for the manufacture and treatment of titanium alloys is vacuum evaporation of elements with a high vapor tension [6, 7]. These elements include, in the first turn, aluminium and chromium. Since aluminium is one of the main elements of the alloy, its evaporation affects the structure and, accordingly, mechanical properties of the alloy.

The aim of the work is to study the influence of electron beam zone melting modes and electron beam welding of intermetallic Ti-44Al-5Nb-3Cr-1.5Zr al-

Table 1. Chemical composition of experimental alloy

Alloy	Ti	Al	Nb	Cr	Zr
wt.%	52.82	28.8	11.72	3.51	3.16
at.%	45.92	44.54	5.26	2.82	1.46

loy (at.%) on the processes of evaporation of alloying elements and formation of microstructure and properties.

MATERIAL AND PROCEDURE OF RESEARCH

In the work, the intermetallic alloy of the following composition was investigated: Ti-44Al-5Nb-3Cr-1.5Zr (at.%) (Table 1), which was developed and melted at the E.O. Paton Electric Welding Institute of the NAS of Ukraine (PWI) [8].

Specimens for the study were produced after electron beam crucibleless zone melting (Figure 1) and after electron beam welding (Figure 2).

At a room temperature, cast intermetallic alloys of the TiAl system represent low ductility materials and during their testing to a uniaxial tension, a fracture of the specimen occurs immediately in an elastic area after tension.

It is known that before using cast intermetallic to eliminate these defects, it should be subjected to gas static isothermal compression (GSIC), long-term heat treatment or rolling [9]. One of the methods to improve the structure and increase mechanical characteristics of intermetallic is a directed crystallization.

For conducting research, the method of crucibleless electron beam zone melting was used (Figure 1).

In our opinion, the use of a crucibleless electron beam melting method is quite promising for the mentioned purposes, because it has a number of distinguishing features:

- high thermal efficiency (efficiency of the process reaches 90 %), which is associated with a small power consumption;

- the indicated method makes it easy to regulate and maintain a set length of the molten zone, which is essential in developing both scientific bases and practical realization of the process;

- treatment of materials can be carried out in a wide range of temperatures — 250–2200 °C, which allows remelting an intermetallic alloy having a melting point of 1460 °C;

- this method allows an easy control of a beam with its direct influence on a specimen. Scanning the beam along the molten zone with a certain frequency and amplitude can, respectively, change the temperature gradient of specimens in the process of melting.

It is also noticeable that after a directed recrystallization, GSIC treatment is not required, because in the

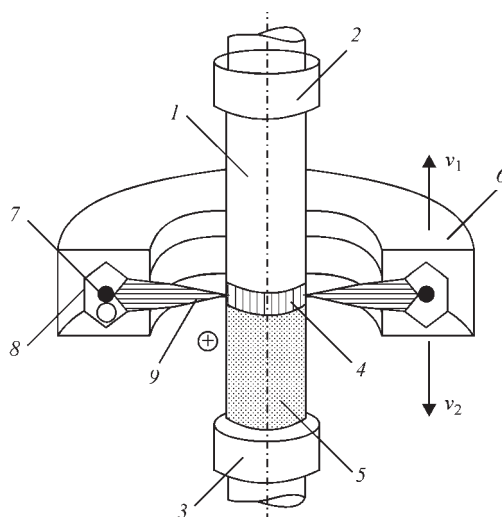


Figure 1. Scheme of the method of crucibleless electron beam zone melting: 1 — molten specimen; 2 — upper holder; 3 — lower holder; 4 — molten zone; 5 — remelted area; 6 — electron beam heater; 7 — cathode; 8 — focusing device; 9 — electron beam

produced ingots such microdefects as discontinuities, microcracks, etc. are absent; the porosity is absent, because shrinkage goes directed at the front of crystallization and not in the volume of the ingot. It allows providing its uniform structure along the length of the ingot. In addition, the conditions of the process provide the purity of the material that is melted (there is no interaction with the material of the crucible).

As was mentioned above, for the further use of this alloy in industry, the technology of electron beam welding (EBW) of intermetallic of the following nominal composition of Ti-44Al-5Nb-3Cr-1.5Zr (at.%) was developed. That was the same alloy, which was tried to be treated by the method of electron beam melting.

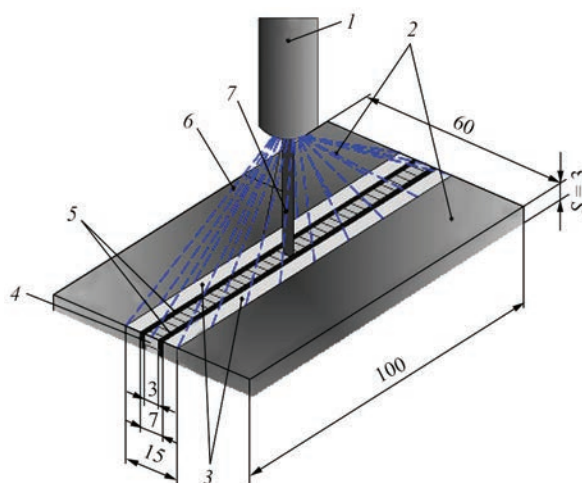


Figure 2. Scheme of the process of electron beam welding of plates of intermetallic Ti-44Al-5Nb-3Cr-1.5Zr alloy (at.%) in the welding chamber of the UL-144 installation: 1 — electron beam gun; 2 — base material; 3 — zone of local heat treatment; 4 — weld; 5 — heat-affected zone; 6 — deployed beam of electrons; 7 — electron welding beam

The experiments on electron beam welding of intermetallic were performed in the welding chamber of the UL-144 installation according to the scheme shown in Figure 2.

Electron beam welding was performed without heating in the following mode: $U_{acc} = 60$ kV; $I_b = 35$ mA; $v_w = 7$ mm/s; $P = 5 \cdot 10^{-3}$ Pa.

While producing welded joints of intermetallics of the TiAl system by the EBW method, their significant disadvantage is the possibility of cold crack formation, that occur at temperatures below 700 °C.

RESEARCH RESULTS

ELECTRON BEAM CRUCIBLELESS ZONE MELTING

During the technological experiments on electron beam crucibleless melting of intermetallic of the TiAl system, a strong evaporation from the molten zone and areas of the heated solid surface, occurred. Unfortunately, the evaporated elements were deposited on assemblies of the electron beam heater, including such an important assembly as a tantalum spiral that simulates electrons; illuminator glass panes; chamber walls; fittings, which led to the impossibility of completing the process.

Micro-X-ray spectral examinations showed that in the process of electron beam melting of the in-

termetallic of the system Ti–44Al–5Nb–3Cr–1.5Zr (at.%), a strong evaporation of aluminium — one of the main components of the alloy occurs, which has a high vapor tension. This occurs from the molten zone and areas of a solid surface that are heated. In addition, chromium, included in titanium aluminide as an alloying element, also evaporates quite intensively. The studies of the chemical composition of titanium aluminide, subjected to recrystallization during crucibleless electron beam melting, showed that from the material up to 20 % of aluminium and up to 18 % of chromium evaporate.

Examinations of the structure of titanium aluminide ingots produced by electron beam crucibleless melting (Figure 3) showed that the structure contains areas of two types: light- and dark-etched coarse equilibrium grains (Figure 3, *a*).

The examination of the microstructure of the ingot showed the presence of areas of the specimen in which the colonies of lamellae of the γ -phase are located in different directions (Figure 3, *b*). Figure 3, *c* presents the macrostructure of the cross-section of the specimen. Tiny pores are observed, from which microcracks propagate to the central part of the specimen, which is apparently caused by intense evaporation of aluminium. On the opposite edge of the cross-section of the specimen (Figure 3, *d*), the areas

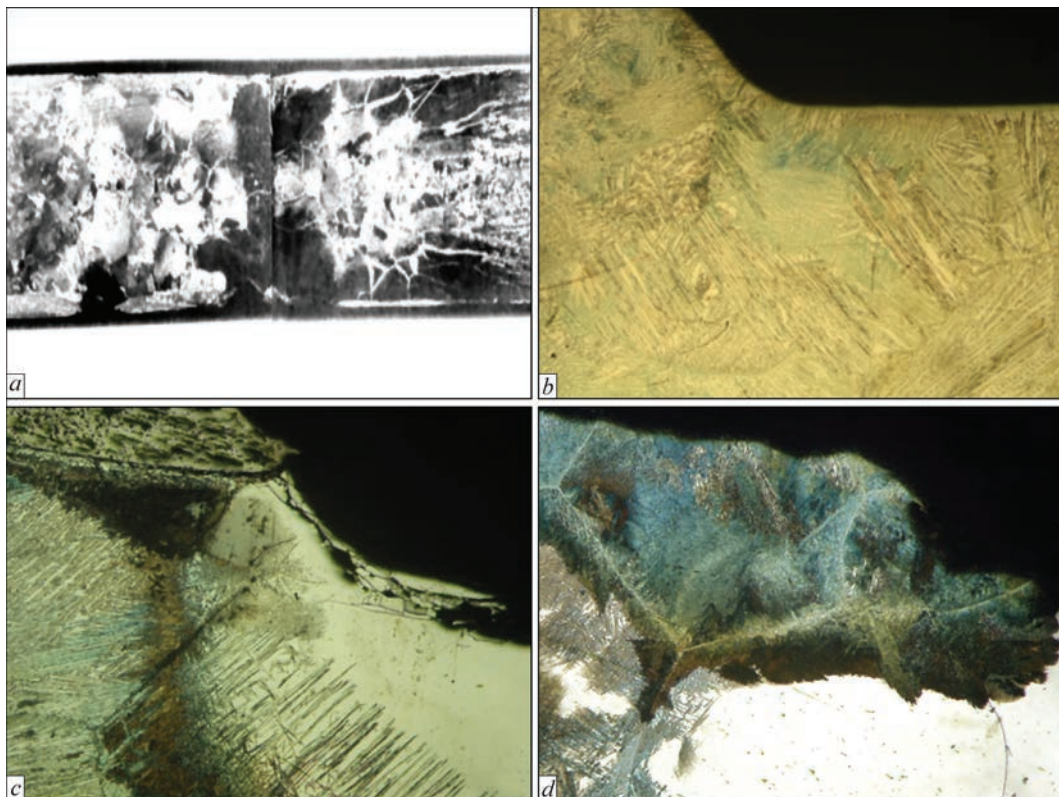


Figure 3. Structure of titanium aluminide ingots produced by electron beam crucibleless zone melting: *a* — macrostructure of investigated specimens; *b* — specimen area, on which the colonies of lamellae of the γ -phase are seen, located in different directions; *b*, *c*, *d* — macro- and microstructure of the cross-section of the specimen after zone remelting

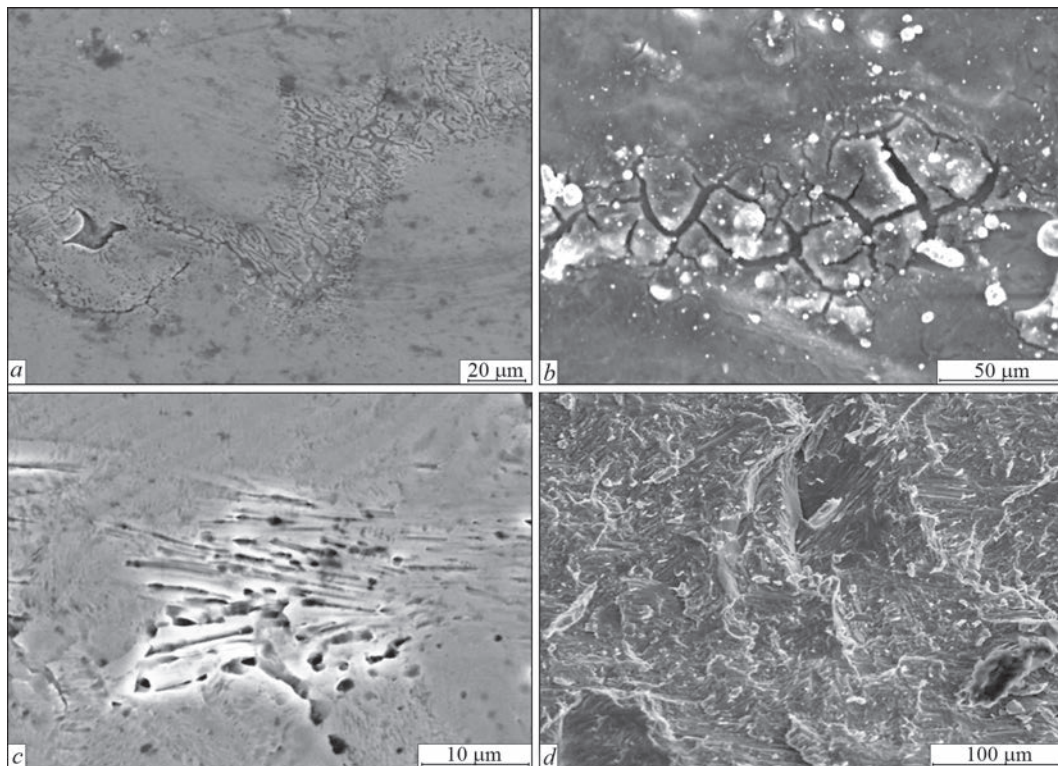


Figure 4. Fractographic studies of specimens of intermetallic Ti-44Al-5Nb-3Cr-1.5Zr alloy (wt.%) after electron beam zone melting: *a-c* — regions of the pore bottom of intermetallic; *d* — fracture surface of the pore bottom of intermetallic

of coarse grains are located, consisting of a mixture of $\gamma+\alpha_2$ -phase.

The micro-X-ray spectral analysis of the bottom of the pore, performed in the electron scanning microscope JSM-840, showed that the assumptions made above were correct (Figure 4). Fractographic studies of specimens of intermetallic Ti-44Al-5Nb-3Cr-1.5Zr alloy (at.%) after electron beam zone melting showed the presence of a large number of pores (Figure 4, *c*).

Examinations showed that at the boundaries of the pore, the aluminium content drops to 18–20 at.% as compared to 46–47 wt.% in the matrix. At the bottom of the pores, the areas of the film with a high aluminium content were found. At some points, the aluminium content reached 59 wt.%. It is possible, that the formation of aluminium oxides occurred in these places (Figure 4, *b*). During a detailed study of fractures, the areas in the form of microscopic particles were found. As was shown by X-ray spectral analysis, the chromium content in these precipitations reached 18 %. For comparison — in the alloy, the chromium content is 3 %.

ELECTRON BEAM WELDING OF INTERMETALLIC ALLOY

Examination of welded butt joints after electron beam welding (EBW) showed that in the weld, transverse cold cracks (Figure 5, *a*) are observed, which pass through the welded joint and end on both sides of the specimen on the base material. It is necessary to note

the heterogeneity of the structure of the weld metal in the form of colonies of the $(\gamma+\alpha_2)$ -phase, which are located along the fusion zone and have a microhardness of 5110–5270 MPa. In this area, numerous cracks with a length from 100 to 300 μm were revealed, located parallel to the fusion line (Figure 5, *b*).

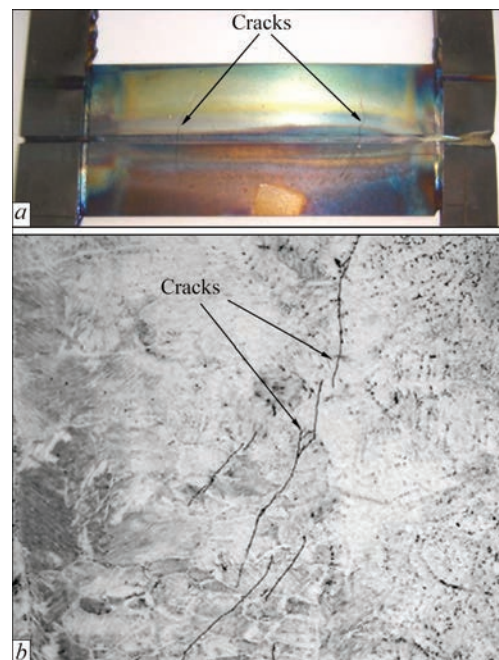


Figure 5. Specimen of welded joint of intermetallic Ti-44Al-5Nb-3Cr-1.5Zr alloy (at.%), produced by electron beam welding: *a* — general appearance; *b* — microstructure ($\times 200$) of weld metal

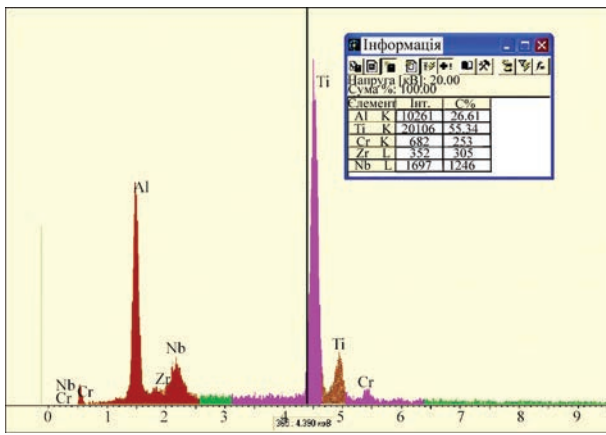


Figure 6. Quantitative analysis of welded joint zone of intermetallic of the Ti–44Al–5Nb–3Cr–1.5Zr system (wt.%)

As it was found above, if in electron beam melting a considerable evaporation of aluminium (to 20 %) and chromium (to 18 %) occurs, and in electron beam welding cracks appear, it became necessary to determine the reasons of cold crack formation. This may be associated with the problem of evaporation of elements during electron beam welding, which leads to changes in the composition of aluminium or chromium.

In order to determine the possible evaporation of the alloy elements in the process of electron beam welding, a quantitative X-ray spectral analysis of the intermetallic welded joint produced by the EBW method was performed.

The results of the quantitative analysis of the welded joint elements of the intermetallic Ti–44Al–5Nb–3Cr–1.5Zr (at.%) are presented in Figure 6.

Investigation of evaporation of elements in the process of welding is almost not observed. Difference in the elemental composition occurs in aluminium by 2.2 % and in chromium by 1 %. In this case, the redistribution of element components in the weld and titanium occurs approximately by 2.5 % higher than in the initial condition. Chromium and aluminium are the elements with a high vapour tension, and alumin-

ium, in addition, has a low boiling point and manages partially to evaporate in the welding process.

On the surface of the welded joint of the intermetallic of the Ti–44Al–5Nb–3Cr–1.5Zr system (at.%), performed by EBW, parallel formations are observed both in the base metal as well as in the weld metal (Figure 7, a).

The thickness of these phases amounts to 1.36–2.5 μm. Cracking in these phases is not observed. Quantitative analysis of the phases showed that they are enriched in titanium (Figure 7, b).

DISCUSSION

COMPARISON OF MODES OF THE ELECTRON BEAM MELTING PROCESS AND ELECTRON BEAM WELDING OF THE Ti–44Al–5Nb–3Cr–1.5Zr ALLOY

Thus, according to the data of chemical analysis and structural examinations, as well as on the basis of a detailed study of literary sources devoted to the topic of evaporation of elements with a high vapour tension in electron beam processes [6, 7], it was concluded that using the method of crucibleless electron beam melting, it is not possible to produce high-quality ingots. In connection with the abovementioned, it was decided to apply an induction heating in argon, that allowed solving all problems with evaporation of elements and producing high-quality ingots [10, 11].

As showed the results of previous studies, the main source of cracks arising is a low ductility of intermetallic at room temperatures (the temperature of viscous-brittle transition is 700 °C) and inability to resist the appearance of cracks as a result of formation of welding stresses.

In order to prevent cold crack formation in welded joints of specimens of titanium aluminide and to form a high-quality weld, it was necessary to carry out a preheating heating of the specimens [12, 13] and the next local heat treatment by an electron beam, deployed in the one and the other direction. It was

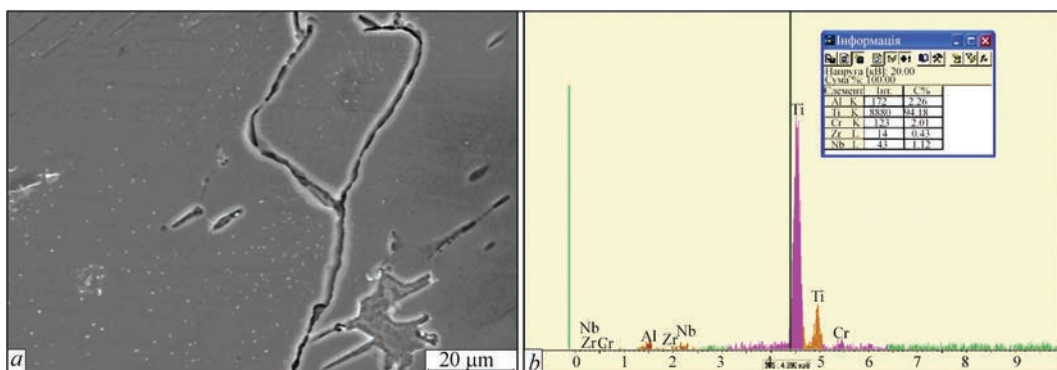


Figure 7. Phases formed in EBW of intermetallic of the Ti–44Al–5Nb–3Cr–1.5Zr system (wt.%) in the weld metal: a — microstructure; b — spectral analysis of phases

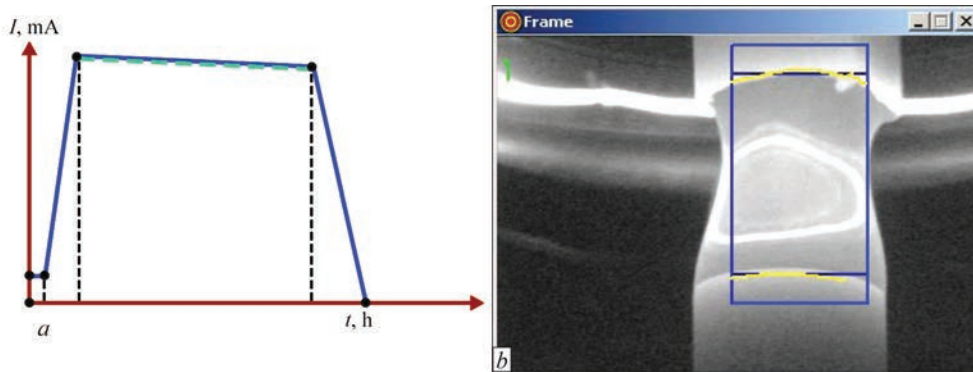


Figure 8. Characteristics of electron beam melting process: *a* — thermal cycle of the process of zone melting of intermetallic; *b* — size of molten zone in the process of zone melting is 10 mm

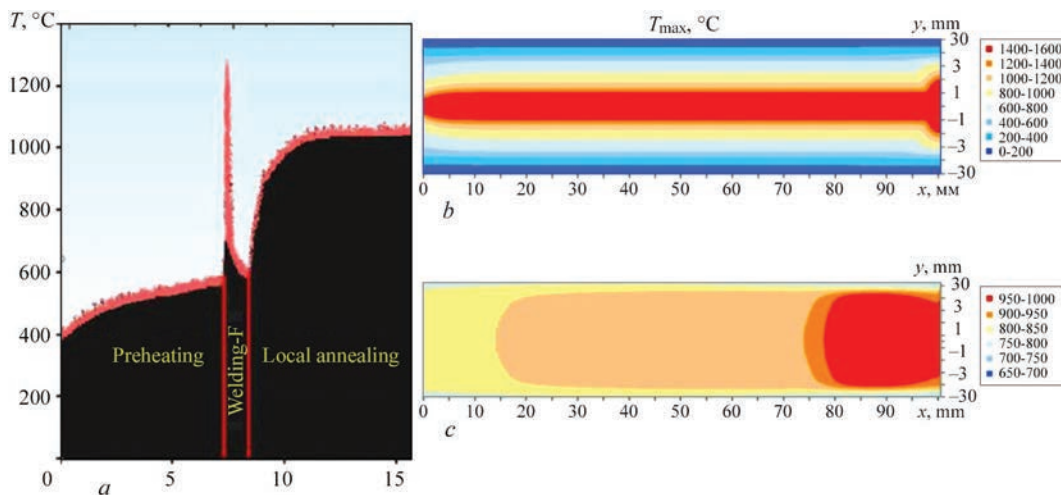


Figure 9. Characteristics of the process of electron beam welding: *a* — thermal cycle of EBW process for welding intermetallic; *b* — calculation of temperature distribution in the weld of intermetallic with the thickness of 3 mm in the process of EBW; *c* — calculation of temperature distribution in the weld of intermetallic within 1 s after the end of welding process

numerically shown and experimentally confirmed that the use of a distributed source of a preheating of the specimen before welding allows realizing favorable conditions during welding and during further cooling, namely, reducing the value of tensile stresses by 30 %. In addition, during use of this technology, a phase transformation occurs, due to which an additional β -(B2)-phase appears in the structure, which represents an ordered phase based on Ti. It is located on the boundaries of colonies and blocks the initiation and propagation of cracks in the α_2 -phase as a result of stress reduction. The formation of a favorable three-component structure: γ -phase, $(\gamma + \alpha_2)$ -phase and β -phase in the weld contributes to increase in its strength and ductility [14, 15].

To answer the question, why during two electron beam vacuum processes for the same alloy, absolutely different behavior of elements with a high vapour tension was observed, a comparison of basic characteristics of these processes was conducted. Figures 8, 9 show the characteristics of the process of electron beam melting and electron beam welding.

As is seen from Figure 7, in electron beam melting at a speed of 50 mm/h, the duration of staying the material in a liquid state is 720 s. At a small thickness of welded material, it can be accepted that geometric dimensions of the welding pool in arc and electron beam welding are approximately equal [16].

To evaluate the average duration of staying the metal in a liquid state during electron beam welding, the formulas were used given in [17], and the dimensions of the welding pool, which are usually accepted for arc welding of titanium with a thickness of 3 mm. By the calculations, it was found that the welding pool in electron beam welding stays in a liquid state approximately for 0.7 s, which is more than 700 times lower than in electron beam melting.

In addition, the width of the molten zone, which is crystallized in electron beam melting, is 10 mm (Figure 7, *b*), which is much more than in the process of electron beam welding, in which the width of the weld with the heat-affected zone is not more than 3 mm. And already in a second after the end of the welding process (Figure 9, *c*), the temperature in the weld drops by 500 °C.

CONCLUSIONS

It was found that in the process of electron beam melting of the intermetallic Ti–44Al–5Nb–3Cr–1.5Zr alloy, a strong evaporation of elements occurs, that have a high vapour tension: aluminium to 20 % and chromium to 18 %. Since aluminium is one of the main components of alloy elements, its evaporation affects the structure. In electron beam welding, such a phenomenon is not observed.

As compared to thermocycles of two electron beam processes, it turned out that duration of staying the material in a liquid state during electron beam melting is 720 s, width of the molten zone is 10 mm, and in electron beam welding, a welding pool, which is crystallized in 0.7 s, has dimensions of approximately 2 mm.

Thus, the level of evaporation of elements with a high vapour tension in electron beam processes depends on duration of staying the material in the liquid state and sizes of the molten zone.

REFERENCES

- Schwaighofer, E., Clemens, H., Mayer, S., et al. (2014) Microstructural design and mechanical properties of a cast and heat treated intermetallic multiphase γ -TiAl based alloy. *Intermetallics*, **44**, 128–140. DOI: <https://doi.org/10.1016/j.intermet.2013.09.010>
- Bewlay, B.P., Nag, S., Suzuki, A., Weimer, M.J. (2016) TiAl alloys in commercial aircraft engines. *Material: High Temp.*, **33**, 549–559. DOI: <https://doi.org/10.1080/09603409.2016.1183068>
- Clemens, H., Mayer, S. (2016) Intermetallic titanium aluminides in aerospace applications processing, microstructure and properties. *Material: High Temp.*, **33**, 560–570. DOI: <https://doi.org/10.1080/09603409.2016.1163792>
- Kablov, E.N., Lukin, V.I. (2008) Intermetallic based on titanium and nickel for advanced engineering product. *The Paton Welding J.*, **11**, 65–71.
- Chernobaj, S.V. (2013) Welding of titanium aluminide alloys (Review). *Ibid.*, **8**, 25–30.
- Varich, I.Yu., Akhonin, S.V., Trigub, N.P. et al. (1997) Evaporation of aluminium from titanium-based alloys during cold-hearth electron beam melting. *Problemy Spets. Elektrometallurgii*, **4**, 15–21 [in Russian].
- Paton, B.E., Trigub, N.P., Akhonin, S.V. et al. (2006) *Electron beam melting of titanium*. Kiev, Naukova Dumka [in Russian].
- Zhuk, G.V., Trigub, N.P., Zamkov, V.N. (2003) Producing of titanium gamma-aluminide ingots using EBTHM method. *Advances in Electrometallurgy*, **4**, 19–21.
- Imaev, V.M., Imaev, R.M., Khismatullin, T.G. (2008) Mechanical properties of intermetallic alloy Ti–43Al–7(Nb, Mo)–0.2B (at.%) after heat treatment. *Fizika Metallov i Metallovedenie*, **105**(5), 516–522 [in Russian]. DOI: <https://doi.org/10.1134/S0031918X08050098>
- Kartavykh, A.V., Asnis, E.A., Piskun, N.V. et al. (2015) Microstructure and mechanical properties control of γ -TiAl(Nb, Cr, Zr) intermetallic alloy by induction float zone processing. *J. of Alloy and Compounds*, **643**, 182–166. DOI: <https://doi.org/10.1016/j.jallcom.2014.12.210>
- Kartavykh, A.V., Asnis, E.A., Piskun, N.V. et al. (2017) Room-temperature tensile properties of float-zone processed β -stabilized γ -TiAl(Nb, Cr, Zr) intermetallic. *J. Materials Letters*, **188**, 88–91. DOI: <https://doi.org/10.1016/j.matlet.2016.10.103>
- Kim, Y.-W., Smarsly, W., Lin, J. et al. (2014) Electron beam joining of γ -titanium aluminide. *Gamma Titanium Aluminide Alloys 2014. The Minerals, Metals & Materials Society*, 99–103.
- Vrzhyzhevskiy, E.L., Piskun, N.V., Taranova, T.G. et al. (2019) Prevention of cold cracks formation during electron-beam welding of alloy based on TiAl system intermetallic compound. *Tekhnologicheskie Sistemy*, **86**(1), 43–49 [in Russian]. DOI: <https://doi.org/10.29010/86.6>
- Tang, B., Qi, X.S., Kou, H.C. et al. (2016) Recrystallization behavior at diffusion bonding interface of high Nb containing TiAl alloy. *Advanced Engineering Materials*, **18**(4), 657–664. DOI: <https://doi.org/10.1002/adem.201500457>
- Yang, K.L., Huang, J.C., Wang, Y.N. (2013) Phase transformation in the β -phase of super a2 Ti₃Al base alloys during static annealing and super plastic deformation at 700–1000 °C. *Acta Mater.*, **51**, 2577–2594. DOI: [https://doi.org/10.1016/S1359-6454\(03\)00057-0](https://doi.org/10.1016/S1359-6454(03)00057-0)
- Paton, B.E. (1987) *Electron beam welding*. Kyiv, Naukova Dumka [in Russian].
- Petrov, G.L., Tumarev, A.S. (1977) *Theory of welding processes: Manual for higher educ. inst.*, 2nd Ed. Moscow, Vysshaya Shkola [in Russian].

ORCID

N.V. Piskun: 0000-0003-1459-2310
 E.L. Vrzhyzhevskiy: 0000-0001-8651-8510,
 V.A. Kostin: 0000-0002-2677-4667
 T.G. Taranova: 0000-0002-2656-4693,
 I.I. Statkevych: 0000-0001-9403-2123

CONFLICT OF INTEREST

The Authors declare no conflict of interest

CORRESPONDING AUTHOR

N.V. Piskun
 E.O. Paton Electric Welding Institute of the NASU
 11 Kazymyr Malevych Str., 03150, Kyiv, Ukraine
 E-mail: E-mail: nadamova54@gmail.com

SUGGESTED CITATION

N.V. Piskun, E.L. Vrzhyzhevskiy, V.A. Kostin, T.G. Taranova, I.L. Bogaichuk, I.I. Statkevych (2022) Influence of time of existence of molten pool in electron beam processes on the level of evaporation of elements with a high vapor tension. *The Paton Welding J.*, **1**, 26–32.

JOURNAL HOME PAGE

<https://pwj.com.ua/en>

Received: 25.10.2021
 Accepted: 07.02.2022

<https://doi.org/10.37434/tpwj2022.01.07>

MATHEMATICAL MODELING OF RESIDUAL STRESSES IN COMPOSITE WELDED JOINTS OF WWER-1000 REACTOR VESSEL COVER WITH CSS NOZZLES

A.A. Makarenko, O.V. Makhnenko

E.O. Paton Electric Welding Institute of the NASU
11 Kazymyr Malevych Str., 03150, Kyiv, Ukraine

ABSTRACT

Composite welded joints (CWJ) of the WWER-1000 reactor vessel cover with the nozzles of the control safety system (CSS) is the object of calculations of strength in the feasibility study of life extension of NPP power units. Kinetics of formation of residual stresses in welding CWJ of the WWER-1000 reactor vessel cover with the CSS nozzles and also their redistribution as a result of postweld heat treatment were calculated by mathematical modeling using finite element method. Effect of preheating on microstructural phase transformations in the HAZ of base material of the cover and nozzle was studied. The main features of residual stress distribution in CWJ after welding and after heat treatment were determined.

KEY WORDS: composite welded joint, reactor vessel cover, WWER-1000, HAZ, microstructural phase transformations, residual stresses, heat treatment, mathematical modeling

INTRODUCTION

One of the most important issues of safe operation and extension of the life of equipment of nuclear power plants (NPPs) in Ukraine is the issues of evaluation of strength, integrity and serviceability of welded joints, which requires data on residual stresses.

In the elements of equipment and pipings of existing NPPs, the so-called composite welded joints (CWJ) of dissimilar materials, usually steels of ferritic-pearlitic (or bainitic) and austenitic classes, were widely used. The peculiar feature of CWJ consists in the fact, that due to the difference in the chemical composition of the base and welding materials during welding heating, a significant diffusion of chemical elements in the joining area can occur, causing chemical and structural heterogeneity of CWJ metal [1, 2], and also due to a significant difference in the coefficients of thermal expansion in the materials of the constituent components in the process of welding and postweld heat treatment, significant unrelaxed residual stresses occur [3, 4]. Structural heterogeneity of CWJ metal and unrelaxed residual stresses significantly affect strength, service life and corrosion resistance of equipment elements [5]. Significant difficulties in the experimental measurement of unrelaxed residual stresses complicate their accounting when determining the life of equipment elements in NPPs.

The reactor vessel is one of the main elements, on the technical condition of which the life of safe operation of a nuclear power plant depends and which

cannot be replaced. Welded joints in reactor vessel are problem areas, where the risk of defects has a high probability. While much attention was paid to the welded joints and deposits of the WWER-1000 reactor vessel, CWJ of the reactor vessel cover with the nozzles of the control safety system (CSS) almost were not studied. In addition to evaluation of structural integrity of the vessel cover in CWJ areas during long-term operation, analysis of the possibility of repair replacement of nozzles by welding technology in case of its wear also represents interest in the future.

DESIGN AND TECHNOLOGY OF CWJ OF VESSEL COVER WITH CSS NOZZLES

Figure 1 shows a scheme of welded joint of the cover of the WWER-1000 reactor vessel, which is formed by joining the CSS nozzle of steel 20 (pearlite class) and the reactor vessel cover of steel 15Kh2NMFA (bainite class) by welding material 10Kh16N25AM6 (austenite class), with the preliminary cladding 3I0-8 (austenite class). The inner surface of the CSS nozzles is insulated from the contact with the heat carrier by welded-on jackets of steel 08Kh18N10T. Welding of a jacket onto the nozzles was carried out during heating of a jacket and a nozzle to the temperature of 100 °C. On the lower part (ends) of the nozzles, an austenitic layer is deposited. In the Table 1 materials are shown, which were used in the manufacture of cover and nozzles of the upper block of the power unit WWER-1000 reactor [6–8].

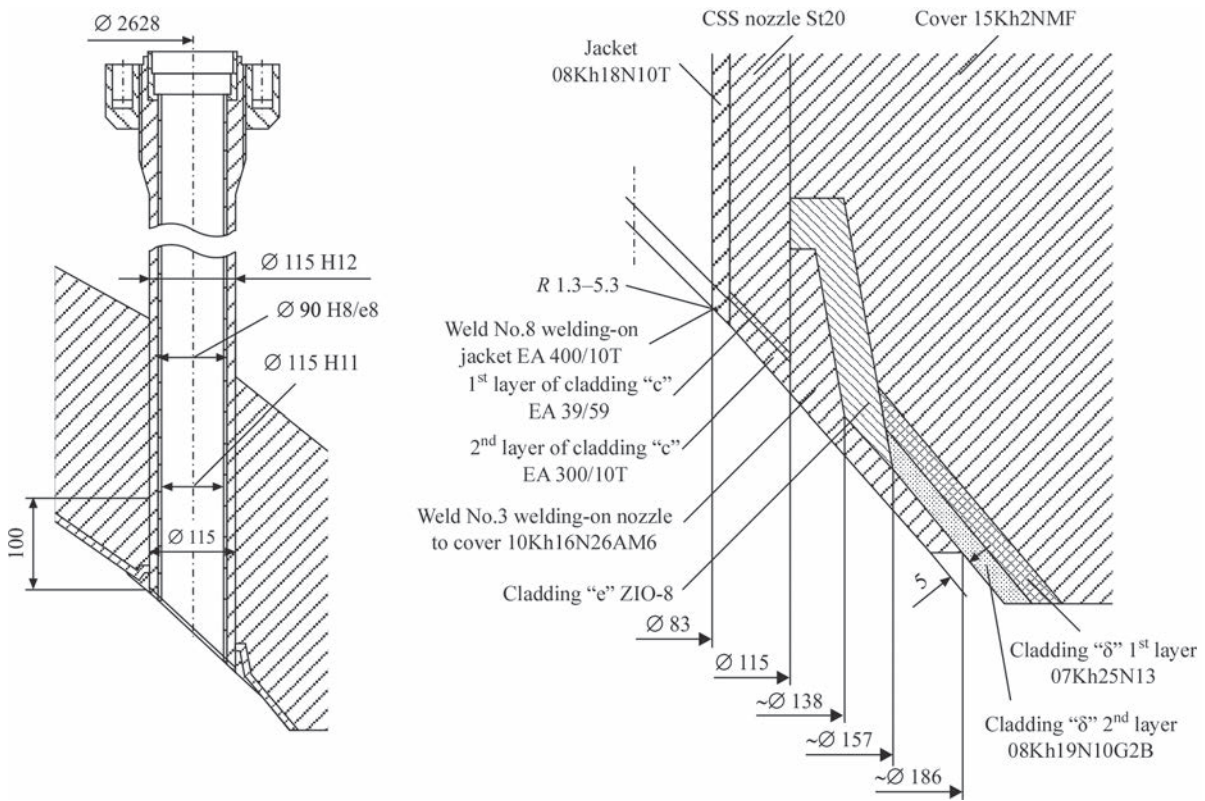


Figure 1. Reactor cover element with connected CSS nozzle and scheme of CWJ

DEVELOPMENT OF MATHEMATICAL MODEL OF SSS IN WELDING CWJ

To calculate the residual stresses, a 2D finite element model of joining the cover of the reactor vessel with a CSS nozzle, admitting axial symmetry (Figure 1), was constructed. The scheme of the model of the welded joint, boundary conditions and finite element mesh are shown in Figures 2, 3.

The temperature problem was solved, admitting a fast-moving heating source, which allowed using a two-dimensional finite element model in the cross-section of the welded joint (Figure 2). For sim-

ulation of temperature distributions while producing welding passes, an equation of non-stationary thermal conductivity was used, which includes taking into account the volumetric welding source of heating $W(x, y, t)$ [9]

$$\frac{\partial}{\partial x} \left(\lambda \frac{\partial T}{\partial x} \right) + \frac{\partial}{\partial y} \left(\lambda \frac{\partial T}{\partial y} \right) + W(x, y, t) = c\rho \frac{\partial T}{\partial t}, \quad (1)$$

where ρ is the density of material; c is the specific heat capacity; λ is the coefficient of thermal conductivity; T is the temperature of material,

$$W(x, y, t) = \frac{6Q}{ab\sqrt{\pi}} \exp \left(\frac{-3(x-x_0)^2}{a^2} - \frac{-3(y-y_0)^2}{b^2} \right), \quad (2)$$

Table 1. Materials used for the welded joint of the reactor cover with the CSS nozzles of the WWER-1000 reactor power unit [6–8]

Parts of cover with nozzles	Grade of material
Basic materials	
Reactor cover	15Kh2NMFA
CSS nozzles	20
Jacket of CSS nozzles	08Kh18N10T
Welding (cladding) materials	
Weld for welding-on CSS nozzles to the cover (No.3)	Sv-10Kh16N26AM6 and 3I0-8
Lower weld for welding-on jacket to the nozzle with cladding (No. 8)	EA-400/10T
1 st layer of cladding “c” to the nozzle	EA-395/9
2 nd layer of cladding “c” to the nozzle	EA-400/10T
Cladding “e” on the cover	ZIO-8
1 st layer of cladding “d” on the cover	07Kh25N13
2 nd layer of cladding “d” on the cover	08Kh19N10G2B

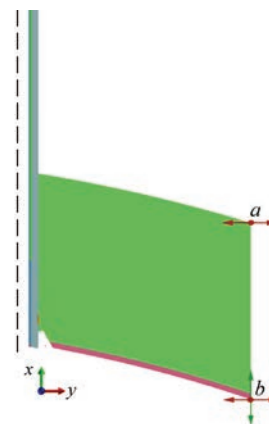


Figure 2. Boundary conditions and scheme of 2D model of CWJ: a — restricts movement in the horizontal plane; b — restricts movement in the horizontal and vertical planes

where Q is the effective power of the welding source of heating; x_0, y_0 are the coordinates of the center of the heating source; a, b are the corresponding dimensions (width and depth) of the effective heating zone in the directions x, y .

The time of heating the metal of each welded or deposited pass in the cross-section of the welded joint depends on the speed of welding v_w and the size of the effective heating zone a , i.e., in the first approximation it can be equal to $t_w = a/v_w$.

The parameters of the welding source of heating were chosen in such a way that the temperature of the metal in the weld exceeded the melting point, and the time interval between the passes was sufficient to cool the metal to the temperature of the accompanying heating.

The boundary conditions on the surfaces of welded joint elements taking into account the convection heat transfer with the environment were specified in the form:

$$q = -h(T_{\text{out}} - T), \quad (3)$$

where T_{out} is the temperature of the environment; q is the heat flow; h is the coefficient of heat transfer from the surface at the convection heat exchange with the environment.

Initial conditions at $t = 0$:

$$\begin{aligned} W(x, y, 0) &= 0, \quad T_{\text{heating}} = 20\text{--}200 \text{ }^\circ\text{C}, \\ T_{\text{out}} &= 20 \text{ }^\circ\text{C}, \end{aligned} \quad (4)$$

where T_{heating} is the temperature of preliminary and accompanying heating.

Taking into account the hypothesis of “plane deformation”, the solution of the distribution of spatial components of stresses and deformations was obtained by means of a two-dimensional model of the cross-section of the welded joint in an elastoplastic formulation, i.e., a deformation tensor can be presented in the form of the tensors:

$$\varepsilon_{ij} = \varepsilon_{ij}^e + \varepsilon_{ij}^p \quad (i, j = x, y, z), \quad (5)$$

where ε_{ij}^e is the tensor of elastic deformations; ε_{ij}^p is the tensor of plastic deformations.

The components of stress tensors σ_{ij} and elastic deformations ε_{ij}^e are connected with each other by the Hooke's law:

$$\varepsilon_{ij}^e = \frac{\sigma_{ij} - \delta_{ij}\sigma}{2G} + \delta_{ij}(K\sigma + \varphi), \quad (6)$$

where δ_{ij} is a single tensor ($\delta_{ij} = 0$ if $i \neq j$, $\delta_{ij} = 1$, if $i = j$), $\sigma = \frac{1}{3}(\sigma_{xx} + \sigma_{yy} + \sigma_{zz})$; $G = \frac{E}{2(1+\nu)}$ shear modulus; $K = \frac{1-2\nu}{E}$ is the compliance of a volume

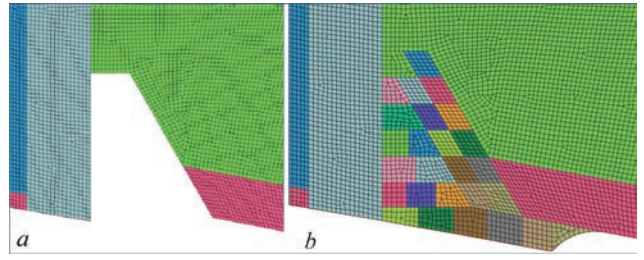


Figure 3. Finite element mesh in the CWJ zone: *a* — before welding; *b* — after welding

compression; E is the Young modulus; ν is the Poisson's ratio; φ is the function of free relative elongations (volumetric changes) caused by changes in temperature and microstructural phase changes.

In a simple case, when structural transformations do not occur:

$$\varphi = \alpha(T - T_0), \quad (7)$$

where α is the coefficient of relative temperature elongation of the material.

In welding of steels that are sensitive to the thermal cycle of welding, in HAZ structural transformations with noticeable volumetric changes may occur. Their taking into account mainly affects the kinetics of distribution of welding stresses and deformations. The total effect of volumetric changes from the temperature T_0 to $T(t)$ is determined in the form [9]:

$$\begin{aligned} \Delta\varphi &= \frac{\sum V_j(T, t)\gamma_j(T) - \sum V_j(T_0)\gamma_j(T_0)}{\sum V_j(T_0)\gamma_j(T_0)} \\ (j &= A, F, P, B, M), \end{aligned} \quad (8)$$

where j phase is austenite, ferrite-pearlite, bainite, martensite; $\gamma_j(T)$ is the volume of the unit of mass of the j^{th} phase at the temperature T ; $V_j(T)$ is the fraction (in fractions from the unit) of the j^{th} phase at the temperature T .

The values $\gamma(T)$ for low-alloy steels are given depending on carbon content C , % [10]:

$$\begin{aligned} \gamma_A(T) &= 0.12282 + 8.56 \cdot 10^{-6}(T - 20) + \\ &+ 2.15 \cdot 10^{-3} C, \quad (\text{cm}^3/\text{g}); \\ \gamma_M(T) &= 0.12708 + 4.448 \cdot 10^{-6}(T - 20) + \\ &+ 2.79 \cdot 10^{-3} C, \quad (\text{cm}^3/\text{g}); \end{aligned} \quad (9)$$

$$\gamma_{B,FP}(T) = 0.12708 + 5.528 \cdot 10^{-6}(T - 20), \quad (\text{cm}^3/\text{g}).$$

The results of calculation of the mass fraction of each $V_j(T)$ phase in the final microstructure after cooling depend on the cooling rate in the characteristic range of temperatures (cooling rate from the temperature 800 to 500 $^\circ\text{C}$).

Kinetics of changing the value $V_j(T)$ in the temperature range from T_s^j beginning of the appearance of the j^{th} phase to T_e^j — end of the appearance of the

j^{th} phase when the austenite decomposition is determined on the basis of ratios:

$$V_j(T) = V_j^{\max} \left[1 - \exp \left(a_j \frac{T_{sj} - T}{T_{sj} - T_{ej}} \right) \right] \quad (10)$$

$$a_j = -2.7 \quad (j = M, \text{FP}, B);$$

$$V_a(T) = 1 - \sum_{i, \delta i, \dot{a}} V_j(T); \quad (11)$$

where $V_a(T)$ is the content of residual austenite at a temperature T .

The values of the temperatures of start T_{sj} and end T_{ej} of the types of j phase transformations were determined according to existing thermokinetic diagrams or the diagrams of the anisothermal decomposition of austenite (ADA) of the relevant steels.

Plastic deformations are associated with the stressed state of the equation of the theory of plastic nonisothermal flow, associated with the von Mises yield criterion:

$$d\varepsilon_{ij}^p = d\lambda \cdot (\sigma_{ij} - \delta_{ij}\sigma) \quad (i, j = x, y, z), \quad (12)$$

where $d\varepsilon_{ij}^p$ is the tensor increment of the tensor ε_{ij}^p at a given moment of time t , predetermined by the history of deformation, stresses σ_{ij} and temperature T ; $d\lambda$ is the scalar function, which is determined by the flow conditions in the following form:

$$\begin{aligned} d\lambda &= 0, \text{ if } f = \sigma_i^2 - \sigma_T^2(T) < 0 \text{ or } f = 0, \\ &\quad \text{at } df < 0; \\ d\lambda &> 0, \text{ if } f = 0 \text{ i } df > 0; \\ &\text{state } f > 0 \text{ is unacceptable,} \end{aligned} \quad (13)$$

where σ_i is the intensity of stresses

$$\sigma_i = \frac{1}{\sqrt{2}} \sqrt{(\sigma_{xx} - \sigma_{yy})^2 + (\sigma_{xx} - \sigma_{zz})^2 + (\sigma_{yy} - \sigma_{zz})^2 + 6(\sigma_{xy}^2 + \sigma_{xz}^2 + \sigma_{yz}^2)},$$

$\sigma_T = (T)$ is the yield strength of material at a temperature T .

Equation (8) shows, that in order to obtain the results on residual stress components σ_{ij} and deformations ε_{ij} it is necessary to consider the process of propagation of elastoplastic deformations by time, starting from some initial state. For this purpose, a method of consistent tracing is traditionally used when for the moment t the solution is sought when a complete solution for the moment $(t - \Delta t)$ is known, where Δt is a step of tracing the propagation of elastoplastic deformations, within which it can be approximately supposed that the development occurs according to a fairly simple load trajectory. In this case, the relation between the end increments of the tensor of deforma-

tions $\Delta\varepsilon_{ij}$ and the tensor of stresses σ_{ij} according to [9], it can be written in the form:

$$\Delta\varepsilon_{ij} = \psi(\sigma_{ij} - \delta_{ij}\sigma) + \delta_{ij}(K\sigma) - b_{ij}, \quad (14)$$

where ψ is the function of the state of material at the point (x, y, z) at the moment t .

$$\psi = \frac{1}{2G}, \text{ if } f < 0,$$

$$\psi > \frac{1}{2G}, \text{ if } f = 0, \quad (15)$$

state $f > 0$ is inadmissible,

b_{ij} is the tensor function of additional deformations, which is determined by an increase in $\Delta\varphi$ and the known results of the previous stage of tracing:

$$b_{ij} = \left[\frac{\sigma_{ij} - \delta_{ij}\sigma}{2G} + \delta_{ij}(K\sigma) \right]_{t-\Delta t} + \delta_{ij}\Delta\varphi \quad (16)$$

$(i, j = x, y, z).$

Flow conditions in the form (11) include significant physical nonlinearity in the function of the material state ψ . In order to realize this type of physical nonlinearity, iterative processes are usually used. As a result, at each iteration, a physically nonlinear problem passes into a linear type of problem of elasticity theory with a variable shear modulus, which is equal to $1/2\psi$ and additional deformations b_{ij} . To solve such a linearized problem, numerical methods are used.

DEVELOPMENT OF MATHEMATICAL MODEL OF RELAXATION AND REDISTRIBUTION OF RESIDUAL STRESSES IN CWJ DURING HEAT TREATMENT

Welded joints of critical structures are subjected to postweld heat treatment. According to the requirements of standard documentation [11], after welding composite welded joints of structural elements in NPP equipment are subjected to heat treatment applying a high tempering mode.

According to the item 13.18 [8] (for replacement [11]), producing welded joints of parts with steels of pearlite class or high-chromium steels with parts of austenite class steels by austenitic filler materials, are not subjected to heat treatment except for the cases, when it is specified by drawings and/or TPD. In addition, according to the item 13.14 [12], the temperature of tempering welded joints of parts of steels of different grades, for which a different tempering temperature is provided, is specified by TPD. Based on the abovementioned, heat treatment modes were set in accordance with the requirements [6].

In the mathematical modeling of the process of postweld heat treatment of CWJ (cover of RV), the

feature of the developed model for determining the nonstationary temperature field was a convective heat transfer on the surfaces due to a gradual heating of the environment (air) in the furnace, holding and a subsequent rather slow cooling in the furnace and then in air. Nonstationary boundary conditions corresponded to a uniform increase in the ambient temperature in the process of heating and to a decrease in temperature to 20 °C during cooling.

The diagram of heat treatment mode, namely, changes in the ambient temperature T_{out} in the process of high tempering of RV cover in the furnace during heating at a rate of 30 °C/h, holding during 9 h and cooling at a rate of 30 °C/h is shown in Figure 4.

Initial and boundary conditions of the boundary value problem of determining temperature distributions in CWJ during heat treatment in time t :

$$\begin{aligned} T_{out}(0) &= 20 \text{ }^\circ\text{C}, T(0) = 20 \text{ }^\circ\text{C}, \\ q &= -h(T_{out}(t) - T), T_{out}(t) = 30 \text{ }^\circ\text{C/h}\cdot t, \\ T_{out}^{\max} &= 650 \text{ }^\circ\text{C}. \end{aligned}$$

The heat transfer coefficient from the surfaces of CWJ elements during convective heat exchange with the environment in the furnace and in the air was taken equal to $h = 30 \text{ W/m}^2 \text{ }^\circ\text{C}$ in the conditions of a natural convection and constant heating and cooling throughout the whole temperature range. A radiant heat exchange in the developed model was not modelled separately, its contribution was taken into account in some increase in the value of the heat transfer coefficient.

A long-term process of heating welded structural elements to a holding temperature of 650 °C causes processes of a high-temperature creep in the material, which leads to relaxation of residual stresses in the area of welded joints.

In the developed model, the problem of determining SSS during heat treatment was solved in a visco-elastoplastic formulation [9]:

$$\varepsilon_{ij} = \varepsilon_{ij}^e + \varepsilon_{ij}^p + \varepsilon_{ij}^{cr} \quad (i, j = x, y, z), \quad (17)$$

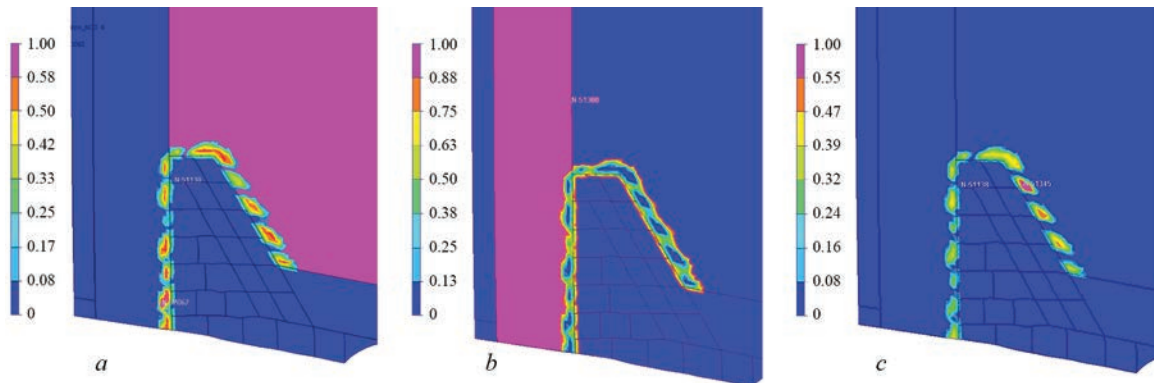


Figure 5. Results of modeling residual microstructural composition in the CWJ zone at $T_{preheating} = 100 \text{ }^\circ\text{C}$: *a* — bainite; *b* — ferrite-pearlite; *c* — martensite

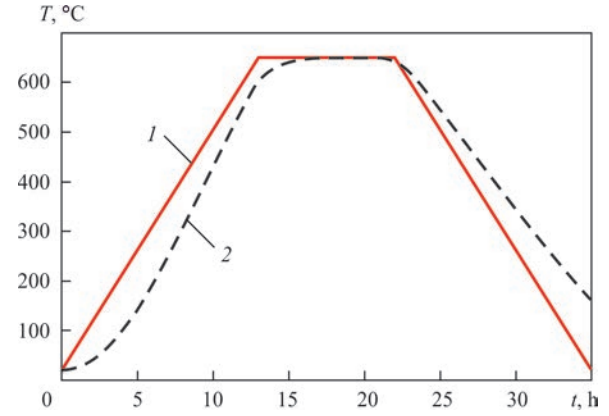


Figure 4. Diagram of changing temperature of CWJ material in the process of heat treatment using a high tempering mode at $T = 650 \text{ }^\circ\text{C}$: 1 — heat treatment mode; 2 — calculated temperature where the rate of creep deformations was determined by the Bailey–Norton's law [13]:

$$\dot{\varepsilon}_{eq}^{cr} = A \cdot \sigma_{eq}^n \quad (18)$$

For austenitic 08Kh18N10T steel at a temperature of 700 °C (973 K), while determining the rate of deformations of a temperature creep, the following coefficients can be accepted: $A = 6.948 \cdot 10^{-14} \text{ (MPa}^{-n} \cdot \text{h}^{-1})$ $n = 6.22$ [14].

RESULTS OF MATHEMATICAL MODELING OF TEMPERATURE DISTRIBUTIONS AND MICROSTRUCTURAL PHASE TRANSFORMATIONS

The results of modeling microstructural transformations in CWJ metal during welding ($T_{heating} = 100 \text{ }^\circ\text{C}$) and a subsequent cooling showed (Figure 5) the presence of local formation of hardened structures in HAZ of the nozzle metal (steel 20) and in the base material of the cover (steel 15Kh2NMF). Figure 6 presents diagrams of changes in the microstructural phase state at the characteristic point of HAZ of the base material of the cover, where the maximum residual martensite content was obtained, depending on heating temperature. The use of preheating during CWJ welding at the level $T_{heating} = 200 \text{ }^\circ\text{C}$ allows reducing the relative con-

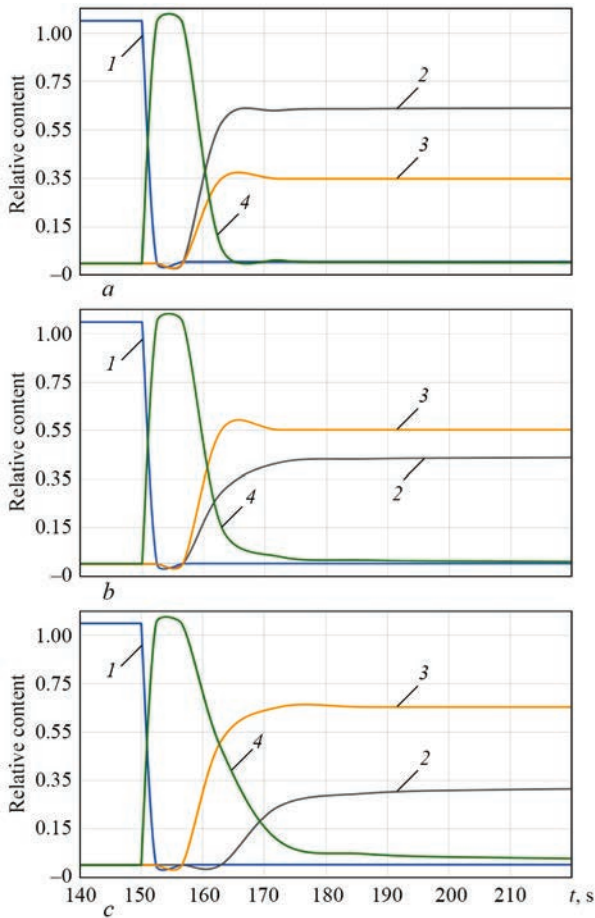


Figure 6. Kinetics of microstructural phase transformations at the characteristic point of HAZ of the base material of the cover (15Kh2NMFA steel) for different preheating temperatures: *a* — without preheating; *b* — $T_{\text{preheating}} = 100\text{ }^{\circ}\text{C}$; *c* — $T_{\text{preheating}} = 200\text{ }^{\circ}\text{C}$; 1 — ferrite; 2 — martensite; 3 — bainite; 4 — austenite

tent of martensite in HAZ from 65 to 30 % as compared to welding without preheating.

RESULTS OF MATHEMATICAL MODELING OF RESIDUAL STRESSES AFTER WELDING AND AFTER HEAT TREATMENT

Figure 7 presents the distribution of residual stresses after welding CWJ at the temperature of preliminary and accompanying heating $T_{\text{heating}} = 100\text{ }^{\circ}\text{C}$ and a subsequent cooling to $T = 20\text{ }^{\circ}\text{C}$. The radial (relative to the nozzle axis) component in the area of the welded joint (Figure 7, *a*) is characterized mainly by tensile residual stresses of up to 200 MPa and local areas of maximum tensile stresses of up to 400 MPa in the base material of the cover adjacent to the austenitic weld metal and in the material of the nozzle, in the upper part, adjacent to the weld metal. The axial (in the direction of the nozzle axis) residual stresses (Figure 7, *b*) have a low level in the austenitic material of the deposit and the weld, and in the base material of the cover and the nozzle, the zones of compressive and tensile stresses of up to 400 MPa were formed. The highest tensile stresses (up to 700 MPa) were determined for the circular component of residual stresses (Figure 7, *c*) in the area of the base material of the cover, which is adjacent to the austenitic weld metal.

Thus, after welding CWJ, rather high residual tensile stresses were obtained, which can negatively affect the strength of the reactor cover during further operation. Therefore, the use of technological operation of postweld heat treatment is absolutely justified. After modeling of welding, modeling of a general

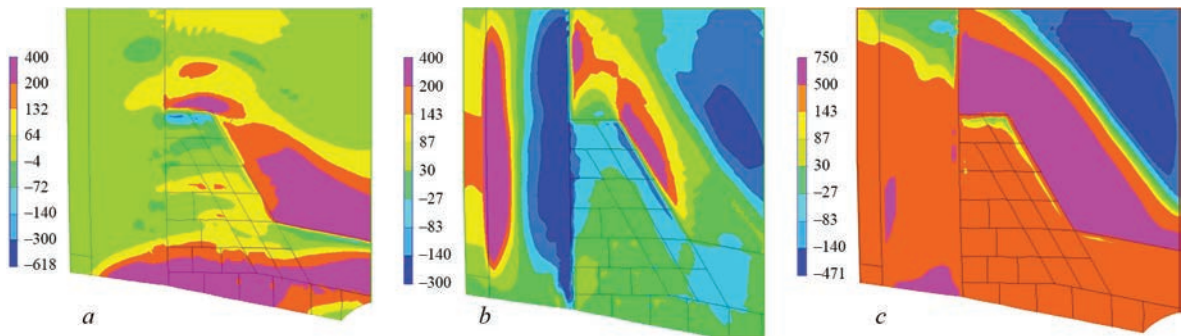


Figure 7. Residual stresses in CWJ after welding at $T_{\text{heating}} = 100\text{ }^{\circ}\text{C}$: *a* — radial; *b* — axial; *c* — circular

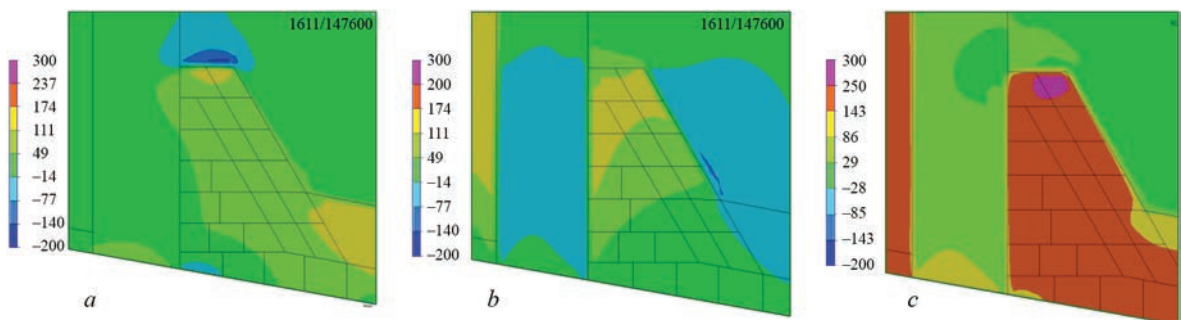


Figure 8. Residual stresses in CWJ after welding ($T_{\text{heating}} = 100\text{ }^{\circ}\text{C}$) and heat treatment ($T = 650\text{ }^{\circ}\text{C}$, $t_{\text{holding}} = 15\text{ h}$): *a* — radial; *b* — axial; *c* — circular

heat treatment was performed according to the mode of high tempering at a temperature of 650 °C with a holding time of 15 h (see Figure 4). The results of the calculation are shown in Figure 8.

ANALYSIS OF EFFECT OF HEATING TEMPERATURE AND HEAT TREATMENT MODE ON RESIDUAL STRESSES

In order to determine the effect of heating temperature during welding and heat treatment mode on residual stresses of a composite (dissimilar) welded joint of the WWR-1000 reactor vessel cover in representative cross-sections (Figure 9), the diagrams of stress distribution were constructed over the thickness of the welded joint (Figures 10–12).

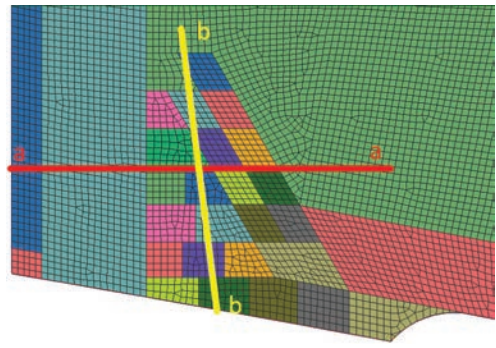


Figure 9. Cross-sections for determination of stresses

The effect of heating temperature during welding on distribution of residual stresses is insignificant, in the selected cross-section of the welded joint over the

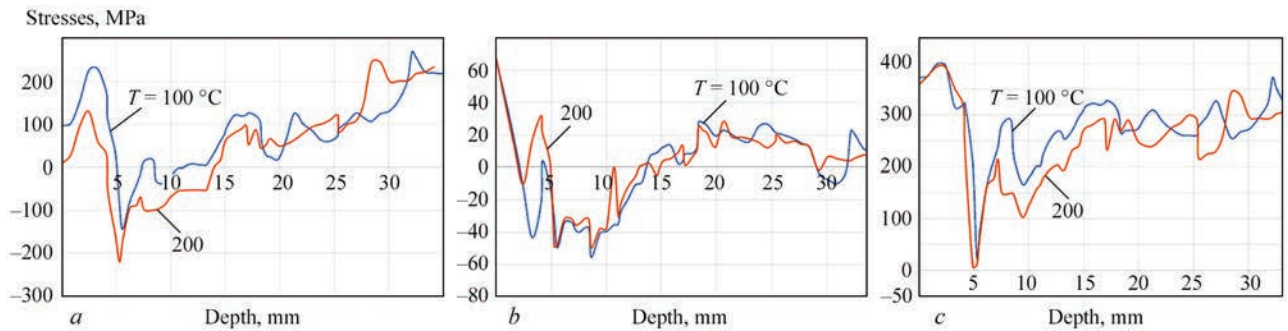


Figure 10. Effect of heating temperature during welding on distribution of residual stresses over the depth of the weld (cross-section *b–b* Figure 9): *a* — radial; *b* — axial; *c* — circular

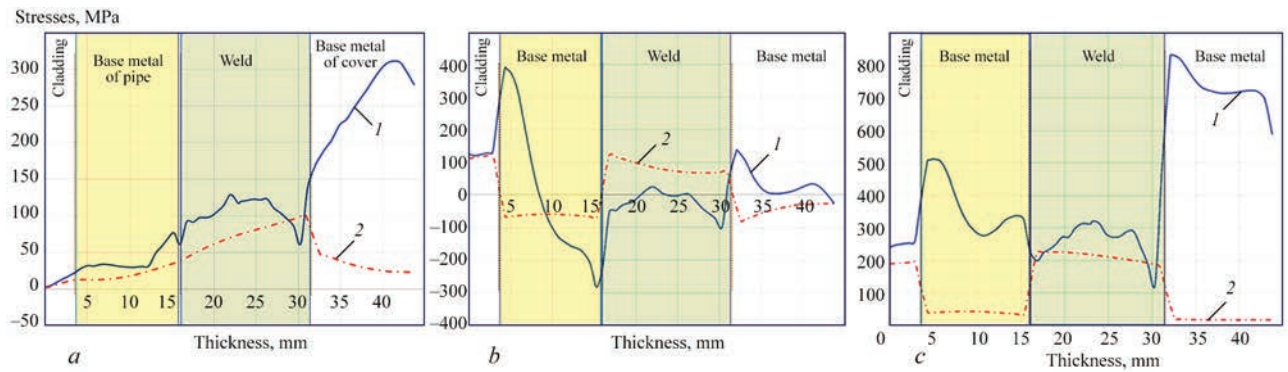


Figure 11. Effect of heat treatment ($T = 650\text{ }^{\circ}\text{C}$) on distribution of residual stresses across the width of the weld (cross-section *a–a* Figure 9): *a* — radial; *b* — axial; *c* — circular; 1 — before heat treatment; 2 — after heat treatment

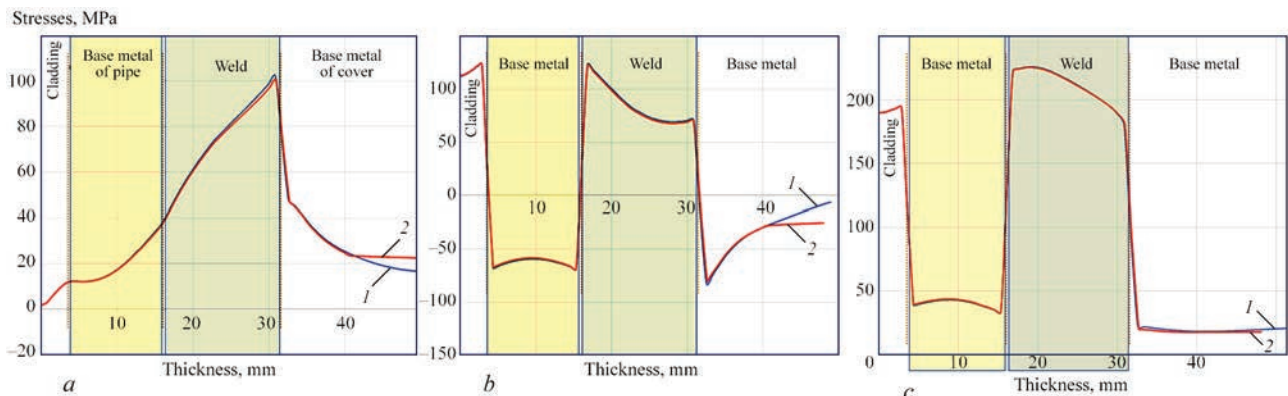


Figure 12. Effect of holding time during heat treatment ($T = 650\text{ }^{\circ}\text{C}$) on distribution of residual stresses across the width of the weld (cross-section *a–a* Figure 9): *a* — radial; *b* — axial; *c* — circular; 1 — 15 h; 2 — 9

depth of the weld (Figure 10), maximum residual tensile stresses in the radial direction noticeably decrease (from 220 to 120 MPa) with an increase in heating temperature, other components (in axial and circular directions) are almost unchanged.

The effect of heat treatment ($T = 650\text{ }^{\circ}\text{C}$) on distribution of residual stresses is quite significant. Radial stresses are noticeably reduced, especially in the area of the base material of the cover, from 300 to 30 MPa (Figure 11, *a*). The axial component of residual stresses in the area of the pipe and cover material decreases, and in the austenitic weld material it increases to 100 MPa (Figure 11, *b*), which is associated with the difference in the coefficients of thermal expansion of different CWJ materials.

The effect of holding time ($t_{\text{holding}} = 15\text{ h}$) during heat treatment ($T = 650\text{ }^{\circ}\text{C}$) on distribution of residual stresses is also insignificant (Figure 12). Relaxation of residual welding stresses largely occurs during the first hour of holding at the maximum temperature, and distribution of residual stresses after heat treatment is determined mainly by the difference in thermophysical properties of different joining materials.

CONCLUSIONS

1. Analysis of the results of mathematical modeling of SSS in the composite welded joint of the WWER-1000 reactor vessel cover with the CSS nozzle showed that the distribution of residual stresses after welding has a complex nature with high tensile stresses in the zones of ferritic-pearlitic materials, inherent in joints of dissimilar materials (base material of the cover of 15Kh2NMFA steel and the nozzle of steel 20).

2. It was determined that in welding CWJ without heating, the residual content of hardened structures in the HAZ metal of the nozzle (steel 20) and in the base material of the cover (steel 15Kh2NMF) can reach 65 %. The use of preliminary (accompanying) heating can significantly reduce the relative content of martensite in the base material of the cover and the nozzle at the boundary interface of fusion with the austenitic weld material.

3. Postweld heat treatment at a high tempering mode ($T = 650\text{ }^{\circ}\text{C}$) reduces the level of residual stresses, but due to a significant difference in the coefficients of thermal expansion of dissimilar joining materials, new rather high residual tensile stresses are formed in the areas of austenitic deposited materials.

REFERENCES

- Makhnenko, O.V., Saprykina, G.Yu. (2002) Role of mathematical modeling in solving problems of welding dissimilar steels (Review). *The Paton Welding J.*, **3**, 14–25.
- Makhnenko, O.V., Kozlitina, S.S., Dzyubak, L.L., Kravets, V.P. (2010) Risk of formation of carbides and α -phase in welding of high-alloy chrome-nickel steels. *The Paton Welding J.*, **12**, 5–8.
- Wenchun Jiang, Wanchuck Woo, Yun Luo, J.H. Li. (2017) Residual stress distribution in a dissimilar weld joint by experimental and simulation study. *J. of Pressure Vessel Technology*, **139**(2), 011402.
- Dean, D., Ogawa, K., Kiyoshima, S. et al. (2009) Simplified methodology to compute the residual stresses in a dissimilar metal welded pipe with considering cladding, buttering and post weld heat treatment. *Computat. Mater. Sci.*, **47**, 398–408.
- Kasatkin, O.G., Tsaryuk, A.K., Skulsky, V.Yu. et al. (2007) Method for improving local damage resistance of welded joints in NPP pipelines. *The Paton Welding J.*, **3**, 27–30.
- 1160.02.02.000 PS: Certificate of vessel. Upper block YC00B01. 2.1 [in Russian].
- 1160.02.18.000TB1: Cover. Table of quality control [in Russian].
- 1160.02.18.000TB2: Cover. Table of quality control [in Russian].
- Makhnenko, V.I. (1976) *Calculated methods of investigation of welding stresses and strains*. Kyiv, Naukova Dumka [in Russian].
- Yurjev, S.F. (1950) *Specific volumes of phase in martensitic transformation of austenite*. Moscow, Metallurgizdat [in Russian].
- (1989) PNAE G-7-009–89: *Equipment and pipings of nuclear power plants. Welding and surfacing. Fundamentals*. Moscow, Energoatomizdat [in Russian].
- SOU NAEK 159: *Assurance of technical safety. Welding and surfacing of equipment and pipings of nuclear power plants with WWER reactors*. Technical requirements.
- Rabotnov, Yu.N. (1966) *Creep of structural elements*. Moscow, GIFML [in Russian].
- Margolin, B. Z., Gulenko, A. G., Kursevich, I. P., Buchatskii, A.A. (2006) Modeling for fracture in materials under long-term static creep loading and neutron irradiation. Pt 2. Prediction of creep rupture strength for austenitic materials. *Strength of Materials*, **38**(5), 449–457.

ORCID

O.V. Makhnenko: 0000-0002-8583-0163

CONFLICT OF INTEREST

The Authors declare no conflict of interest

CORRESPONDING AUTHOR

O.V. Makhnenko: 0000-0002-8583-0163

E.O. Paton Electric Welding Institute of the NASU
11 Kazymyr Malevych Str., 03150, Kyiv, Ukraine

E-mail: E-mail: makhnenko@paton.kiev.ua

SUGGESTED CITATION

A.A. Makarenko, O.V. Makhnenko (2022) Mathematical modeling of residual stresses in composite welded joints of WWER-1000 reactor vessel cover with CSS nozzles. *The Paton Welding J.*, **1**, 33–40.

JOURNAL HOME PAGE

<https://pwj.com.ua/en>

Received: 30.10.2021
Accepted: 07.02.2022

<https://doi.org/10.37434/tpwj2022.01.08>

INFLUENCE OF LONG-TERM SOAKING ON THE STRUCTURE AND PROPERTIES OF IN625 ALLOY SAMPLES MADE BY SELECTIVE LASER MELTING

N.O. Lysenko, O.O. Pedash, V.V. Klochykhin, P.O. Kasai

JSC “MOTOR SICH”, 69068, Zaporizhzhya, Ukraine

ABSTRACT

The paper presents the results of studying the influence of long-term soaking on the structure and properties of samples made by selective laser melting of Inconel 625 alloy powders, produced by the method of off-center plasma spraying of a rapidly rotating rod billet (PREP-process). Investigations of chemical composition, macro- and microstructure, mechanical and heat-resistant properties of the samples plotted in xy and z direction was performed. Samples after building and hot isostatic pressing with subsequent heat treatment by different variants were to be examined. Investigation results showed that performance of the operation of hot isostatic pressing of the samples with subsequent standard heat treatment promotes practically complete elimination of microporosity in inner volumes of the metal and obtaining a more uniform solid solution. It was established that long-term soaking at the temperature of 900 °C, facilitates lowering of ductile and heat-resistant properties of Inconel 625 alloy due to lamellar precipitates of δ -phase. Performed study was the basis for recommending the recovery heat treatment mode. In addition, it is shown that long-term soaking at the temperatures of 700 and 980 °C does not lead to precipitation of lamellar δ -phase.

KEY WORDS: heat-resistant alloy; additive technologies; selective laser melting; hot isostatic pressing; heat treatment

INTRODUCTION

Development of additive technologies, in particular those of selective laser melting (SLM), allows manufacturing metal products of a complex geometrical shape by 3D compacting directly from a computer model by layer-by-layer deposition of metal powder and its further melting. Additive technology is the general name of a group of technologies, which envisage manufacturing products by digital models by layer-by-layer addition of material [1–4]. The interest to additive technologies and direct “printing” or growing of metal parts, as an alternative to traditional technologies, arose first of all in aviation, space industry, medicine and power engineering. Here, economic activity was the main driving factor. This is particularly true for single complex products, moulds with intricate cooling channels, where manufacturing by the traditional methods is considerably more expensive, than using additive technologies [1]. In addition to lower cost of manufacturing unique products, additive technologies allow an essential reduction of the time, consumed in manufacturing the finished product. There is no need to make sophisticated fixtures. Proceeding from that, the time from the moment of creating the model to obtaining the finished part is reduced from several weeks to several days.

In this work, the influence of long-term soaking at different temperatures on the structure and proper-

ties of Inconel alloy (IN625) was studied on samples made by 3D printing (selective laser melting).

MATERIALS AND METHODS OF INVESTIGATION

Used as the object of study were samples from Inconel 625 alloy for testing mechanical properties and microstructure, produced by selective laser melting in 3D unit of EOS GmbH Company (Germany), with working chamber dimensions ($x \times y \times z$) of 400×400×400 mm, fitted with ytterbium laser of 1000 W power.

The powder was made by the method of off-center spraying of rapidly rotating billet (PREP-process). The fractions of granules used for making the samples were equal to 20–50 μm .

Laser sintering of powders is a multiple repetitive process which includes several stages: deposition of a powder layer and its leveling with a roller; laser processing (scanning) of the powder layer with full penetration of the powder mixture according to the geometry of the initial 3D model; cleaning of the produced layer; moving the platform with the part downwards by one layer thickness; repetition of the entire process, i.e. deposition of the next powder layer, laser scanning, etc. Processing is performed in the chamber with inert gas purging and is controlled by the computer to obtain the specified 3D geometry of the part.

The made samples were both cylindrical of 14 mm diameter, and of rectangular cross-section with

Table 1. Modes of heat-treatment of 3D samples after HIP

Variant	Homogenizing I		Aging		Homogenizing II	
	$T, ^\circ\text{C}$	τ, h	$T, ^\circ\text{C}$	τ, h	$T, ^\circ\text{C}$	τ, h
1	1190	1	–	–	–	–
2	Same	Same	900	16	–	–
3	–»–	–»–	Same	700	–	–
4	–»–	–»–	–»–	1000	–	–
5	–»–	–»–	–»–	2100	–	–
6	–»–	–»–	–»–	Same	1000	1
7a	–»–	–»–	–»–	1000	1180	Same
7b	–»–	–»–	–»–	2100	Same	–»–
8	–»–	–»–	700	700	–	–
9	–»–	–»–	980	1400	–	–

16×6 mm dimensions. Sample length was 65 mm. Sample building on 3D printer was performed in *xy*, as well as in *z* direction. To eliminate internal porosity and improve the sample density, the process of selective laser melting was followed by hot isostatic pressing (HIP) in hot isostatic press QIH 09×1.5-2070-1400 MURC (QUINTUS Company, Sweden). HIP was conducted in the following mode: heating up to 1160±10 °C temperature, soaking time of 3 h, 160 MPa working gas pressure in the high-pressure vessel. Sample cooling was performed with application of the function of high-rate uniform cooling.

After HIP samples were heat-treated in vacuum furnace IPSEN T²T in the dynamic vacuum environment, cooling was conducted in the flow of inert gas (argon).

Modes of sample heat treatment after gas stating are given in Table 1.

After treatment by different variants the billets were machined to ensure the dimensions, envisaged by the technical documentation for making samples for mechanical and high-temperature strength testing.

The alloy chemical composition was determined by the methods of spectral and chemical analysis. Mechanical properties (σ_r , $\sigma_{0.2}$, δ , ψ) of the samples were

tested in tensile testing machine ZDMY 30 for correspondence to the requirements of AMS 7000 standard.

Impact toughness (*KCU*) was determined on impact samples, tested in pendulum testing machine Instron SI-1M.

Hardness was determined by Brinell method in LECO AMH-43 instrument.

The time to high-temperature destruction (τ_d) (characteristic which is determined at long-term strength testing) of the samples was found in Instron M3 unit at the temperature of 700 °C and constant loading of 333 MPa. At long-term strength testing the samples were taken to destruction.

Fractographic study of powder morphology, as well as fractures of rupture and impact samples after testing for mechanical properties was conducted in binocular microscope STEMI 2000-C and electron scanning microscope JEOL JSM 6360LA.

Microstructural studies were performed on un-etched and etched microsections using Axio Observer. Dlm microscope.

ANALYSIS AND DISCUSSION OF THE OBTAINED RESULTS

Microstructural examination revealed that the powder used to obtain samples by 3D laser printing (SLP), is characterized by a practically complete absence of satellite granules, and good sphericity with a small number of irregularly shaped particles (Figure 1).

Chemical composition of the made samples is satisfactory and meets the requirements of AMS 7000 for the studied alloy (Table 2).

IN625 alloy is a typical example of alloys with a low hardening (or non-hardenable alloys). The alloy is mainly used at up to 1000 °C temperatures, where oxidation resistance is the most important requirement [5]. More over, at temperatures above 550 °C, this alloy can undergo essential changes of the microstructure and mechanical properties [6].

It is found that mechanical properties of the samples grown in *xy* and *z* directions (variants 1, 2), meet

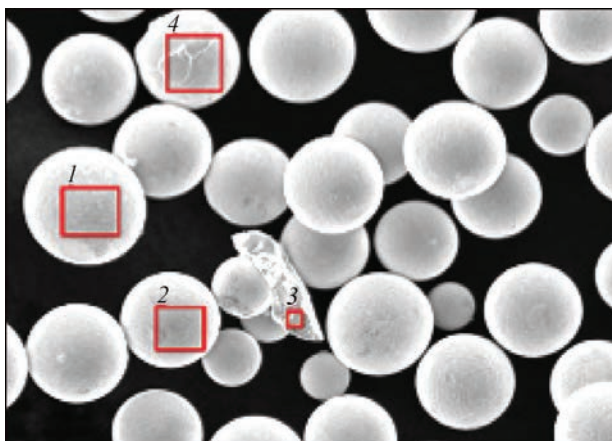


Figure 1. Morphology of IN625 alloy powders

Table 2. Chemical composition of Inconel 625 samples, wt.%

Alloy grade	Element content, %						
	C	Cr	Al	Ti	Nb	Mo	Fe
IN625	0.03	21.20	0.20	0.20	3.88	8.55	3.03
AMS 7000 norms	≤0.10	20.0–23.0	≤0.4	≤0.4	3.15–4.15	8.0–10.0	≤5.00

Note. The balance is Ni.

Table 3. Mechanical properties of IN625 alloy at $T = 20\text{ }^{\circ}\text{C}$

Heat-treatment variant	Direction of sample building	σ_r , MPa	$\sigma_{0.2}$, MPa	δ , %	ψ , %	KCU, J/cm ²	HB
1	xy	882	438.5	56.4	57.7	281.3	201
	z	869	433.5	57.0	59.0	308.7	207
2	xy	881	448.0	48.4	53.9	281.3	Same
	z	866	433.0	52.0	53.7	308.7	→—
AMS 7000 norms		≥827	≥344.7	≥30.0	—	—	—

the requirements of AMS 7000 for IN625 alloy. Values of relative elongation (δ) are approximately 2 times higher than the requirements of AMS 7000 (Table 3).

Long-term strength ($T_{\text{test}} = 700\text{ }^{\circ}\text{C}$; $\sigma = 333\text{ MPa}$) of the samples after heat treatment by the 1st and 2nd variant (see Table 1) is at approximately the same level (Table 4); here the time to fracture (τ_{fr}) is equal to 437.5–655.4 h; in keeping with AMS 7000 τ_{fr} is not regulated.

It should be noted that performance of aging at the temperature of $900 \pm 10\text{ }^{\circ}\text{C}$ for 16 h (variant 2) did not lead to any noticeable increase of the mechanical or high-temperature properties.

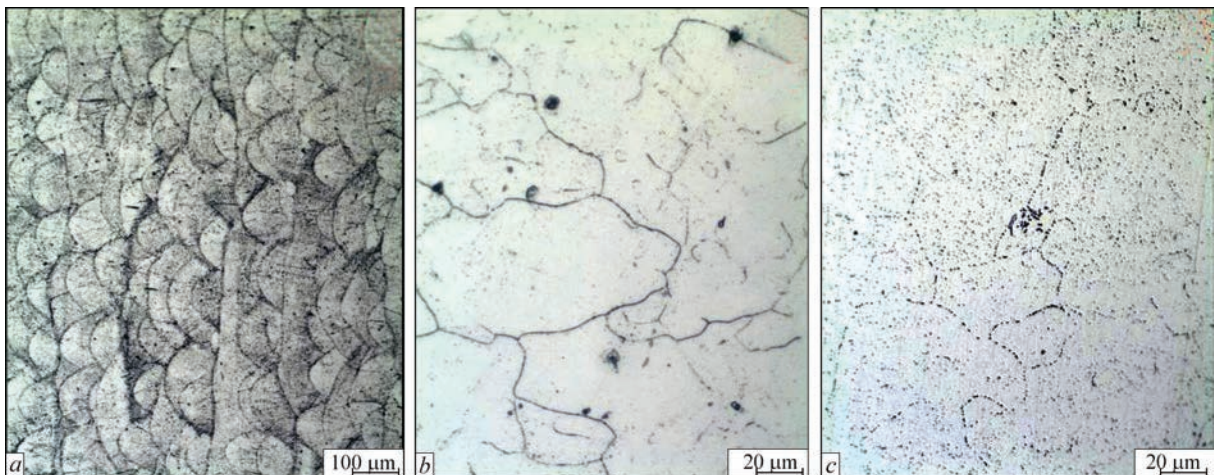
Metallographic examination showed that the sample microstructure in the condition after building (before performance of HIP and heat treatment operations of both vertical (z), and horizontal (xy) ones) is γ -solid solution of Ni–Cr–Mo–Nb–Fe with the presence of carbides and carbonitrides, and it corresponds to non-heat-treated state of IN625 alloy, manufactured by the method of 3D printing (Figure 2, *a*). A structural in-

Table 4. High-temperature strength properties of IN625 alloy

Heat-treatment variant	Direction of sample building	Long-term strength		
		T_{test} , $^{\circ}\text{C}$	σ , MPa	Time-to-fracture (τ_{fr}), h
1	xy	700	333	446 ¹⁵
	z	Same	Same	627 ²⁰
2	xy	→—	→—	517 ⁵⁰
	z	→—	→—	590 ³⁰

homogeneity is observed in the initial samples, which is due to formation of zones of layer-by-layer fusion, as well as thin dendrites elongated in the direction of sample growing, which formed due to high rates of heating and cooling, which are in place during the processes of melting and solidification in a short time.

During high-temperature heating at HIP ($1160 \pm 10\text{ }^{\circ}\text{C}$) and heat-treatment ($1190 \pm 10\text{ }^{\circ}\text{C}$), a more uniform structure forms due to solid solution homogenizing as a result of equalizing of the chemi-


Figure 2. Microstructure of 3D samples from IN625 alloy: *a* — initial condition, $\times 100$; *b* — variant 1, $\times 500$; *c* — variant 2, $\times 500$ (see Table 1)

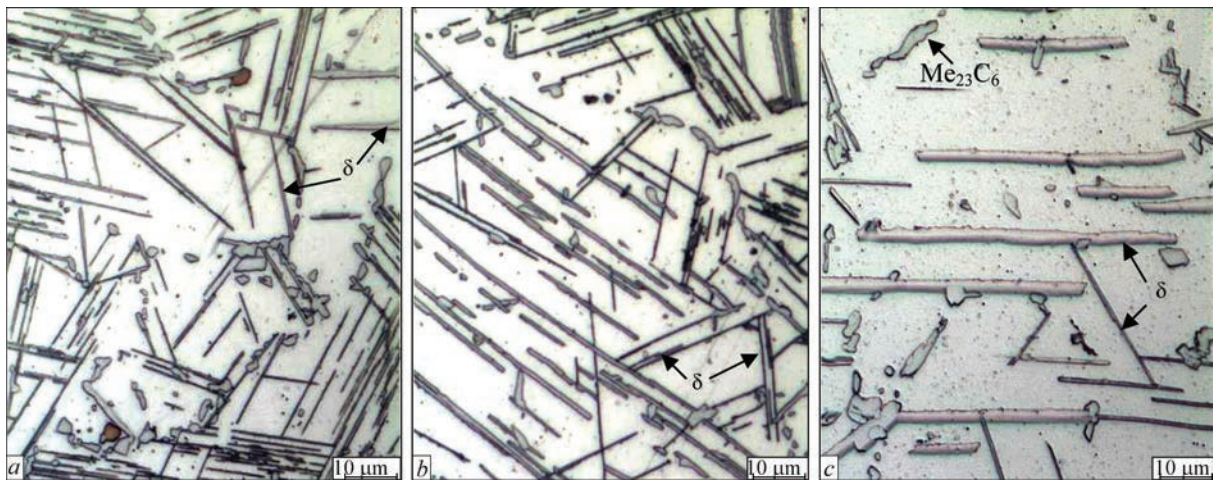


Figure 3. Microstructure of 3D samples of IN625 alloy after heat-treatment, $\times 1000$: *a* — variant 3; *b* — variant 4; *c* — variant 5 (see Table 1)

cal composition between layer-by-layer fusion zones (Figure 2, *b*).

At heat-treatment by variant 2 (HIP + (homogenizing + aging at 900 °C, 16 h)) precipitation of hardening intermetallic γ'' (Ni_3Nb)-phase with BCC structure and slight coagulation of carbides of M_{23}C_6 type (Figure 2, *c*) are observed (Figure 2, *c*).

Lamellar precipitates of δ -phase, as well as structures, characteristic for overheated state of IN625 alloy in the form of partial melting along the grain boundaries, were not revealed in the initial samples heat-treated by the 1st and 2nd variants.

Performance of HIP operation by the above-given mode promotes practically complete “healing” of pores and microdiscontinuities, concentrated in the inner volumes of metal. Here, globular and (or) thin film oxides were found in the “healing” zones. Dimensions of oxide inclusions in the studied sample material were, mainly, equal to 7 μm (isolated, rarely found ones were up to $\sim 20 \mu\text{m}$). Carbides and carbonitrides precipitate in the form of discrete globular particles of approximately 5 μm size.

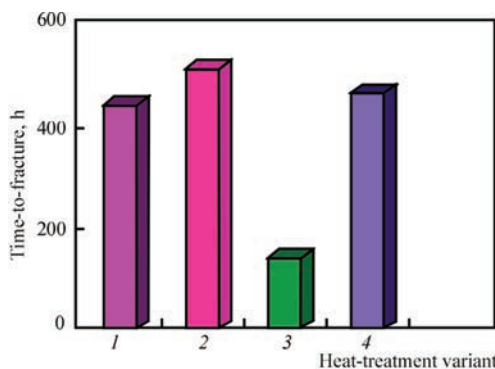


Figure 4. Long-term strength of 3D samples of IN625 alloy, depending on heat-treatment variant: 1 — variant 1; 2 — variant 2; 3 — variant 4; 4 — variant 7a (see Table 1)

Conducting long-term soaking at the temperature of 900 °C (variants 3, 4, 5) promoted precipitation of a considerable amount of lamellar particles of δ -phase from γ -matrix (Figure 3). With longer soaking time the number and dimensions of δ -phase plates increased: at soaking for 700 h (variant 3) the plate width reached approximately 0.85 μm (Figure 3, *a*); at soaking for 1000 h (variant 4) plates of the width of approximately up to 1.5 μm (Figure 3, *b*) were found; at soaking for 2100 h (variant 5) the maximum width of the plates is equal to approximately 3.75 μm (Figure 3, *c*).

It should be also noted that the material of the samples processed by variants 3–5, demonstrates coarsening of the structure as a result of growth and coagulation of carbides of Cr_{23}C_6 type, particularly, on grain boundaries. Precipitation of particles of hardening intermetallic γ -phase is negligible.

Testing samples treated by the 4th variant showed that long-term soaking (1000 h) at the temperature of 900 °C leads to lowering of the ductile characteristics (δ , ψ — 1.5 times, KCU — ~ 6 times) at a certain increase of strength (σ , $\sigma_{0.2}$) and hardness (HB) of the material, compared with the values, obtained after heat-treatment by variants 1 and 2 (Table 5).

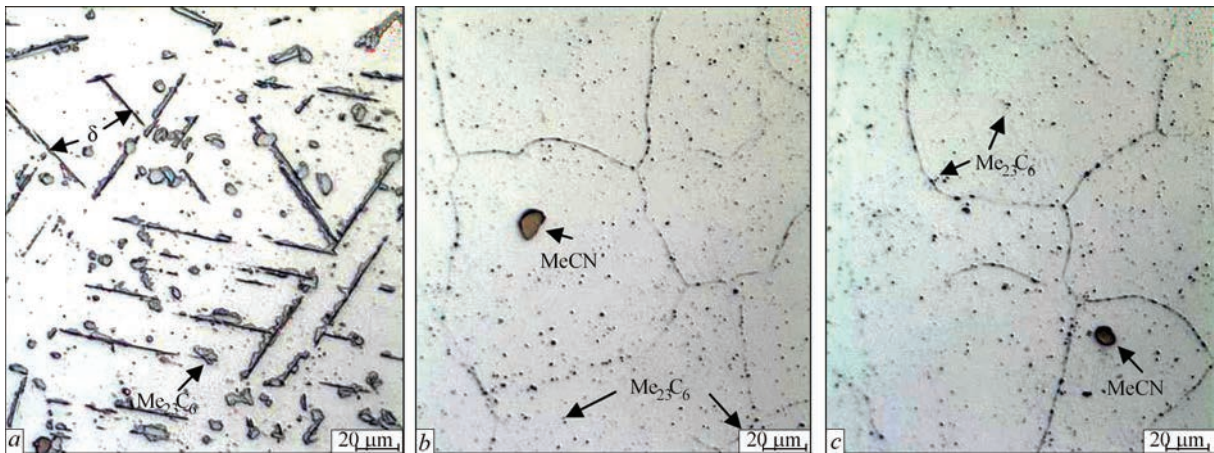
Long-term strength of samples heat-treated by variant 4 (with soaking for 1000 h at aging at 900 °C), decreased more than 3 times (Figure 4).

In order to increase the ductility and high-temperature strength of IN625 alloy, and eliminate unfavourable phases (lamellar and large near-boundary carbides) formed during long-term soaking at 900 °C temperature, recovery heat treatment operations were performed at temperatures of 1000 °C (variant 6) and 1180 °C (variants 7a, 7b) with soaking for 1 h.

Fragmentation and thinning of δ -phase plates, as well as partial dissolution of δ -phase and Cr_{23}C_6 car-

Table 5. Mechanical properties of IN625 alloy at $T = 20\text{ }^{\circ}\text{C}$

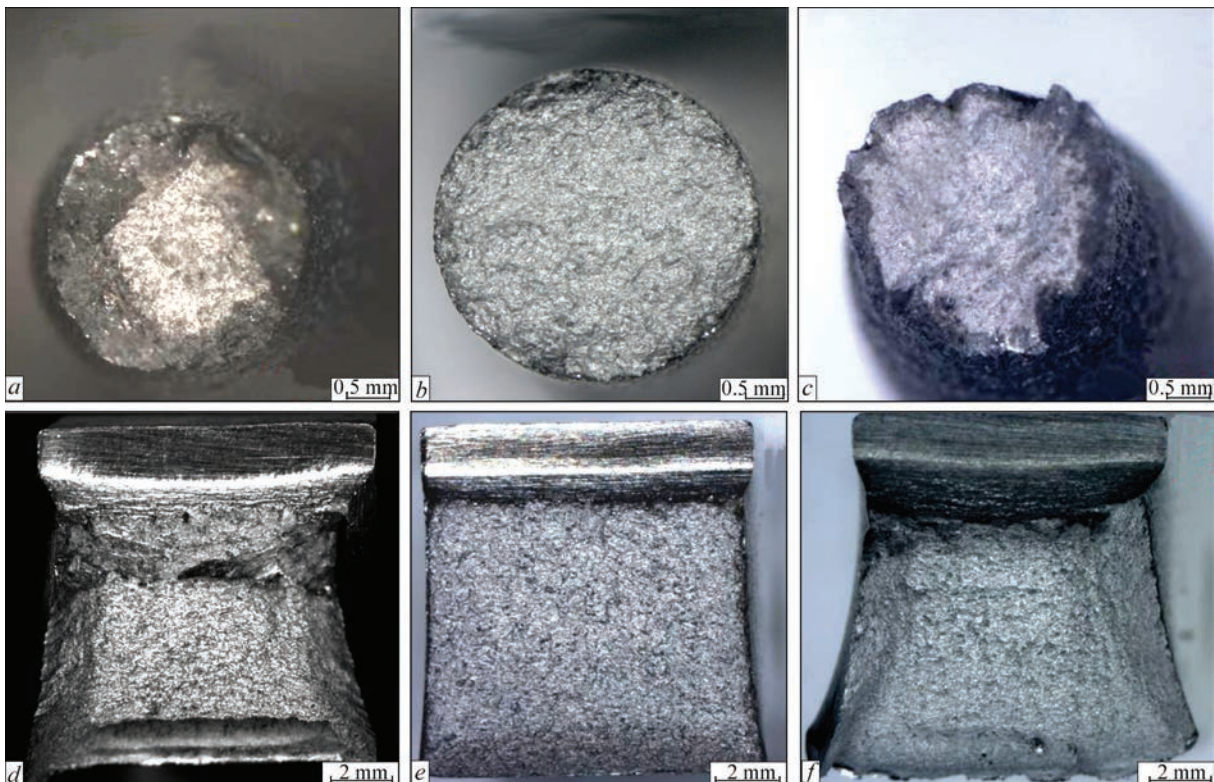
Heat-treatment variant	Direction of sample building	σ_r , MPa	$\sigma_{0.2}$, MPa	δ , %	ψ , %	KCU, J/cm ²	HB
1	xy	882.0	438.5	56.4	57.7	281.3	201
4	→→	912.0	467.0	38.0	33.4	49.0	241
7a	→→	885.0	456.7	60.0	64.2	262.2	207
AMS 7000 norms		≥ 827.0	≥ 344.7	≥ 30.0	–	–	–


Figure 5. Microstructure of 3D samples of IN625 alloy after recovery heat-treatment, $\times 1000$: *a* — variant 6 (variant 4 + heating at $1000\text{ }^{\circ}\text{C}$ (1 h)); *b* — variant 7a (variant 4 + heating at $1180\text{ }^{\circ}\text{C}$ (1 h)); *c* — variant 7b (variant 5 + heating at $1180\text{ }^{\circ}\text{C}$ (1 h))

bides in γ -solid solution are observed in the microstructure of IN625 alloy samples, heat treated by variant 6 at $1000\text{ }^{\circ}\text{C}$ temperature (1 h) (Figure 5).

Heat-treatment of samples by variants 7a, 7b at $1180\text{ }^{\circ}\text{C}$ temperature (1 h) (after long-term soaking for 1000 h (variant 4) and 2100 h (variant 5)) pro-

notes complete dissolution of lamellar δ -phase and Cr_{23}C_6 type carbides with further precipitation of these carbides in the form of fine discrete particles (Figure 5). The microstructure is Ni–Cr–Mo–Nb–Fe γ -solid solution, containing carbides, carbonitrides and a small quantity of intermetallic γ'' -phase; it cor-


Figure 6. Fractographic structure of fractures of rupture (*a, b, c* — $\times 12.5$) and impact (*d, e, f* — $\times 6.5$) 3D samples of IN625 alloy: *a, d* — variant 1; *b, e* — variant 4; *c, f* — variant 7a

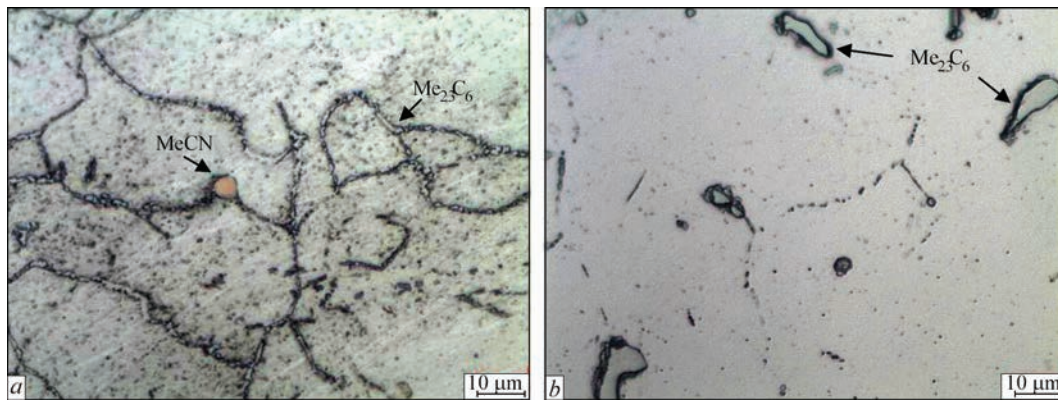


Figure 7. Microstructure of 3D samples of IN625 alloy after heat-treatment, $\times 1000$: *a* — variant 8; *b* — variant 9 (see Table 1)

responds to homogenized state of IN625 alloy, and is similar to variant 1.

Figure 6 shows the structure of fractures of IN625 alloy samples (3D printing), heat-treated by variants 1, 4 and 7a, after tensile and impact toughness testing at room temperature. The cup-shaped structure of the fractures and formation of a “neck” in the destruction zone on rupture test samples and presence of beveling on impact test samples of variants 1 and 7a are indicative of a rather high ductility of the alloy (Figure 6, *a, c, d, f*). Practical absence of the “neck” in the destruction zone on rupture samples or beveling on impact samples treated by the 4th variant, is characteristic for material of a lower ductility (Figure 6, *b, e*).

As a result of the performed study, it was determined that heat treatment at 1180 °C temperature for 2 h (variants 7a and 7b) promotes recovery of mechanical and high-temperature strength properties that is due to homogenizing of IN625 alloy, at which dissolution of lamellar δ -phase and Cr_{23}C_6 type carbides in γ -solid solution is observed, with further precipitation of Cr_{23}C_6 type carbides and a small quantity of intermetallic γ'' -phase in the form of fine discrete particles, strengthening the matrix.

In addition, the microstructural state of IN625 alloy samples produced by selective laser melting (3D printing) was studied after heat-treatment by variants 8 and 9 with long-term soaking at temperatures of 700 °C (700 h) and 980 °C (1400 h), respectively.

Metallographic examination of samples at up to $\times 1000$ magnification showed that long-term soaking at temperatures of 700 °C (700 h, variant 8) and 980 °C (1400 h, variant 9) does not lead to formation of lamellar δ -phase. Here, it was noted that at treatment by 8th variant (700 °C, 700 h) coarsening of the structure takes place, mainly, due to growing and coagulation of Cr_{23}C_6 type carbides which precipitate predominantly on grain boundaries (Figure 7, *a*).

In samples treated by the 9th variant (980 °C, 1400 h) the grain boundaries are thin, and a considerable quantity of Cr_{23}C_6 type carbides are present

in the form of coagulated particles of approximately 7–15 μm size, uniformly distributed in the metal volume (Figure 7, *b*).

CONCLUSIONS

1. Chemical composition of samples, made from IN625 alloy by 3D printing in EOS M400 unit, corresponds to AMS 7000 requirements for IN625 alloy.

2. It is found that long-term soaking at 900 °C temperature for 700 h (variant 3), 1000 h (variant 4) and 2100 h (variant 5) leads to lowering of ductility and high-temperature strength of IN625 alloy as a result of precipitation of a considerable number of lamellar particles of δ -phase from γ -matrix, as well as coarsening of the structure due to growth and coagulation of Cr_{23}C_6 type carbides, particularly on grain boundaries. Increase of soaking time promotes increase of the number and dimensions of δ -phase plates, as well as coarsening of the grain boundaries.

3. Heat treatment of samples with lower properties, presence of a large number of δ -phase plates and coarsening of the grain boundaries (variants 4, 5) at 1180 °C temperature for 1 h (variants 7a and 7b) promotes recovery of mechanical and high-temperature properties that is due to homogenizing of IN625 alloy, at which dissolution of lamellar δ -phase and Cr_{23}C_6 type carbides in γ -solid solution are observed with further precipitation of Cr_{23}C_6 type carbides and a small quantity of intermetallic γ'' -phase in the form of fine discrete particles which strengthen the matrix.

4. Long-term soaking at temperatures of 700 °C (700 h, variant 8) and 980 °C (1400 h, variant 9) does not lead to lamellar phase formation.

REFERENCES

1. Zlenko, M.A., Popovich, A.A., Mutylyna, I.N. (2013) *Additive technologies in mechanical engineering*. St.-Petersburg, SPbPU [in Russian].
2. Santos, E.C. (2006) Rapid manufacturing of metal components by laser forming. *Int. J. Mach. Tools Manuf.*, 46(12–13), 1459–1468.

3. Allen, J. (2011) The potential for aero engine component manufacture using additive layer manufacturing. *AERODAYS Conf., Madrid*.
4. (2013) *National Institute of Standards and Technology. Measurement science roadmap for metal-based additive manufacturing*. Energetics Incorp., Columbia, Maryland, for NIST, U.S. Department of Commerce, May, 2013.
5. Sims, Ch., Hagel, V. (1976) *Heat-resistant alloys*. Moscow, Metallurgiya [in Russian].
6. Suave, L.M., Cormier, J., Villechaise, P. et al. (2014) Microstructural evolutions during thermal aging of alloy IN625: Impact of temperature and forming process. *Metall. Mater. Sci.*, **45**, 2963–2982.

ORCID

N.O. Lysenko: orcid.org/0000-0003-2319-1260,
O.O. Pedash: orcid.org/0000-0003-1231-9951,
V.V. Klochykhin: orcid.org/0000-0002-0754-5543,
P.O. Kasai: orcid.org/0000-0003-2181-8381

CONFLICT OF INTEREST

The Authors declare no conflict of interest

CORRESPONDING AUTHOR

N.O. Lysenko
JSC “MOTOR SICH”, 69068, Zaporizhzhya,
Ukraine. E-mail: tb.ugmet@motorsich.com

SUGGESTED CITATION

N.O. Lysenko, O.O. Pedash, V.V. Klochykhin,
P.O. Kasai (2022) Influence of long-term soaking on
the structure and properties of IN625 alloy samples
made by selective laser melting. *The Paton Welding
J.*, **1**, 41–47.

JOURNAL HOME PAGE

<https://pwj.com.ua/en>

Received: 27.10.2021

Accepted: 07.02.2022

<https://doi.org/10.37434/tpwj2022.01.09>

METHODS AND MEANS OF EARLY VIBRATION DIAGNOSTICS OF ROTATING COMPONENTS OF MECHANISMS OF QUAY CONTAINER HANDLERS

I.M. Javorskyi^{1,2}, R.M. Yuzefovych^{1,3}, O.V. Lychak¹, P.O. Semenov⁴

¹Karpenko Physico-Mechanical Institute of the NASU
5 Naukova Str., 79060, Lviv, Ukraine,

²Politechnika Bydgoska
7 Prof. Sylwestra Kaliskiego, 85796, Bydgoszcz, Poland,

³Lviv Polytechnic National University
12 Stepan Bandera Str., 79013 Lviv, Ukraine,

⁴Odesa National Maritime University
34 I. Mechnikov Str., 65029, Odesa, Ukraine

ABSTRACT

The paper describes the properties of a model of vibration of interconnected rotating mechanisms in the form of biperiodically nonstationary random processes (BPNRP). Individual cases of such a model are considered, which enable performing data analysis by the method of periodically nonstationary random processes (PNRP). These methods are used to analyze the condition of mechanisms at increased vibration level. Separation of deterministic and stochastic vibrations was performed and parameters describing the structure of hidden periodicities of the first and second order were determined. The causes for increased vibration level were established.

KEY WORDS: lifting mechanism, vibration, periodical nonstationarity, deterministic oscillations, amplitude spectrum, stochastic high-frequency modulation, dispersion

INTRODUCTION

In vibration diagnostic systems the carriers of information on the technical condition of a mechanism are displacement, speed or acceleration of contact surfaces of the mechanisms, arising as a result of their defective part interaction. The nature of such an interaction is reflected in the parameters of the recorded vibration signals. In order to fulfill the description and analysis of the regularities of the latter, it is necessary to substantiate their adequate mathematical models, methods and algorithms of processing and computer support of the processes of extraction of the diagnostic features and taking decisions on the technical condition of the diagnosed object.

Vibration signals of rotating mechanisms are characterized by rhythmic variability, the main features of which are cyclic repeatability and stochasticity. Nonlinear effects, arising in mechanical systems at appearance of defects, lead to their interaction, which is reflected in the signal properties in the form of modulations. Such a modulation is quantitatively characterized by parameters, describing the structure of periodical or almost periodical time changes of moment functions of the first and second orders of the respective classes of nonstationary random processes [1–11]. It is rational to use these parameters at forma-

tion of diagnostic features to reveal the defects. As shown by investigations [1, 7–9, 12], application of such features enables detecting defects at early stages of their development and conducting effective monitoring of the diagnosed object.

Vibrations of mechanisms, consisting of many rotating components, have complex polyrhythmic structure. It is due, primarily, to different rotation speeds of individual elements. So, depending on the defect location, vibrations of the rolling bearing can be characterized by oscillations with shaft rotation frequencies, frequencies of rotation of the rolling bodies on the inner or outer rings, separator frequencies, as well as frequencies, determined by their combinations. Gear pair vibrations can have oscillations with shaft rotation frequencies, gear meshing frequencies and their combinations. Therefore, in the general case, vibrations can be described by polyperiodically nonstationary random processes [1, 3, 4], which belong to the class of almost periodically nonstationary processes. In the simplest case, when just two stochastic rhythms interact with each other, we come to a model in the form of a biperiodically nonstationary random process. Below we will briefly characterize such a model of vibration signal, and will consider separate cases, which allow substantiating analysis of vibrations of objects with complex kinematics, using the methods of periodically nonstationary random processes.

BPCRP MODEL OF A VIBRATION SIGNAL

The effectiveness of the methods of processing the cyclostationary signals at monitoring the machine condition can be generally explained by their ability to detect modulations, caused by appearance of malfunctions. The effects of modulation in the vibration model in the form of periodically correlated random processes (PCRP), which describe the stochastic repeatability with one period, are characterized by mutually stationary random processes in their harmonic representation [1, 11, 13]:

$$\xi(t) = \sum_{k \in Z} \xi_k(t) e^{ik \frac{2\pi}{P_1} t},$$

where Z is the set of integers i ; P_1 is the period of non-stationarity (period of rotation of one of the gears). Generalizing these representations, we can come to the conclusion that modulation of two stochastic periodicities which is due to rotation of the two gears can be expressed as follows:

$$\xi(t) = \sum_{k \in Z} \xi_k^{(P_2)}(t) e^{ik \frac{2\pi}{P_1} t}, \quad (1)$$

where frequency harmonic $2\pi/P_1$ and its multiples are modulated by PCRP with period P_2 :

$$\xi_k^{(P_2)}(t) = \sum_{l \in Z} \xi_{kl}(t) e^{il \frac{2\pi}{P_2} t}.$$

Therefore, for random process (1), we have:

$$\xi(t) = \sum_{k, l \in Z} \xi_{kl}(t) e^{i\Lambda_{kl} t}, \quad (2)$$

where $\xi_{kl}(t)$ are the mutually stationary random processes and $\Lambda_{kl} = k \left(\frac{2\pi}{P_1} \right) + l \left(\frac{2\pi}{P_2} \right)$. Note that process

(2) is the sum of amplitude- and phase-modulated harmonics, where Λ_{kj} frequencies are a linear combination of two fundamental frequencies $\Lambda_{10} = k(2\pi/P_1)$ and $\Lambda_{01} = l(2\pi/P_2)$. Mathematical expectations of modulating processes $m_{kl} = E\xi_{kl}(t)$ are Fourier coefficients of the mean function:

$$m(t) = E\xi(t) = \sum_{k, l \in Z} m_{kl} e^{i\Lambda_{kl} t}. \quad (3)$$

For correlation function $R(t, \tau) = E\overset{\circ}{\xi}(t)\overset{\circ}{\xi}(t + \tau)$, $\overset{\circ}{\xi}(t) = \xi(t) - m(t)$ we have:

$$R(t, \tau) = \sum_{k, l \in Z} R_{kl}(\tau) e^{i\Lambda_{kl} t}, \quad (4)$$

where

$$R_{kl}(\tau) = \sum_{p, q \in Z} r_{p-k, q-l, p, q} e^{i\Lambda_{pq}\tau}, \quad (5)$$

and $r_{pqkl}(\tau) = E\overset{\circ}{\xi}_{pq}(t)\overset{\circ}{\xi}_{kl}(t + \tau)$, $\overset{\circ}{\xi}_{pq}(t) = \xi_{pq}(t) - m_{pq}$ are the cross-correlation functions of the modulation process, sign “ $\overset{\circ}{-}$ ” denotes complex conjugation. Thus, Fourier coefficients of correlation function (4) are defined by cross-correlation functions of modulating processes, where the indices are shifted by k and l , respectively. It follows from (5) that mutual correlations of modulating processes $\overset{\circ}{\xi}_{kl}(t)$ with different indices lead to biperiodical nonstationarity of the second order. This results in correlations of the respective spectral components, which are quantitatively characterized by Fourier transformation of expression (5):

$$f_{kl}(\omega) = \frac{1}{2\pi} \int_{-\infty}^{\infty} R_{kl}(\tau) e^{-i\omega\tau} d\tau. \quad (6)$$

It follows from (5) that:

$$f_{kl}(\omega) = \sum_{p, q \in Z} f_{p-k, q-l, p, q}(\omega - \Lambda_{pq}),$$

where

$$f_{pqkl}(\omega) = \frac{1}{2\pi} \int_{-\infty}^{\infty} r_{pqkl}(\tau) e^{-i\omega\tau} d\tau$$

are the mutually spectral densities of modulating processes $\overset{\circ}{\xi}_{pq}(t)$. Values (5) and (6) are called the correlation and spectral components, respectively [1–3]. Zero correlation component $R_{00}(\tau)$ is defined by

self-correlated function $r_{pq}(\tau) = E\overset{\circ}{\xi}_{pq}(t)\overset{\circ}{\xi}_{pq}(t + \tau)$:

$$R_{00}(\tau) = \sum_{p, q \in Z} r_{pq}(\tau) e^{-i\Lambda_{pq}\tau}.$$

This is the time-averaged correlation function of random process (2), i.e. the correlation function of its stationary approximation.

Zero spectral component

$$f_{00}(\omega) = \sum_{p, q \in Z} f_{pq}(\omega - \Lambda_{pq}) \quad (7)$$

is the spectral density of stationary approximation power for (2). It defines the spectral decomposition of time-averaged instantaneous power of oscillations $R(0, t)$. Random processes, mathematical expectations and correlation function, which are biperiodic functions and which can be represented by series (3) and (4), are called BPCRP. Fourier coefficients of the correlation function and spectral density are the general characteristics of amplitude and phase modulation of BPCRP carrier harmonics. Zero spectral

component, as one can see from (7), is the total power of spectral densities of modulating processes $\xi_{pq}(t)$, shifted by Λ_{pq} . Spectral component $f_{kl}(\omega)$ (6) is the sum of shifted mutually spectral densities of modulating processes, where the indices differ by k and l , respectively. Proceeding from the above statements, we can conclude that $f_{00}(\omega)$ describes the oscillation spectrum, and $f_{kl}(\omega)$ functions give the correlation of this spectrum harmonics, where the frequencies are shifted by $\Lambda_{kl} = k\left(\frac{2\pi}{P_1}\right) + l\left(\frac{2\pi}{P_2}\right)$. These correlations are not equal to zero, except if the processes of modulation with the respective numbers are interrelated.

Individual cases of hidden periodicity of biorhythms are easily derived from expression (2). We will extract only those of them, which can be readily analyzed in terms of PNRP approach.

Suppose that $\xi_{kl}(t) = c_{kl} + \xi_{k0}(t) + \xi_{0l}(t)$, where c_{kl} are certain complex numbers, while $\xi_{k0}(t)$ and $\xi_{0l}(t)$ — are stationary random processes. Then:

$$\begin{aligned} \xi(t) = & \sum_{k,l \in Z} c_{kl} e^{i\Lambda_{kl}t} + \sum_{k \in Z} \xi_{k0}(t) e^{ik\frac{2\pi}{P_1}t} + \\ & + \sum_{l \in Z} \xi_{0l}(t) e^{il\frac{2\pi}{P_2}t} = s(t) + \xi_1(t) + \xi_2(t). \end{aligned} \quad (8)$$

Here, $s(t)$ is the biperiodic function. If $\{\xi_{k0}(t), k \in Z\}$ and $\{\xi_{0l}(t), l \in Z\}$ sets are uncorrelated, and random processes which belong to each of them, are stationary coupled, then $\xi_1(t)$ and $\xi_2(t)$ are PNRP. Ad-

ditive model (8) can be applied to analysis of vibrations of two damaged components, where development of defects does not affect each other. In the case of a single-defect component, one of the PNRP in representation (8) becomes a stationary random process. Then, the random processes, which describe the modulations, namely $\xi_{k0}(t)$ or $\xi_{0l}(t)$, are uncorrelated.

We derive a multiplicative model in the form of the product of two PNRP with different periods P_1 and P_2 in the case, when $\xi_{kl}(t) = \xi_{k0}(t)\xi_{0l}(t)$. Then:

$$\xi(t) = \sum_{k \in Z} \xi_{k0}(t) e^{ik\frac{2\pi}{P_1}t} \sum_{l \in Z} \xi_{0l}(t) e^{il\frac{2\pi}{P_2}t} = \xi_1(t)\xi_2(t).$$

Analysis of such a model can be performed by PNRP methods, if one of the periods significantly exceeds the value of the other one. If only one of the components is defective, then actually its vibrations will be described by PNRP, and those of the other one — by a stationary random process $\eta(t)$. Then, $\xi(t) = \eta(t)\xi_1(t)$. In such a presentation, the influence of a defectfree component is reflected in the interaction of modulation characteristics of the damaged component carrier harmonics.

INVESTIGATION OF VIBRATIONS OF QUAY CONTAINER HANDLER

In September, 2021, the staff of the Department of the Methods and Means of Extraction and Processing of Diagnostic Signals of G.V. Karpenko Physico-Mechanical Institute of the NAS of Ukraine (PMI), together with the representatives of PORTTEKH-

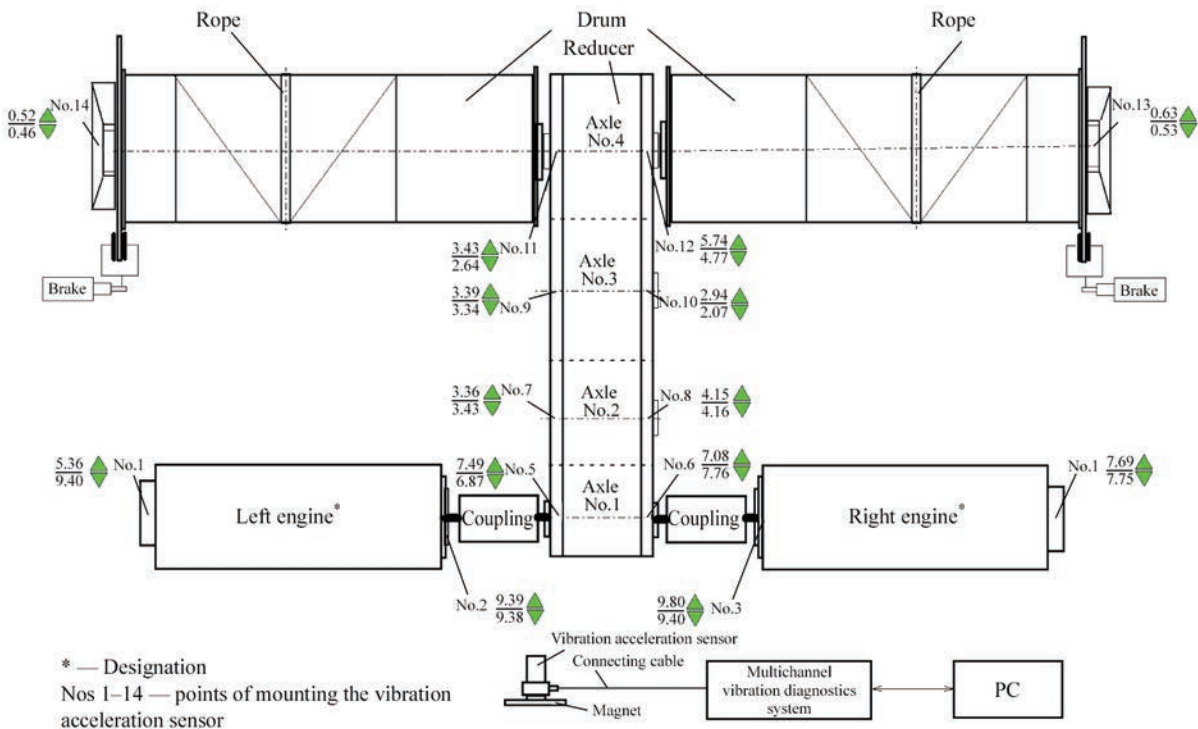


Figure 1. Scheme of arrangement of control points and measured RMS values of vibration acceleration (lifting and lowering) for Crane 1

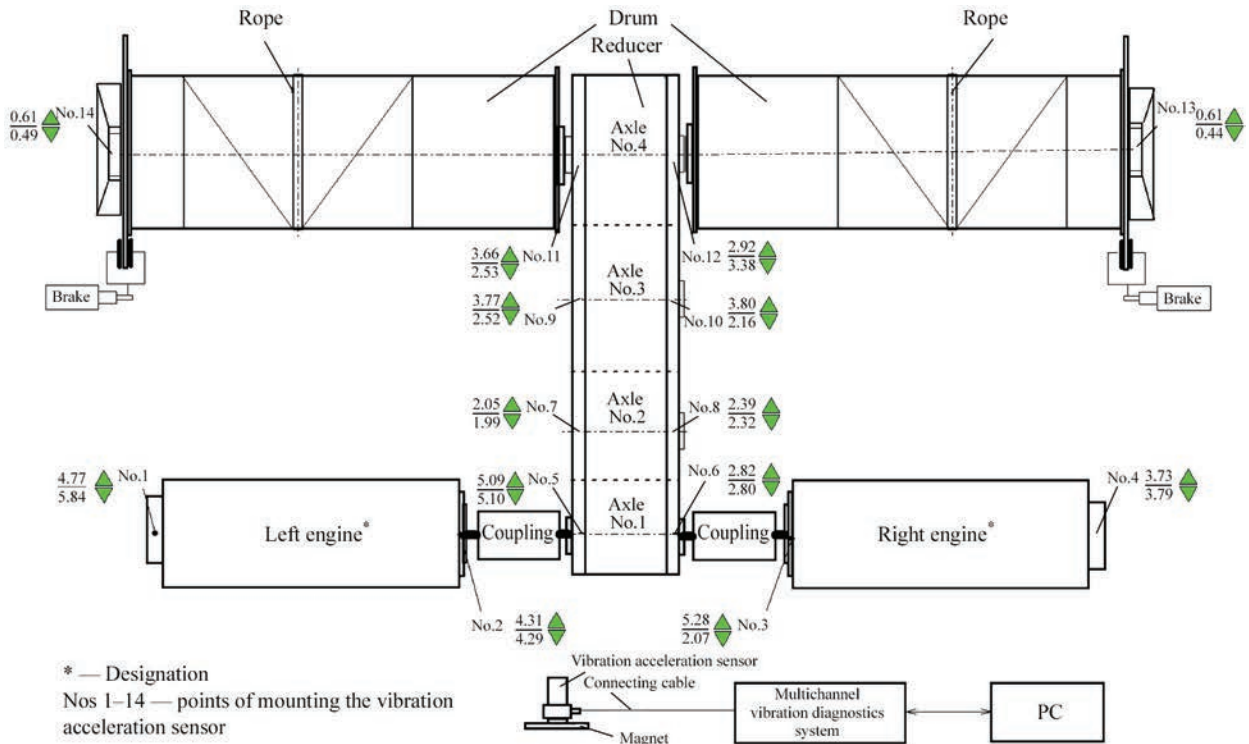


Figure 2. Scheme of arrangement of control points and measured RMS values of vibration acceleration (lifting and lowering) for Crane 2

EXPERT Company performed measurements and recording of signals of vibrations of lifting mechanism of quay container handlers ZPMC (Crane 1 and Crane 2, respectively), which belong to Brooklyn Kyiv Port Company. This Company is the operator of container terminal based on quays Nos 42, 43 of State Company “Odessa Sea Trade Port”.

The layout of drive mechanism control points is given in Figures 1, 2. During performance of measurements, the sensors were fastened to the mechanism housing by magnets. Vibration acceleration was recorded in each point, and its root mean square

(RMS) value was determined at crane mechanism operation for lifting and lowering of the spreader without the payload, using vibration acceleration sensors AVS-117. The sampling frequency of vibration signals was 10 kHz, the input signal frequency band was from 2 Hz to 2 kHz, and duration of recording the signal realizations for each control point was 2 s.

Determination of vibration levels of the mechanisms was conducted in keeping with DSTU ISO 10816-1:2007 “Classes of mechanisms and their vibration norms” by vibration diagnostic system COMPACT-VIBRO, which was developed at PMI [15, 16].

Table 1. Evaluation of the mechanism technical condition by vibration intensity (ISO 2372)

Vibration level (RMS value)		Mechanism classes				
By vibration speed	By vibration acceleration	Small mechanisms $P < 15 \text{ kW}$	Medium-sized mechanisms $15 \text{ kW} < P < 75 \text{ kW}$	Large-sized mechanisms on rigid foundations $P > 300 \text{ kW}$	Large-sized mechanisms with non-rigid fastening $P > 300 \text{ kW}$	
mm/s	m/s^2	Class 1	Class 2	Class 3	Class 4	
44.6	70.1	C	C	C	C	
28.2	44.2			B	B	
17.8	27.9			A	A	
11.2	17.6			B	A	A
7.1	11.1					
4.5	7.2					
2.8	4.4					
1.8	2.8	A	A	A		
1.12	1.8					
0.71	1.1					
0.45	0.7	A	A	A	A	

A — satisfactory vibration value; B — admissible vibration value; C — emergency vibration value.

Table 2. Calculated RMS values of vibration acceleration of mechanism drive elements for Crane 1

Point number	Component description	Actual RMS value, m/s ²		Boundary RMS values, m/s ²
		At lifting	At lowering	
1	Left engine	5.36	9.40	11.1
2		9.39	9.38	11.1
3	Right engine	9.80	9.40	11.1
4		7.69	7.75	11.1
5	Reducer	7.49	6.87	11.1
6		7.08	7.76	11.1
7		3.36	3.43	11.1
8		4.15	4.16	11.1
9		3.39	3.34	11.1
10		2.94	2.07	11.1
11		3.43	2.64	11.1
12		5.74	4.77	11.1
13	Outrigger of the right drum	0.63	0.53	11.1
14	Outrigger of the left drum	0.52	0.46	11.1

Table 3. Calculated RMS values of vibration acceleration of mechanism drive elements for Crane 2

Point number	Component description	Actual RMS value, m/s ²		Boundary RMS values, m/s ²
		At lifting	At lowering	
1	Left engine	4.77	5.84	11.1
2		4.31	4.29	11.1
3	Right engine	5.28	2.07	11.1
4		3.73	3.79	11.1
5	Reducer	5.09	5.10	11.1
6		2.82	2.80	11.1
7		2.05	1.99	11.1
8		2.39	2.32	11.1
9		3.77	2.52	11.1
10		3.80	2.16	11.1
11		3.66	2.53	11.1
12		2.92	3.38	11.1
13	Outrigger of the right drum	0.61	0.44	11.1
14	Outrigger of the left drum	0.61	0.49	11.1

In keeping with DSTU ISO 10816-1:2007 the examined mechanisms belong to class 3 (powerful prime movers and other powerful mechanisms with rotating masses, mounted on massive foundations relatively rigid in the direction of vibration measurement).

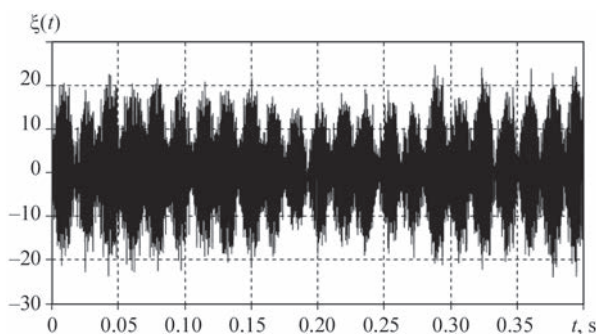
Normative RMS values of vibration acceleration, which allow evaluation of the technical condition of the mechanism in keeping with the established norms of vibration intensity, are given in Table 1.

Evaluation of the condition of mechanism components was based on determination of RMS value of vibration accelerations (see Tables 2, 3).

As follows from Table 2, mean root square values of vibrations in bearing units of Crane 1 turned out to be higher and close to boundary values. In order to determine the causes for such a condition, the derived realizations of vibration signals were analyzed using the procedure developed by us.

ANALYSIS OF VIBRATION STRUCTURE AND DETERMINATION OF ITS PARAMETERS

The segment of realization of one of the recorded signals of vibration acceleration is shown in Figure 3. As one can see from Figure 3, vibrations have the form of clearcut groups, following each other with the frequency of approximately 60 Hz. In order to establish the general properties of the signals, in particular, their spectral composition, the correlation functions and spectral densities of their stationary approxima-

**Figure 3.** Signal realization segment

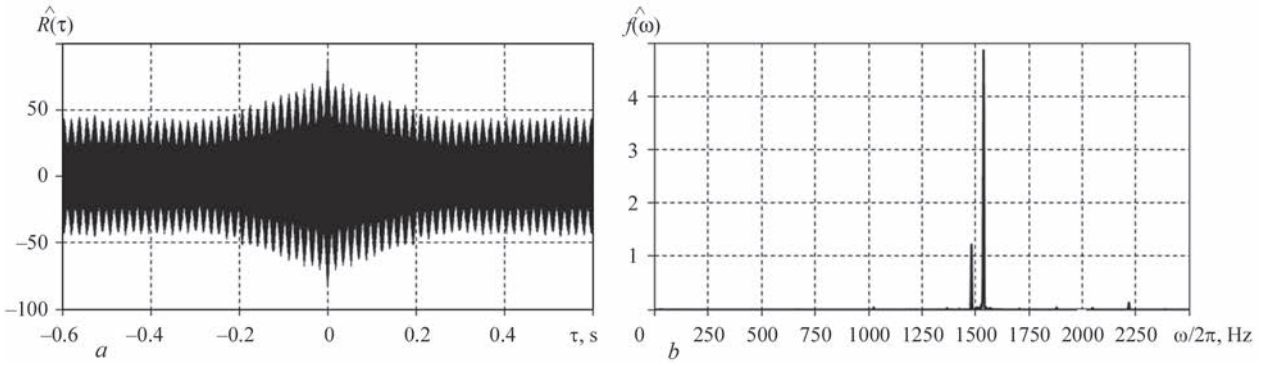


Figure 4. Evaluation of the correlation function (a) and spectral density (b)

tions were calculated. The following dependencies were used for this purpose:

$$\hat{R}(jh) = \frac{1}{K} \sum_{n=0}^{K-1} [\xi(nh) - \hat{m}] [\xi((n+j)h) - \hat{m}],$$

$$\hat{m} = \frac{1}{K} \sum_{n=0}^{K-1} \xi(nh),$$

$$\hat{f}(\omega) = \frac{h}{2\pi} \sum_{n=-L}^L k(nh) \hat{R}(nh) \cos \omega nh,$$

where $h = T/K$ is the discretization step; T is the time of signal recording; j is the integer number; $L = \tau_m/h$ is the natural number; τ_m is the point of correlogram truncation; $k(nh)$ is the correlation window. In this case, Hamming window was selected:

$$k(\tau) = \begin{cases} 0.54 + 0.46 \cos \frac{\pi\tau}{\tau_m}, & |\tau| \leq \tau_m, \\ 0, & |\tau| > \tau_m. \end{cases}$$

Results of calculation of one of the signals are shown in the form of graphic dependencies in Figure 4. It follows from the data of Figure 4, that group structure is preserved also in the dependence of the correlation function on the shift. Its characteristic feature also is the nonvanishing “tail”, which is indicative of the presence of a deterministic component in the vibration composition. Frequency dependence

of the signal spectral density shows (Figure 4, b) that the main part of vibration power is concentrated in the high-frequency region, the high-frequency oscillations being mostly the narrowband ones. The values of spectral density in the low-frequency region are barely noticeable against the background of powerful peaks in [1.4 kHz; 1.6 kHz] range. Therefore, for a more probable analysis of the low-frequency vibrations, we will divide the frequency region of the signals into two ranges: [0 kHz; 1.0 kHz] and [1.0 kHz; 2.5 kHz]. The graphs of evaluation of the correlation function and spectral density of the low-frequency signal component power are given in Figure 5. The spectral density is of a peaked nature, and nonvanishing oscillations of the correlation function show that this spectrum is mixed and a considerable fraction of the signal power belongs to deterministic oscillations.

Further detalization of vibration structure requires, first of all, separating their deterministic and stochastic components. The first step in such a separation is determination of the nonstationarity period (basic frequency) of deterministic oscillations. For this purpose, it is rational to use the least squares method as the most effective one [1, 17], which is reduced to searching for the coordinates of the maximum values of functional:

$$\hat{F}_1(\theta) = \frac{1}{2K+1} \sum_{n=-K}^K \hat{m}^2(\theta, nh), \quad (9)$$

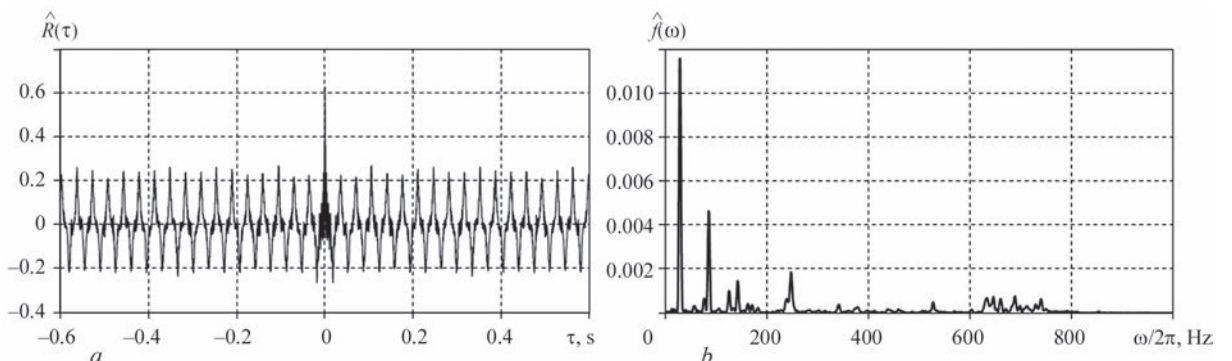


Figure 5. Evaluation of the correlation function (a) and spectral density (b) of the low-frequency signal

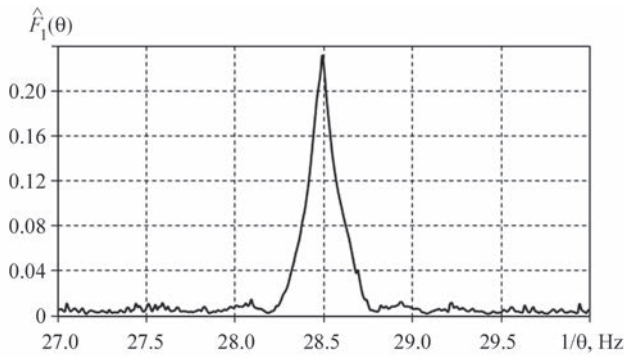


Figure 6. Quadratic functional (13), depending on trial frequency where

$$\hat{m}_1(\theta, nh) = \sum_{k=1}^{L_1} \left[\hat{m}_k^c(\theta) \cos k \frac{2\pi}{\theta} nh + \hat{m}_k^s(\theta) \sin k \frac{2\pi}{\theta} nh \right],$$

$$\begin{cases} \hat{m}_k^c(\theta) \\ \hat{m}_k^s(\theta) \end{cases} = \frac{2}{2K+1} \sum_{n=-K}^K \xi(nh) \begin{cases} \cos k \frac{2\pi}{\theta} nh \\ \sin k \frac{2\pi}{\theta} nh \end{cases}, \quad (10)$$

while θ is the so-called “trial” period and L_1 is a certain chosen number of the harmonics. Note that the maximum value of functional (9) is close to average power of the deterministic component of oscillations.

The graph of the dependence of quadratic functional (9) on trial frequency $f = 1/\theta$ for $L_1 = 30$ is shown in Figure 6. Frequency value at which the functional value reaches its maximum was taken as the estimate of

basic frequency $\hat{f}_0 = 1/\hat{P}_1$. With an accuracy of up to three digits we find $\hat{f}_0 = 28.480$ Hz. The found value corresponds to the engine rotor frequency. Total power of

the rotation harmonics, which is determined by value (9) in

point \hat{f}_0 , is equal to $\hat{F}_1\left(\frac{1}{\hat{f}_0}\right) = 0.24\left(\frac{\text{m}}{\text{s}^2}\right)^2$. This value

is equal to a little less than half of the total power of low-frequency oscillations, which is determined by the value of correlation function evaluation in point τ

$= 0$, i.e. $\hat{R} = (0) = 0.62\left(\frac{\text{m}}{\text{s}^2}\right)^2$ (see Figure 5, a).

Substituting \hat{f}_0 value into formula (10) instead of $1/\theta$, we will calculate the cosine and sine coefficients, and proceeding from them — the amplitudes of the respective harmonics:

$$A(k\hat{f}_0) = \sqrt{(\hat{m}_k^c)^2 + (\hat{m}_k^s)^2}. \quad (11)$$

The amplitude spectrum (11) in the form of a diagram is shown in Figure 7, b. As we can see the spectrum is rather wide. However, the greatest part of the deterministic oscillation power belongs to the first three harmonics.

Figure 7, a, shows the time dependence of periodic function:

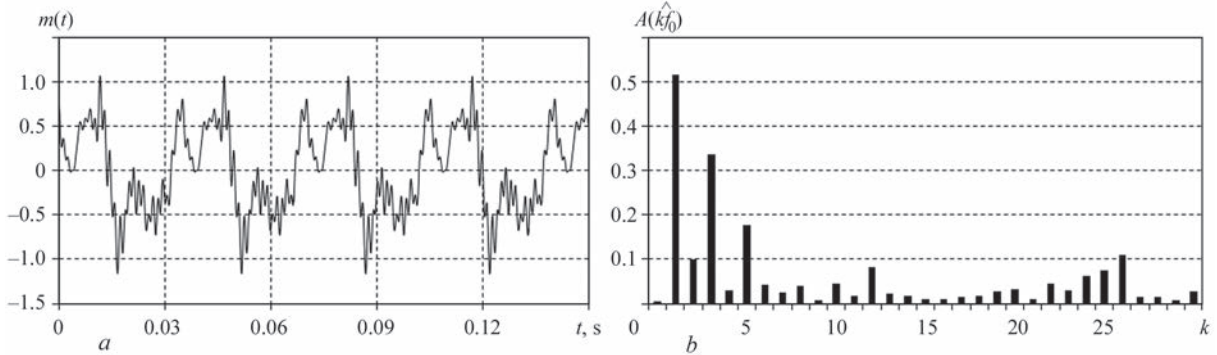


Figure 7. Deterministic oscillations (a) and their amplitude spectrum (b)

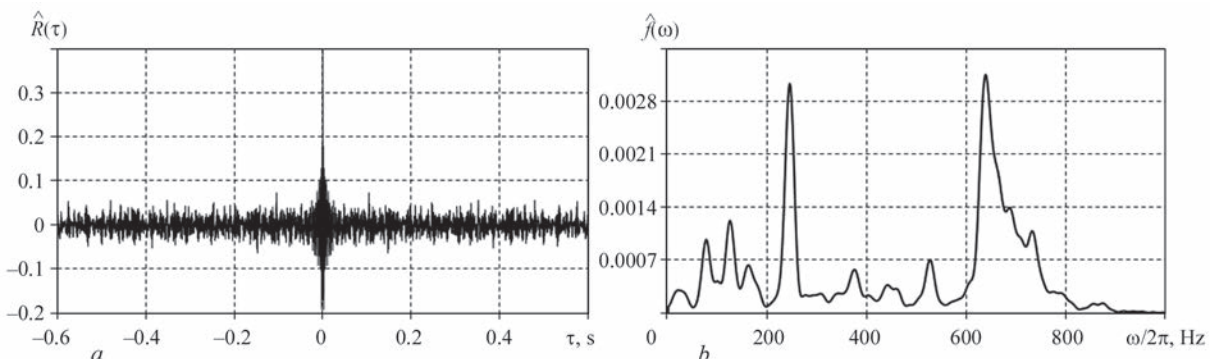


Figure 8. Evaluation of the correlation function (a) and spectral density (b) of the stochastic component of low-frequency signal

$$\hat{m}(t) = \sum_{k=1}^{30} [\hat{m}_k^c(\theta) \cos 2\pi k f_0 t + \hat{m}_k^s(\theta) \sin 2\pi k f_0 t], \quad (12)$$

which, if the following condition is satisfied:

$$h \leq \frac{P_1}{2L_1 + 1}$$

is the interpolation formula for the deterministic vibrations, excited by rotor rotation.

Knowing dependence (12) for all $t \in [0, P_1]$, we will separate residual vibrations $\dot{\xi}(t) = \xi(t) - \hat{m}(t)$ and will conduct their spectral-correlation analysis. The graphs of correlation function and spectral density, calculated on the base of time series $\dot{\xi}(nh)$, are shown in Figure 8. The correlation function now vanishes quickly to the level of low-power oscillations (Figure 8, *a*). The residual spectral density, similar to the initial signal, has a ridge-like structure (Figure 8, *b*), which is due to low-power harmonics with the frequencies characteristic for the bearing, their combinations, as well as narrowband stochastic modulation of these harmonics. These low-power residual oscillations have a slight influence on the mechanism operation, so that now we can extract a deterministic periodic function in formula (8), which is presented by finite series (12).

Now we will move over to analysis of vibrations in [1.0 kHz; 2.5 kHz] range (Figure 9). Evaluation of

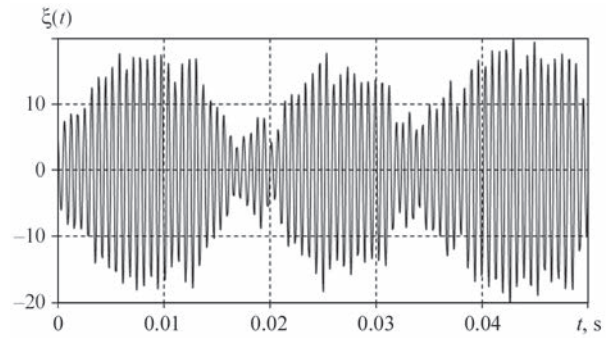


Figure 9. High-frequency signal realization segment

the correlation function at large shifts has the form of nonvanishing high-frequency oscillations (Figure 10, *a, b*) that can be caused by the presence of a deterministic component. In order to confirm such an assumption, we will calculate functional (9), varying the trial frequency in [1470 Hz, 1490 Hz] and [1525 Hz, 1545 Hz] ranges. Obtained clearcut peaks in the graphs of frequency dependence of functional (13) at frequencies $\hat{f}_0^1 = 1481.13$ Hz and $\hat{f}_0^2 = 1538.11$ Hz (Figure 11, *a, b*) provide an affirmative answer to this. Having calculated by expressions (10) the respective harmonic amplitudes, we have $A(\hat{f}_0^1) = 4.163$ m/s² and $A(\hat{f}_0^2) = 7.833$ m/s². Total power of the harmonics is equal to 39.35 (m/s²)² that is equal to approximately half of the total power of high-frequency vibrations.

We will express the high-frequency deterministic oscillations as follows:

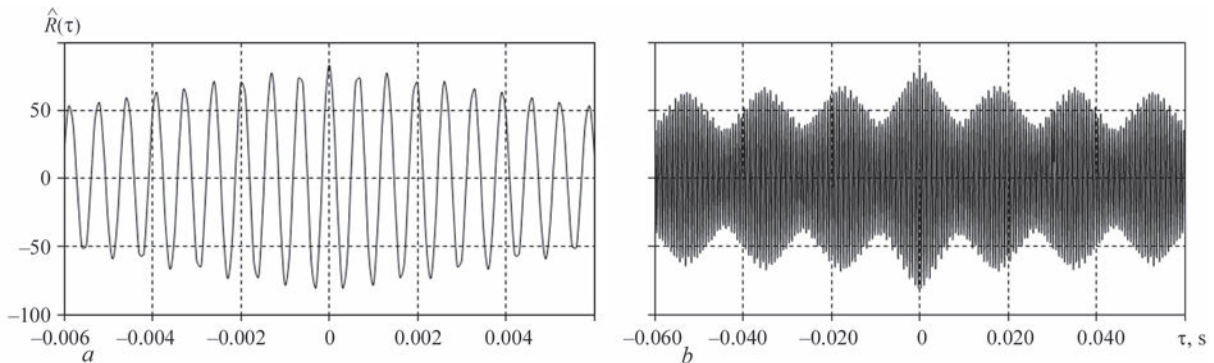


Figure 10. Evaluation of the correlation function of high-frequency signal for initial (*a*) and large (*b*) shifts

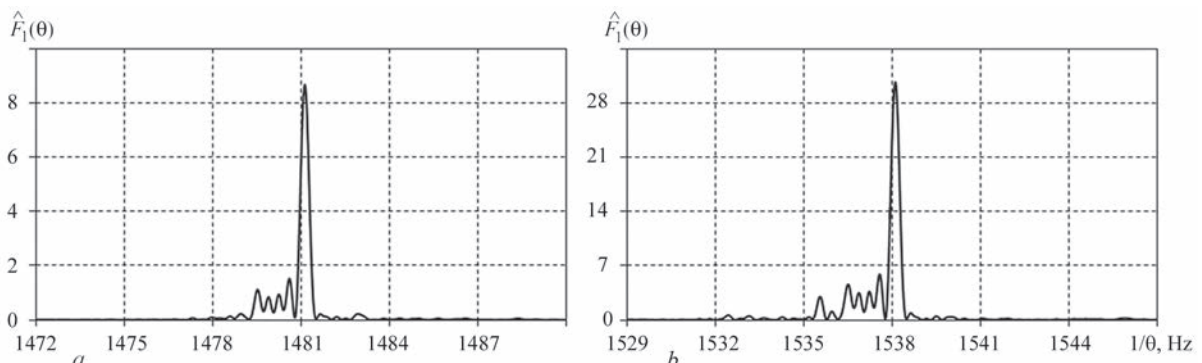


Figure 11. Dependencies of functional (9) on trial frequency in different frequency bands (*a*) and (*b*)

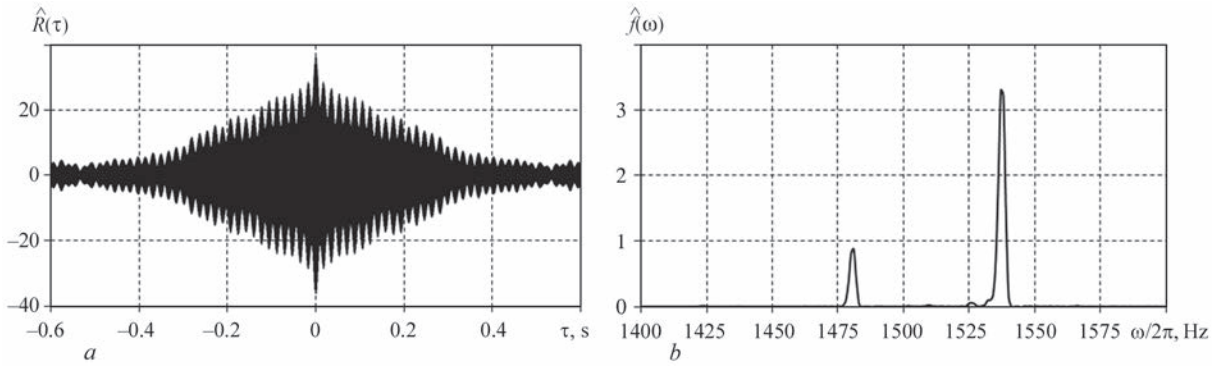


Figure 12. Correlation function (a) and spectral density (b) of the stochastic component of high-frequency signal

$$s_2(t) = \sum_{k=1}^2 \left[\hat{a}_k(f_0^{(k)}) \cos 2\pi f_0^{(k)} t + \hat{b}_k(f_0^{(k)}) \sin 2\pi f_0^{(k)} t \right], \quad (12)$$

and will extract the stochastic component $\xi(nh) = \xi(nh) - s_2(t)$. Evaluation of its correlation function is slowly oscillationally vanishing to the level of low-power fluctuations and has group structure (Figure 12, a). Therefore, evaluation of spectral density, based on its correlation function, is peaked. Here, there exist two peaks, which are much larger than the others in magnitude at frequencies which practically coincide with those of the deterministic harmonics (Figure 12, b). Addition of oscillations with such close frequencies leads to the phenomenon of beating, where oscillations with frequency difference $f_1 - f_2$ are the frequencies, with which the main oscillation groups follow each other. Such beating is observed on the graphs of realization and evaluation of the correlation function.

In order to clarify whether these high-frequency oscillations are related to the low-frequency ones and in which way, we will search for hidden periodicities of the second order in the range, to which the rotor frequency belongs. For this purpose we will also use the least squares method, which in this case is reduced to analysis of frequency dependence of the functional:

$$\hat{F}_2(\theta) = \frac{1}{2K+1} \sum_{n=-K}^K R^2(nh, \theta), \quad (13)$$

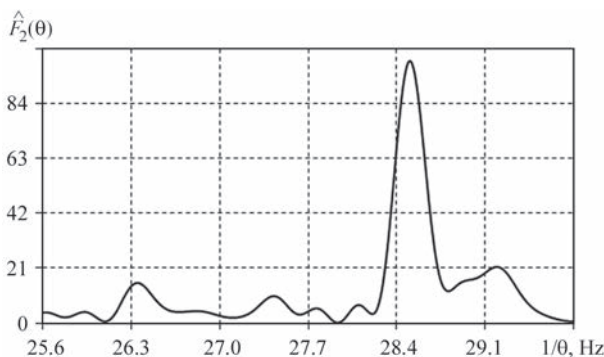


Figure 13. Dependence of quadratic functional (13) on trial frequency

where

$$\hat{R}(nh, \theta) = \sum_{k=1}^{L_2} \left[\hat{R}_k^c(\theta) \cos k \frac{2\pi}{\theta} nh + \hat{R}_k^s(\theta) \sin k \frac{2\pi}{\theta} nh \right], \quad (14)$$

$$\begin{cases} \hat{R}_k^c(\theta) \\ \hat{R}_k^s(\theta) \end{cases} = \frac{2}{2K+1} \sum_{n=-K}^K \xi^2(nh) \begin{cases} \cos k \frac{2\pi}{\theta} nh \\ \sin k \frac{2\pi}{\theta} nh \end{cases}, \quad (15)$$

Here, L_2 is the selected number of addends in the sum (14). For calculations it was assumed that $L_2 = 5$. Figure 13 presents the dependence of functional (13) on trial frequency $f = 1/\theta$. A pointed peak at frequency $\hat{f}_0 = 28.5$ Hz, which is close to that of rotor frequency, does not leave any doubt that the dispersion and correlation function of the stochastic component of vibrations are periodic function with engine rotor rotation period. As no other periodicities were revealed at analysis, presentations (8) in this case can be regarded as PNRP with period $P = P_1$.

Taking $\theta = \hat{P} = 1/\hat{f}_0$, in (15), we will calculate Fourier coefficients of dispersion and its average value:

$$\hat{R}_0 = \frac{1}{2K+1} \sum_{n=-K}^K \xi^2(nh).$$

Based on these values, we will formulate the following expression:

$$\hat{R}(t, \theta) = \hat{R}_0 + \sum_{k=1}^5 \left[\hat{R}_k^c(\theta) \cos k \frac{2\pi}{\hat{P}} t + \hat{R}_k^s(\theta) \sin k \frac{2\pi}{\hat{P}} t \right], \quad (16)$$

which, provided

$$h \leq \frac{\hat{P}}{2L_2 + 1}$$

is the interpolation formula for dispersion. The graph of time dependence of dispersion (16) and its amplitude spectrum

$$\hat{V}(k\hat{f}_0) = \sqrt{\left[\hat{R}_k^c(\hat{P}) \right]^2 + \left[\hat{R}_k^s(\hat{P}) \right]^2}$$

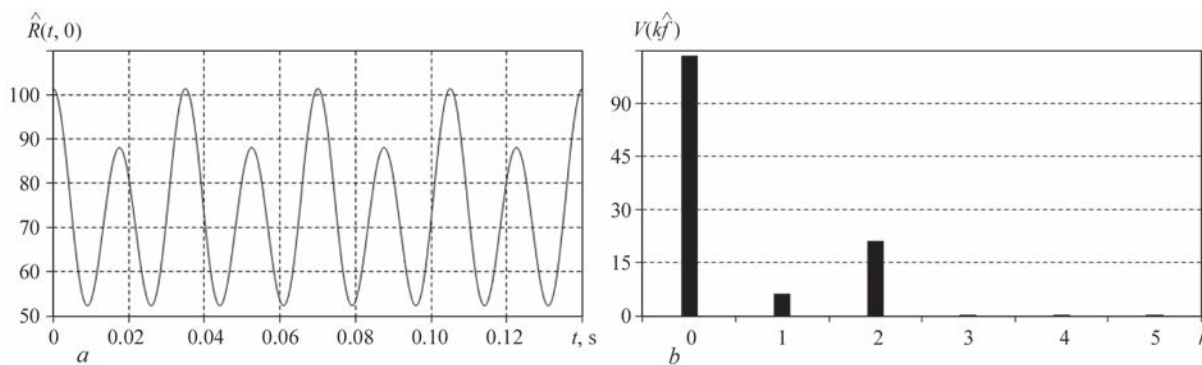


Figure 14. Dispersion (a) and its amplitude spectrum (b)

are shown in Figure 14. Only zero, first and second harmonics are significantly expressed in the spectrum.

Therefore, proceeding from the above results, we can assume that the time variability of dispersion is the result of modulation of the harmonics of low-frequency deterministic oscillations by stochastic high-frequency band oscillations, resulting from damage. The correlation function of such oscillations can be approximated by slowly vanishing oscillations with resonance frequency ν_0 . The result of such a modulation in the frequency range is observed as narrow-band peaks at frequencies $\nu_0 \pm k\hat{f}_0$ (Figure 11). Each high-frequency narrowband composition is a stationary random process; they, however, are cross-correlated. Here the cross-correlations of the components, the frequency distance between which is equal to $k\hat{f}_0$, determine the k -th component of dispersion. Based on these considerations, we can conclude that the second harmonics of dispersion is the result of modulation of the most powerful first harmonic of deterministic oscillations. Such a modulation leads to appearance of peak values in the frequency region at $\nu_0 - \hat{f}_0$ and $\nu_0 + \hat{f}_0$ frequencies. The cross-correlation function of these two stationary narrowband random processes, where the spectra are separated by $2\hat{f}_0$, determines the second harmonic of dispersion.

The detected modulations can be studied further on using Hilbert transform [18]. However, the above-established facts on the signal structure allow making a conclusion about the nature of the damage. An increased vibration level is not related to the probable defects in one of the bearing elements, but is attributable to wear of the bearing housing seat as a result of long-term operation of the mechanism. “Worn-out” hole in the housing causes sliding of the bearing outer ring, which, in its turn, excites powerful high-frequency oscillations.

CONCLUSIONS

The COMPACT-VIBRO system, developed at G.V. Karpenko Physico-Mechanical Institute of the NAS

of Ukraine was used to select and analyze vibration signals from container handler mechanisms.

The methods for detection of hidden periodicities based on models in the form of PNRP and their generalizations were used to separate the deterministic and stochastic components of signals with higher RMS value level and to establish the characteristic features of each of them. The amplitude spectrum of deterministic components of vibrations was determined, and the deterministic and stochastic high-frequency modulation of their harmonics was detected. It is shown that such a modulation causes periodic nonstationarity of the second order with shaft rotor rotation period. The amplitude spectrum of time changes of signal dispersion was determined, and its connection with cross-correlations of the signal narrow-band high-frequency components was shown. The cause for the high vibration level, proceeding from the narrow band of dispersion spectrum and low values of its first harmonics, is bearing bushing damage propagation at the initial stage.

Calculated RMS values for Crane 1 and Crane 2 are within the normative range.

REFERENCES

1. Javorskyj, I.M. (2013) *Mathematical models and analysis of stochastic oscillations*. Lviv, PMI of NAS of Ukraine [in Ukrainian].
2. Javorskyj, I., Mykhailyshyn, V. (1996) Probabilistic models and statistical analysis of stochastic oscillations. *Pattern Recogn. Image Anal.*, 6(4), 749–763.
3. Javorskyj, I., Yuzefovych, R., Kravets, I., Matsko, I. (2014) Methods of periodically correlated random processes and their generalizations. Cyclostationarity: Theory and Methods. Lecture Notes in Mechanical Engineering. Ed. by F. Chaari, J. Leskow, A. Sanches-Ramires. New York, Springer Int. Publish. Switzerland, 73–93.
4. Javorskyj, I., Dzeryn, O., Yuzefovych, R. (2019) Analysis of mean function discrete LSM-estimator for biperiodically nonstationary random signals. *Math. Model. Comput.*, 6(1), 44–57.
5. McCormick, A.C., Nandi, A.K. (1998) Cyclostationarity in rotating machine vibrations. *Mech. Syst. Signal Process.*, 12(2), 225–242.

6. Capdessus, C., Sidahmed, M., Lacoume, J.L. (2000) Cyclostationary processes: Application in gear fault early diagnostics. *Mech. Syst. Signal Process.*, **14**(3), 371–385.
7. Antoni, J., Bonnardot, F., Raad, A., El Badaoui, M. (2004) Cyclostationary modeling of rotating machine vibration signals. *Mech. Syst. Signal Process.*, **18**, 1285–1314.
8. Antoni, J. (2009) Cyclostationarity by examples. *Mech. Syst. Signal Process.*, **23**, 987–1036.
9. Randall, R.B., Antoni, J. (2011) Rolling element bearing diagnostics — A tutorial. *Mech. Syst. Signal Process.*, **25**(2), 485–520.
10. Zimroz, R., Bartelmus, W. (2009) Gearbox condition estimation using cyclostationary properties of vibration signal. *Key Engineering Mater.*, **413**(1), 471–478.
11. Hurd, H.L., Miamee, A. (2007) *Periodically correlated random sequences: Spectral theory and practice*. New York, Wiley.
12. Javorskyj, I., Kravets, I., Matsko, I., Yuzefovych, R. (2017) Periodically correlated random processes: Application in early diagnostics of mechanical systems. *Mech. Syst. Signal Process.*, **83**, 406–438.
13. Javorskyj, I., Matsko, I., Yuzefovych, R. et al. (2021) Methods of hidden periodicity discovering for gearbox fault detection. *Sensors.*, **21**, 6138.
14. Javorskyj, I., Leśkow, J., Kravets, I. et al. (2011) Linear filtration methods for statistical analysis of periodically correlated random processes. Pt II: Harmonic series representation. *Signal Process.*, **91**, 2506–2519.
15. Yuzefovych, R., Javorskyj, I., Matsko, I. et al. (2020) Devices for detection of defects at early stages of their initiation at determination of technical condition of mechanisms. *Tekh. Diahnost. ta Neruiniv. Kontrol*, **4**, 8–16 [in Ukrainian]. DOI: <https://doi.org/10.37434/tdnk2020.04.02>.
16. Javorskyj, I., Yuzefovych, R., Lychak, O. et al. (2021) Methods and means of early vibrodiagnostics of bearing units of rotary mechanisms. *Tekh. Diahnost. ta Neruiniv. Kontrol*, **2**, 30–37 [in Ukrainian]. DOI: <https://doi.org/10.37434/tdnk2021.02.04>.
17. Javorskyj, I., Yuzefovych, R., Matsko, I., Zakrzewski, Z. (2021) The least square estimation of the basic frequency for periodically non-stationary random signals. *Digital Signal Process.*, **116**, 103113. DOI: <https://doi.org/10.1016/j.dsp.2021.103333>.
18. Javorskyj, I., Yuzefovych, R., Matsko, I., Kurapov, P. (2021) Hilbert transform of a periodically non-stationary random signal: Low-frequency modulation. *Digital Signal Process.*, **116**, 103113. DOI: <https://doi.org/10.1016/j.dsp.2021.103113>.

ORCID

I.M. Javorskyj: 0000-0003-0243-6652,
R.M. Yuzefovych: 0000-0001-5546-453X,
O.V. Lychak: 0000-0001-5559-1969

CONFLICT OF INTEREST

The Authors declare no conflict of interest

CORRESPONDING AUTHOR

R.M. Yuzefovych
Karpenko Physico-Mechanical Institute
of the NASU
5 Naukova Str., 79060, Lviv, Ukraine
E-mail: roman.yuzefovych@gmail.com

SUGGESTED CITATION

I.M. Javorskyj, R.M. Yuzefovych, O.V. Lychak,
P.O. Semenov (2022) Methods and means of
early vibration diagnostics of rotating components of
mechanisms of quay container handlers. *The Paton
Welding J.*, **1**, 48–58.

JOURNAL HOME PAGE

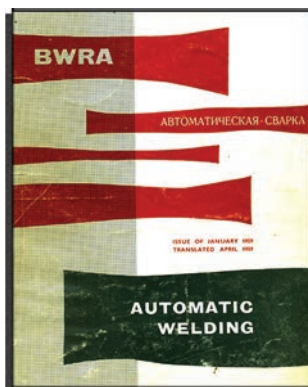
<https://pwj.com.ua/en>

Received: 07.12.2021

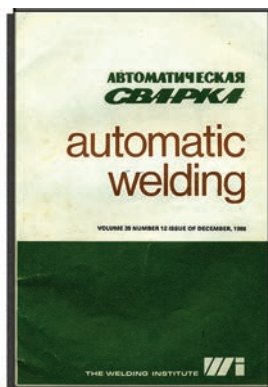
Accepted: 07.02.2022

“THE PATON WELDING JOURNAL” — SHORT HISTORY

The history of “The Paton Welding Journal” is closely connected with the E.O. Paton Electric Welding Institute (PWI) and the history of “Avtomatychne Zvaryuvannya” journal. It is assumed that the first issue of “Avtomatychne Zvaryuvannya” journal was published in March, 1948 [in Russian].



No. 1, 1959



No. 12, 1986

Beginning from 1959, translation of the journal entitled “Automatic Welding” (ISSN 0005-108X) into English was performed by the British Welding Research Association, Cambridge, UK. The first English issue for 1959 was a translation of the Russian issue No.4, 1959. At that time, the communication and translation took at least 15 weeks. Therefore, in order to ensure the accuracy and fast reproduction of the text, none of the metric units were converted into British units, except for some basic coefficients. In 1959–1986 the journal cover was changed three times.

The “Automatic Welding” journal publication was interrupted in 1987. Instead of it, PWI in cooperation with The British Library Document Supply Centre, released a monthly translation journal “Welding International” (ISSN 0950-7116). This journal published part of the papers from the Russian variant of “Avtomatychne Zvaryuvannya” journal.

Starting from 1989, PWI resumed publication of the translated journal. Thus, in 1989–1990 “The Paton Welding Journal” (ISSN 0957 798X) was published by Abington Publishing House, which is part of Woodhead Publishing Ltd (Cambridge, UK). During this period, the appearance of the journal cover changed three times.

In 1991–1998, “The Paton Welding Journal” (ISSN 0957 798X) was published monthly

by Riecanisky Science Publishing Co (Cambridge, UK), and its cover changed twice. From the middle of 1994, the journal starts publishing information about the availability of abstracts of the papers from “The Paton Welding Jour-



No. 2, 1991



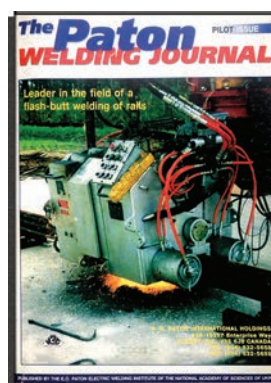
No. 9, 1998

nal” in electronic format at the site: <http://www.demon.co.uk/cambsci/pwj.html>.

In July, 1999, PWI, with the support of the International Association “Welding”, issued a pilot version of “The Paton Welding Journal”. “The Paton Welding Journal” (ISSN 0957 798X) is published with the frequency of 12 issues per year, and it is an English translation of “Avtomatychne Zvaryuvannya”. The journals in both languages are issued simultaneously without any time differences. The journal site is: <https://patonpublishinghouse.com/eng/journals/tpwj>. Beginning from issue No.7, the journal is indexed in the Crossref, with DOI indices assigned to each published scientific paper. From No.8, 2021 the content of the journal includes papers received from authors from around the world in the field of welding, metallurgy, materials science and selectively includes translations into English of papers from the following journals, which are published by PWI in Ukrainian: “Avtomatychne Zvaryuvannya” (Automatic Welding), “Tekhnichna Diahnostyka ta Neruivnyi Kontrol” (Technical Diagnostics & Nondestructive Testing), “Suchasna Elektrometalurhiya” (Electrometallurgy Today).



No. 1, 1989



July, 1999



No. 12, 2021

Over the years, “The Paton Welding Journal” has gone through a lot of transformations, but it is developing, it has not lost its relevance and has a stable international status and demand.

Svitlana Ivanenko, Head of the PWI Library

SUBSCRIPTION-2022



«The Paton Welding Journal» is Published Monthly Since 2000 in English, ISSN 0957-798X, doi.org/10.37434/tpwj.

«The Paton Welding Journal» can be also subscribed worldwide from catalogues subscription agency EBSCO.

If You are interested in making subscription directly via Editorial Board, fill, please, the coupon and send application by Fax or E-mail.

12 issues per year, back issues available.

\$384, subscriptions for the printed (hard copy) version, air postage and packaging included.

\$312, subscriptions for the electronic version (sending issues of Journal in pdf format or providing access to IP addresses).

Institutions with current subscriptions on printed version can purchase online access to the electronic versions of any back issues that they have not subscribed to. Issues of the Journal (more than two years old) are available at a substantially reduced price.

SUBSCRIPTION COUPON

Address for journal delivery _____

Term of subscription since _____

20

till _____

20 _____

Name, initials _____

Affiliation _____

Position _____

Tel., Fax, E-mail _____

The archives for 2009–2020 are free of charge on www://patonpublishinghouse.com/eng/journals/tpwj



ADVERTISING

in «The Paton Welding Journal»

External cover, fully-colored:

First page of cover
(200×200 mm) — \$700
Second page of cover
(200×290 mm) — \$550
Third page of cover
(200×290 mm) — \$500
Fourth page of cover
(200×290 mm) — \$600

Internal cover, fully-colored:

First/second/third/fourth page
(200×290 mm) — \$400

Internal insert:

(200×290 mm) — \$340
(400×290 mm) — \$500

• Article in the form of advertising is 50 % of the cost of advertising area

• When the sum of advertising contracts exceeds \$1001, a flexible system of discounts is envisaged

• Size of Journal after cutting is 200×290 mm

Address

11 Kazymyr Malevych Str. (former Bozhenko Str.), 03150, Kyiv, Ukraine

Tel.: (38044) 200 82 77

Fax: (38044) 200 82 77

E-mail: journal@paton.kiev.ua

www://patonpublishinghouse.com/eng/journals/tpwj